Graduate Theses and Dissertations

Graduate School

2011

Magneto-Dielectric Polymer Nanocomposite Engineered Substrate for RF and Microwave Antennas

Cesar A. Morales
University of South Florida, camorale@mail.usf.edu

Scholar Commons Citation

Magneto-Dielectric Polymer Nanocomposite Engineered Substrate for RF and

Microwave Antennas

by

Cesar A. Morales

A dissertation submitted in partial fulfillment
of the requirements for the degree of
Doctor of Philosophy
Department of Electrical Engineering
College of Engineering
University of South Florida

Major Professor: Jing Wang, Ph.D.
Thomas M. Weller, Ph.D.
Lawrence Dunleavy, Ph.D.
Ryan Toomey, Ph.D.
Hariharan Srikanth, Ph.D.

Date of Approval:
October 21, 2011

Dedication

To my Wife Paula Algarin, my Mother Cielo Silva, my Father Cesar Morales and

my brothers Julio, Oscar and Andres Morales

Acknowledgements

I like to express my gratitude to my lovely wife, Paula, whom stands by my side always, supporting me with infinite love and wise words and being my fuel for everything I have done in the past years.

I would also like to thank my parents Cesar and Cielo. They are my best counselors and have always been there giving me love and dedication that helped making me a better person since childhood. They have been my inspiration and strength that keeps me going on.

I am especially grateful for the moral support received from my brothers, Julio, Oscar and Andres. They are constantly in my mind and my heart providing me with the motivation to become a better person.

I want to state my appreciation to my professors Dr. Jing Wang, Dr. Tom Weller and Dr. Larry Dunleavy for their academic guidance and support in making me a better scholar and professional in my field.

Finally, special thanks are given to my close friends and colleagues Julio Dewdney, Daniel Sosa, I-Tsang Wu, Tianpeng Wu, Kosol Son, Sergio Melais, Julio Medrano, Norma Paz, Michael Konrad, Megan DiTizio, Julie McCoy and Kristen Stojak. They have always provided me a helping hand during the moments of need.

Table of Contents

List of Tables

List of Figures

Abstract

This dissertation presents the first reported systematic investigation on the implementation of multilayer patch antennas over Fe_3O_4–based polymer nanocomposite (PNC) magneto-dielectric substrates. The PNC substrate is created by the monodispersion of Fe_3O_4 nanoparticles, with mean size of 7.5nm, in a polymeric matrix of Polydimethylsiloxane (PDMS).

Recently, magneto-dielectric substrates have been proposed by several researchers as a means for decreasing the size and increasing the bandwidth of planar antennas. Nevertheless, factors such as high loss and diminished control over magnetic and dielectric properties have hindered the optimal performance of antennas. In addition, the incompatibility and elevated complexity prevents integration of conventional magnetic materials with antennas and standard fabrication processes at printed circuit boards (PCBs) and wafer levels. Additionally, the low hysteresis losses exhibited by uniformly embedded superparamagnetic nanoparticles complemented by the ease of integration of polymer nanocomposites in standard fabrication processes, offer promising solutions to resolve any of the complications and concerns foresaid.

Towards this dissertation work, one multilayer antenna was constructed over a molded PDMS substrate along with three similar antennas built on PDMS-Fe_3O_4 PNC substrates with different Fe_3O_4 nanoparticle loading concentrations in the PDMS matrix of 80%, 50% and 30% by weight. This pioneering work in the

experimental implementation and characterization of magneto-dielectric PNC antennas has not only resulted in antennas with different operational frequencies in the 3-5GHz band, but also expanded our knowledge base by correlating the concentration of magnetic nanoparticles to key antenna performance metrics such as antenna bandwidth, antenna efficiency and miniaturization factors.

Among the most significant results a magneto-dielectric antenna with maximum miniaturization factor of 57%, and a 58% increase in bandwidth, whilst retaining an acceptable antenna gain of 2.12dBi, was successfully demonstrated through the deployment of molded PDMS-Fe_3O_4 PNC substrate under external DC bias magnetic fields.

This dissertation also presents a versatile process for constructing flexible and multilayer antennas by the seamless incorporation of a variety of materials such as PDMS, Liquid Crystal Polymer (LCP) laminates, metal clads and molded magneto-dielectric polymer nanocomposites with evenly embedded magnetic nanoparticles.

Chapter 1

Introduction

1.1 Overview

The work presented in this dissertation introduces the implementation of bandwidth-enhanced patch antennas on molded magneto-dielectric polymer nanocomposite substrates, which are the first of their kind. A patch antenna design is selected because of its high susceptibility to the substrate characteristics. This antenna has a microstrip configuration, and therefore the field interaction between the patch and the ground plane largely occurs in the substrate underneath the patch. Taking advantage of this condition, the patch is placed over a cavity filled with magneto-dielectric nanocomposite material. In particular, polymer nanocomposites consisting of Magnetite (Fe_3O_4) nanoparticles, evenly dispersed in a Polydimethylsiloxane (PDMS) matrix, are prepared in order to fill the cavity. The unique magneto-dielectric properties of this engineered material facilitate the miniaturization of the antenna, while improving its performance by widening the antenna bandwidth as compared to those of conventional counterparts designed on pure dielectric substrates, and improving impedance matching to free-space (i.e., air around the antenna). The implementation of magneto-dielectric substrate opens the possibility of miniaturization using new materials while retaining low permittivity, which reduces energy trapping inside the substrate, and thus facilitating the radiation of

the antenna to free space. The decreased permittivity also helps mitigate losses caused by the excitation of surfaces waves into the substrate.

The complex permittivity and permeability of the magnetite polymer nanocomposites are both sensitive to external DC bias magnetic fields, thereby enabling optional tuning of the operational frequency and the modification of the antenna radiation characteristics (i.e. antenna efficiency)

1.2 Dissertation Organization

This dissertation is organized into six chapters, with the first and sixth corresponding to introduction and conclusions respectively. Chapters two through five describe the primary contributions of the work developed in this dissertation.

Chapter 2 presents the background and review of magneto-dielectric substrates for antenna implementation and development. There, the basics on the electrical properties of dielectric and magnetic materials are presented, providing a detailed description of complex permeability and permittivity. Thereafter, an overview on how the properties of the material define antenna size and performance is elaborated. Finally, electromagnetic simulations are used to demonstrate the advantages of using magneto-dielectric versus pure dielectric substrates.

Chapter 3 presents the fabrication and characterization of magnetite (Fe_3O_4) polymer nanocomposites. Initially, a brief explanation of the characteristics of magnetite nanoparticles is provided. Thereafter, synthesis and characterization of nanoparticles and polymer nanocomposites are described.

Chapter 4 presents the methodology for characterization and extraction of complex permeability and permittivity of polymer nanocomposites using microstrip transmission line test fixtures. This chapter explains in detail how well-known techniques, such as the Nicolson-Ross-Weir and Barker Jarvis methods were adapted for multilayer microstrip-based structures for the purpose of extracting the electrical properties of magneto-dielectric materials.

Chapter 5 presents the design and implementation of multilayer patch antennas equipped with dielectric and magneto-dielectric substrates. Experimental results are presented to reveal the substantial influence of the electrical properties of the material (i.e. permeability, permittivity, dielectric and magnetic loss tangents) on the overall performance of the magneto-dielectric antennas.

1.3 Contributions

The main contribution from this dissertation work is the implementation of magneto-dielectric polymer nanocomposites for the miniaturization and bandwidth enhancement of microstrip patch antennas, while upholding acceptable performance as well as functional radiation characteristics.

Deployment of newly developed polymer nanocomposites in RF/microwave antennas, calls for the extraction of the intrinsic electrical properties of these materials, which is deemed essential for the effective design and implementation of such devices. This process was developed by engineering a hybrid algorithm that combines time-domain techniques [23], frequency domain

techniques [22][26], with transmission line theory and conformal mapping methods [24][25][27]-[35].

A multilayer patch antenna design has been developed here to demonstrate the usefulness of magneto-dielectric nanocomposites, easiness in the processing and integration techniques onto PCB level design, and their soaring potentiality of integration to micro-fabrication levels.

Magneto-dielectric polymer nanocomposites have been systematically studied by implementing different concentrations of magnetite (Fe_3O_4) nanoparticles (80%, 50% and 30% by weight) in a polymeric matrix of Polydimethylsiloxane (PDMS) and the trade-offs between miniaturization, bandwidth enhancement, antenna performance and concentration of nanoparticles have been successfully identified.

1.4 Current State of the Art

The most common practice for antenna miniaturization has traditionally rested in using high permittivity substrates for the purpose of reducing the antenna size by a factor roughly proportional to $\sqrt{\varepsilon_r}$. However, size reduction is achieved at the expense of lowering the antenna gain and bandwidth, which is caused by the excessive coupling between the patch and ground plane. In addition, high permittivity materials tend to be heavy (e.g., ceramics) hence not viable for lightweight antenna structures [1].

1.4.1 High Losses in Regular Magnetic Substrates

As an alternative approach, several antennas incorporating magneto-dielectric substrates have been presented, which continue to cope with issues

related with high material losses [2]. This is particularly the case of an antenna configuration recently proposed by Erkmen *at al.,* in which ferrite layers with magnetic loss and dielectric loss tangents of around 0.2 (*tanδ_d* ≈ *tanδ_m* ≈ 0.2) are implemented [3]. The effect of material losses has been decreased by maintaining a given distance between the printed antenna and the magneto-dielectric layer, with some drawbacks related to a high profile (above 2 inches) [2]. Undoubtedly, some important enhancements in the antenna radiation field have been achieved using the ground plane as a reflector, even at frequencies when the distance between the antenna and the ground plane becomes less than λ/20 [2]. It is here that the trade-off between the overall antenna height, weight and performance becomes a matter of important interest.
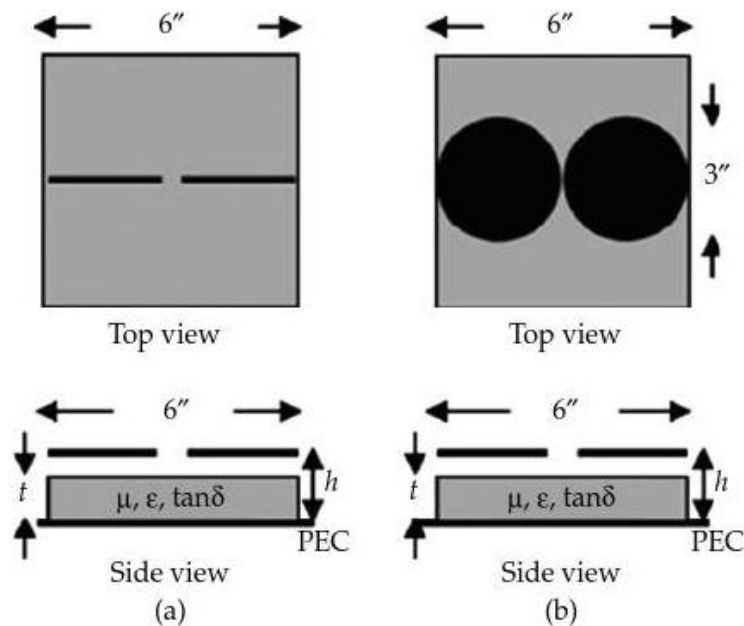
Figure 1.1 – (a) Six-inch wire dipole antenna over a finite matched impedance layer (MIL); (b) Six-inch circular dipole over a finite MIL on a PEC (Perfect Electric Conductor) surface. From Volakis *et al.* [2].

Two typical antenna configurations on a ferrite-coated ground plane are shown in Figure 1.1 These designs are based on the strategic selection of materials and configurations that lead to a suppressed destructive interference caused by the ground plane, and consequently resulting in larger antenna gain compared to a free standing antenna [2].
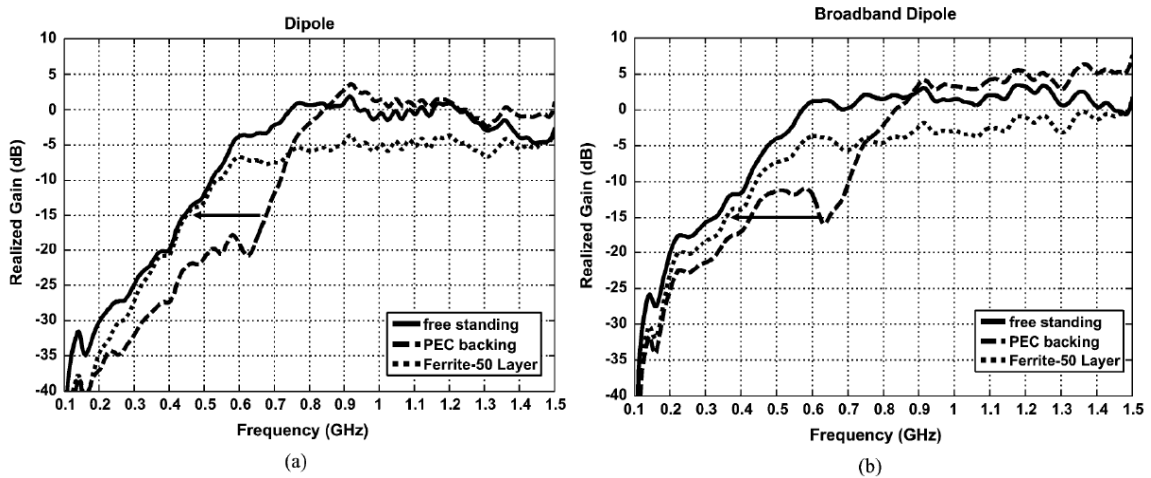
Figure 1.2 – Measured boresight gain for (a) the wire dipole shown in Figure 1.1 (a); and (b) the circular dipole shown in Figure 1.1 (b). From Erkmen *et al.* [3].

Figure 1.2 shows the measured gain with and without Matched Impedance Layer (MIL) treatment for dipole antennas illustrated in Figure 1.1. The -15 dB gain point is shifted from 680 MHz down to 440 MHz for the wire dipole and from 650 MHz down to 350 MHz for the circular dipole. These frequency shifts correspond to 35.3% and 46.15% miniaturization factors, respectively [2][3]. However, the effective gain above certain frequencies is lowered due to the varying ferrite properties and especially to the additional losses induced. Until now, most of the commercially available magneto-dielectric materials are not suitable for applications above 1.5GHz. These issues can be addressed using

more complex geometries and configurations, such as tapered lines or selective

variations in the thickness of the coated MIL layer [1].

1.4.2 Prior Work on Simulation and Modeling of Magneto-Dielectric Materials

Namin *et al.* [1] have proposed a methodology to design stacked-patch

antennas based on magneto-dielectric substrates. In particular, they created an

antenna in which the effective permeability and permittivity holds the same value,

which is also referred as the matched magneto-dielectric condition. Under this

circumstance, the impedance of the antenna is going to be equal to that of the

free space. This unique property allows for a better impedance matching over the

bandwidth of the antenna, thus decreasing any losses due to wave reflection

within the antenna and the free space. Additionally, even with moderated values

of permeability and permittivity of less than 5, considerable reductions in length,

width and thickness were achieved [1].
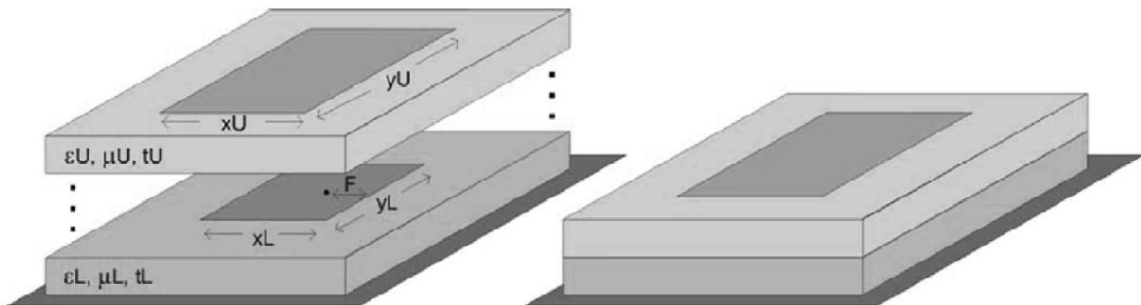
Figure 1.3 – Exploded and collapsed-view schematics of the stacked-patch antenna design using magneto-dielectric substrates. From Namin *et al.* [1].

As shown in Figure 1.3, the entire assembly consisted of a stack of patch

antennas, each one of them was placed on top of a different magneto-dielectric

substrate. The effective dielectric and magnetic parameters of the resulting stack

were calculated by combining the relative parameters of each layer and its

intervening volumetric fractions. The antenna was strategically designed using a genetic algorithm (GA), where its overall size and broadside gain were considered as the target parameters while keeping the matched magneto-dielectric condition [1]. To maintain this condition, unwarranted adjustments were adopted, such as the dynamic assignation of values for the effective parameters of each individual substrate layer.
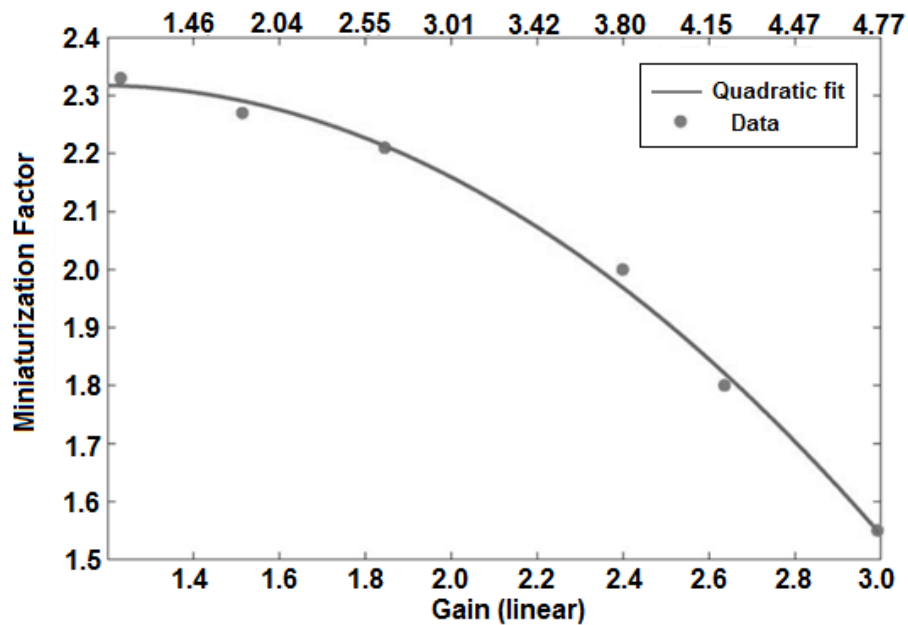
Figure 1.4 – Antenna miniaturization factor vs. the broadside gain at the center frequency obtained for several designs. From Namin *et al.* [1].

As stated before, the creation of magneto-dielectric materials provides viable means for miniaturization. However, there is a tradeoff between the highest gain achievable and its miniaturization factor. Figure 1.4 shows the miniaturization factor (with respect to a dielectric-only antenna) vs. broadside gain (with respect to an isotropic antenna) at the center frequency. This data was acquired using several optimal designs of the stacked patch antenna.

Miniaturization of antenna typically leads to some level of performance degradation that cannot be avoided, even with the use of magneto dielectric materials. The performance of the antenna is going to suffer due to the reduction of its physical area and the increment of confined energy given the proximity of the metallization layers. In addition, the results presented in [1] are based in simulations under ideal circumstances, with the loss properties of the magneto-dielectric materials and the metallization layers being neglected. Undoubtedly, the aforementioned loss related properties would introduce a negative impact on the overall performance of any antenna implemented in real applications.

Another proposed approach was to employ thin ferromagnetic layers based on metals such as iron and cobalt [4]. However, this type of laminate may be used only at frequencies below 2-3GHz, because the effective permeability drops rapidly while frequency is increased. These materials also exhibit higher magnetic losses at high frequencies [4].

1.4.3 Issues for the Current State of the Art

As explained previously, high permittivity materials are frequently used for antenna miniaturization at the expense of reduced gain and bandwidth, resulting from incremented capacitive coupling throughout the substrate.

Despite the fact that magneto-dielectric materials present a promising new approach for miniaturization of components, the currently available magneto-dielectric materials exhibit high losses that adversely affect the performance of current antenna designs. Moreover, commercially available materials are not well suited for device applications above 1.5GHz [2]. Permittivity and permeability

both tend to decrease as the operational frequency is increased. The presence of ferromagnetic resonances and high loss properties have curtailed wider acceptance of magneto-dielectric materials usage for implementing antennas at higher frequencies.

Commercially available magnetic materials are generally non-versatile. High permeability materials are often hard and heavy (e.g. Iron, cobalt and other ferrites) and therefore unsuitable for the fabrication of lightweight antennas. Moreover, it is difficult to integrate these materials through conventional fabrication processes especially when physical flexibility is greatly preferred. This dissertation work represents one of the first attempts to fill this knowledge and technology gap.

Chapter 2

Background and Literature Review

2.1 Introduction

Materials used for RF and microwave antennas are selected based on their effective electrical properties. In recent years, electromagnetic properties such as complex permeability and permittivity offered by engineered metamaterials have shown great promise in the miniaturization of antennas. Nevertheless, the size reductions yielded by these metamaterials that consist of periodic structures, are still burdened by the undesired performance issue of narrow bandwidth. Nowadays, researchers have been interested in carefully exploring intrinsic details of the materials, with the specific goal of tailoring their dielectric and magnetic properties, and thus granting improvements in the performance of RF/microwave devices (e.g. antennas). Particularly, magneto-dielectric materials have been widely examined for antenna applications, exhibiting excellent advantages amid several unresolved deficiencies. Aside from the fact that permittivity and permeability diminish as the operational frequency increases, high dielectric and magnetic losses and incompatibility with standard fabrication processes are some of the other challenges that still require resolution. These setbacks are addressed in following chapters, in which magneto-dielectric nanocomposites are proposed as a favorable alternative to miniaturizing and improving the performance of microstrip antennas.

Also presented in this chapter is a review on the fundamental antenna design concepts related to the implementation of magneto-dielectric materials as the engineered substrate. A comprehensive overview of the electrical properties of such materials is shown to explain how the presence of complementary magnetic and dielectric properties is advantageous to enhancing the general performance of planar antennas. In the chosen rectangular microstrip patch antenna topology, the field distribution is confined inside the substrate, between the patch and the ground plane. Consequently, the electrical properties of the substrate determine the overall performance of such a device, thereby setting the performance metrics to include the bandwidth, size and efficiency of the antenna. Finally, patch antennas are designed and simulated using a variety of engineered substrates (from pure dielectric to magneto-dielectric materials). Comparisons of the different designs provide a good understanding of how the performance of the antenna is characteristically defined by the electrical properties of the substrate.

2.2 Antenna Miniaturization by Using Magneto-Dielectrics

Miniaturization, bandwidth enhancement and impedance matching to its surrounding media have become the major concerns for antenna designers. One of the biggest issues for the employment of materials with high permittivity is that the improvement in miniaturization factor results in reduced bandwidth and inferior impedance matching. The key challenges and tradeoffs between the aforementioned performance metrics as well as their dependency on the

electrical properties of the substrate are relatively understood by classical antenna design theory and concepts.

The size of any existing antenna is inherent to its guided wavelength in the antenna substrate material:

$$Antenna\ Size \propto \lambda_g = \frac{c}{f \cdot \sqrt{\mu_{eff} \cdot \varepsilon_{eff}}}$$

(2.1)

where λ_g is the guided wavelength, c is the speed of light, ε_{eff} and μ_{eff} are the effective permittivity and effective permeability, respectively. Both ε_{eff} and μ_{eff}, are proportional to the relative permittivity (ε_r) and relative permeability (μ_r) of the substrate material and dependent on the geometry of the antenna design.

From equation (2.1), it is clear that miniaturization of antennas can be achieved by the implementation of high permittivity (ε_r) substrates and superstrates. However, antenna miniaturization through this route occurs at the expense of degradation of its performance. High permittivity causes confinement of the antenna electric fields within the substrate situated between the metallization layers, thereby lowering the bandwidth and efficiency of the antenna. Alternatively, the usage of dielectric materials with elevated permeability ($\mu_r > 1$) provides miniaturization while improving the bandwidth and efficiency of the antenna. These effects are detailed in the subsequent section.

2.3 Importance of Substrate in Wave Impedance Matching

The characteristic impedance of the any substrate is defined by the relation between the relative values of permeability and permittivity as follows:

$$\eta = \sqrt{\mu_0/\varepsilon_0} \cdot \sqrt{\mu_r/\varepsilon_r} = \eta_0 \cdot \sqrt{\mu_r/\varepsilon_r} \qquad (2.2)$$

where η_0 is the characteristic impedance of the free space.
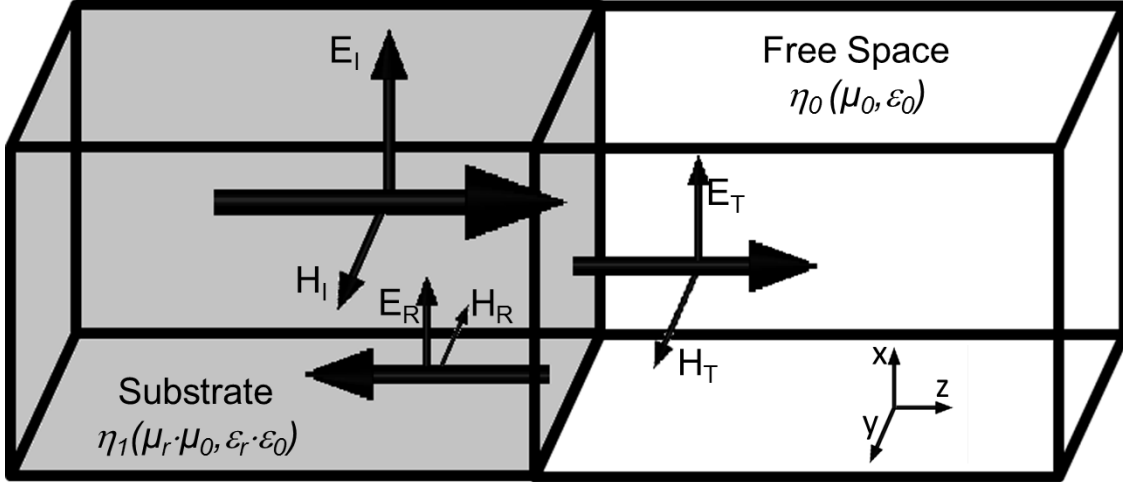
Figure 2.1 – Wave reflection and transmission across the substrate and free space interface.

Figure 2.1 shows the phenomena of normal transmitted and reflected waves at the interface between two different materials (a substrate and the free space). For understanding the basic concept, the simplest case with normal incidence is explained here. When an incident wave (E_I, H_I) encounters the interface between the different materials, a fraction of the incident wave is transmitted to the second medium (E_T, H_T) and another fraction is reflected (E_R, H_R). Magnitude and phase of the reflected and transmitted waves are determined by the electrical properties of the different materials, under the assumption that at the boundaries the waves do not incur in any loss [5]:

$$E_I = \hat{a}_x \cdot E_0 \cdot e^{-j\beta_1 z} \qquad (2.3)$$

$$E_R = \hat{a}_x \cdot \Gamma^b \cdot E_0 \cdot e^{+j\beta_1 z} \qquad (2.3a)$$

$$E_T = \hat{a}_x \cdot T^b \cdot E_0 \cdot e^{-j\beta_2 z} \qquad (2.3b)$$

14

$$H_I = \hat{a}_y \cdot \frac{E_0}{\eta_1} \cdot e^{-j\beta_1 z} \tag{2.3c}$$

$$H_R = -\hat{a}_y \cdot \frac{\Gamma^b \cdot E_0}{\eta_1} \cdot e^{+j\beta_1 z} \tag{2.3d}$$

$$H_T = \hat{a}_y \cdot \frac{T^b \cdot E_0}{\eta_0} \cdot e^{-j\beta_2 z} \tag{2.3e}$$

where E_0 is the amplitude of the incident electric field, η_1 is the characteristic impedance of the substrate, η_0 is the characteristic impedance of the free space, β_1 is the phase constant of the substrate, β_2 is the phase constant of the free space, Γ^b and T^b represent the reflection and transmission coefficient at the interface, respectively.

Γ^b and T^b can be calculated directly from the characteristic impedances of the two different materials[5]:

$$\Gamma^b = \frac{\eta_0 - \eta_1}{\eta_0 + \eta_1} \tag{2.4}$$

$$T^b = \frac{2\eta_0}{\eta_0 + \eta_1} \tag{2.5}$$

As observed in Equation (2.2), the characteristic impedance of high permittivity substrate is significantly low, posing a challenge against matching of the antenna substrate with the surrounding environment. From Equations (2.4) and (2.5) the optimum impedance matching is obtained when $\eta_0 = \eta_1$, which implies zero reflection ($\Gamma^b = 0$). From equation (2.2), this condition is readily achievable when the substrate is made of a magneto-dielectric material with equivalent relative permittivity and permeability $\varepsilon_r = \mu_r$.

2.4 Enhancement of the Antenna Bandwidth by Using Magneto-Dielectrics

The antenna bandwidth is also affected by the electrical properties of the substrate. Hansen and Burke derived a good approximation for the calculation of the bandwidth, based on a combination of the cavity and transmission line models for rectangular patch antennas, in which the resultant bandwidth is mainly controlled by the radiation resistance by assuming a substrate material with low loss properties [6]. For values of $\varepsilon_r \cdot \mu_r > 1$, a good approximation for the radiation conductance is given by [6]:

$$G = \frac{1}{40 \cdot \sqrt{\mu_r \cdot \varepsilon_r} + 170 \cdot \mu_r \cdot \varepsilon_r} \tag{2.6}$$

The characteristic admittance of a wide microstrip line is given by [7]:

$$Y_0 = \frac{a \cdot \sqrt{\varepsilon_r}}{\eta_0 \cdot t \cdot \sqrt{\mu_r}} \tag{2.7}$$

where a is the line width (patch width) and t is the substrate thickness. Based on the zero-order theory, the following expression is inherent to a resonant patch:

$$\frac{a}{\lambda_g} = \frac{1}{2 \cdot \sqrt{\mu_r \varepsilon_r}} \tag{2.8}$$

Furthermore, from equations (2.7) and (2.8), the characteristic admittance of the patch can be expressed as:

$$Y_0 = \frac{\lambda_g}{2 \eta_0 \cdot \mu_r \cdot t} \tag{2.9}$$

The quality factor Q can be then expressed in terms of the radiation conductance and the characteristic admittance [7]:

$$Q = \frac{\pi \cdot Y_0}{4 \cdot G} \tag{2.10}$$

The zero-order bandwidth BW can be defined at a VSWR≤2 as [6]:

$$BW = \frac{1}{\sqrt{2} \cdot Q} \tag{2.11}$$

Finally, combining Equations (2.6), (2.9), (2.10) and (2.11) [6]:

$$BW = \frac{96 \cdot \sqrt{\frac{\mu_r}{\varepsilon_r}} \frac{t}{\lambda_0}}{\sqrt{2} \cdot [4 + 17 \cdot \sqrt{\mu_r \varepsilon_r}]} \tag{2.12}$$

where λ_0 is the free space wavelength.

Assuming a patch antenna with substrate thickness t=1.57mm and zero-order resonance at 4GHz (λ_0=74.95mm), equation (2.12) can be evaluated by assigning different values to μ_r and ε_r. BW is evaluated for $1<\mu_r<5$ while keeping a constant $\varepsilon_r \cdot \mu_r$. In this case, theoretically, resonance frequency will remain constant if the antenna dimensions are also kept constant. With a constant $\varepsilon_r \cdot \mu_r$=6.76, BW and Γ^b are calculated and plotted in Figure 2.2.
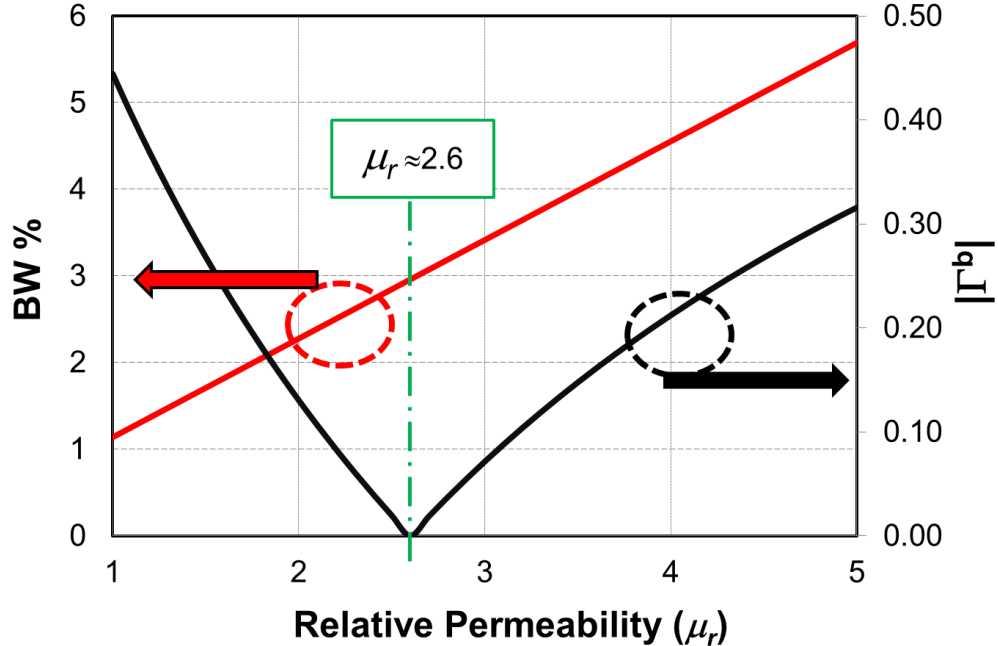
Figure 2.2 – Theoretical BW and $|\Gamma^b|$ vs. μ_r while a patch antenna retains the same dimensions.

As noted in Figure 2.2., the best plane wave impedance matching occurs at $\varepsilon_r=\mu_r=2.6$, when $\Gamma^b=0$. Note that this reflection coefficient does not refer to the one experimented by the patch, but that experimented by a plane wave traveling within the substrate-air interface and may be considered suitable for explanation purposes. Also, as μ_r increases, a linear increment in *BW* is observed. This can be easily anticipated through Equation (2.12) which reveals the linear dependence of *BW* on μ_r, when the product of μ_r and ε_r remains constant. This also can be observed from Equations (2.9) to (2.11), where given an increasing μ_r, the antenna quality factor is decreased with the characteristic admittance of the patch. Note that in this set of equations, both the guided wavelength λ_g and the radiation conductance G are kept constant (i.e., given a constant $\varepsilon_r \cdot \mu_r$).

2.5 Simulations of Multilayer Patch Antennas on Dielectric and Magneto-Dielectric Substrates

A brief study of the potential benefits of magneto-dielectric polymer nanocomposites is proposed in this section. For this purpose, three microstrip patch antennas have been designed and simulated using the 3D full-wave electromagnetic field simulation software ANSYS HFSS v.11.1. Two designs employ dielectric-only substrates and the third one is implemented based on a magneto-dielectric substrate. For all cases, the operation frequency was set to 4GHz.

For the first and second antennas, two laminates have been selected for the design. The first laminate is Rogers RT/Duroid 5870 ($\varepsilon_r=2.33$, $tan\delta_d=0.0012$)

with a thickness of 62mils (1.575 mm). A dielectric-only material fills a cavity buried through the entire substrate. This cavity has the same lateral dimensions identical to the antenna patch. A flexible liquid crystal polymer laminate Rogers Ultralam 3850 (ε_r=2.9, $tan\delta_d$=0.0025) with a thickness of 1mil (0.025mm) is used to form the top metallization layer, composed of the microstrip-feed line and the patch. The thickness of the substrate has been selected following the work reported in [2], in which the maximum radiation efficiency of about 90% is achieved for a substrate with thickness closed to $0.02\lambda_0$. Figure 2.3 shows the 3D perspective-view schematic and the top view layout for the proposed multilayer patch antenna.
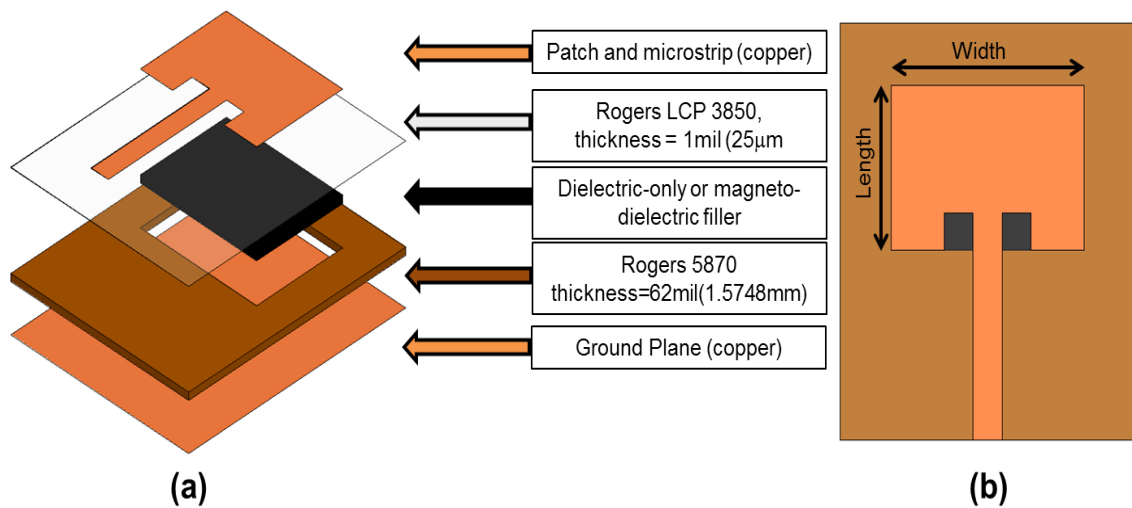
Figure 2.3 – (a) 3D perspective-view schematic of the multi-layer microstrip patch antenna; (b) Top view layout of the antenna.

The third design used a magneto-dielectric material as the cavity filler. The values for the relative parameters of the cavity fillers for the different microstrip patch antennas are summarized in table 2.1.

Table 2.1 – Relative parameters of the cavity fillers for the microstrip patch antennas

Design	Filler's Description	Relative Permittivity ε_r	Relative Permeability μ_r	Dielectric Loss Tangent $tan\delta_d$	Magnetic Loss Tangent $tan\delta_m$
1	Dielectric-only	2.6	1	0.001	0
2	Dielectric-only	6.76	1	0.001	0
3	Magneto-dielectric	2.6	2.6	0.001	0.001

The values of permeability and permittivity were selected to demonstrate that by using moderate values of these properties, the antenna size can be reduced while the bandwidth is improved. In addition, these values were also chosen to facilitate direct comparison between the antennas in order to explore how the substrate filler properties can help in the determination of their characteristics (size~ $\sqrt{\mu_r \cdot \varepsilon_r}$ and bandwidth~ $\sqrt{\mu_r/\varepsilon_r}$). Comparison between designs 1 and 3 illustrates that through the use of magneto-dielectric materials, it is possible to miniaturize the antenna patch, given the presence of permeability in the filler material. Besides, the comparison between designs 2 and 3 was carried out to show the bandwidth enhancement achieved through implementation of magneto-dielectric materials, as compared to a dielectric-only substrate. In this last case, the antennas have the same size because they maintained the same miniaturization factor (i.e., $\sqrt{\mu_r/\varepsilon_r}$).
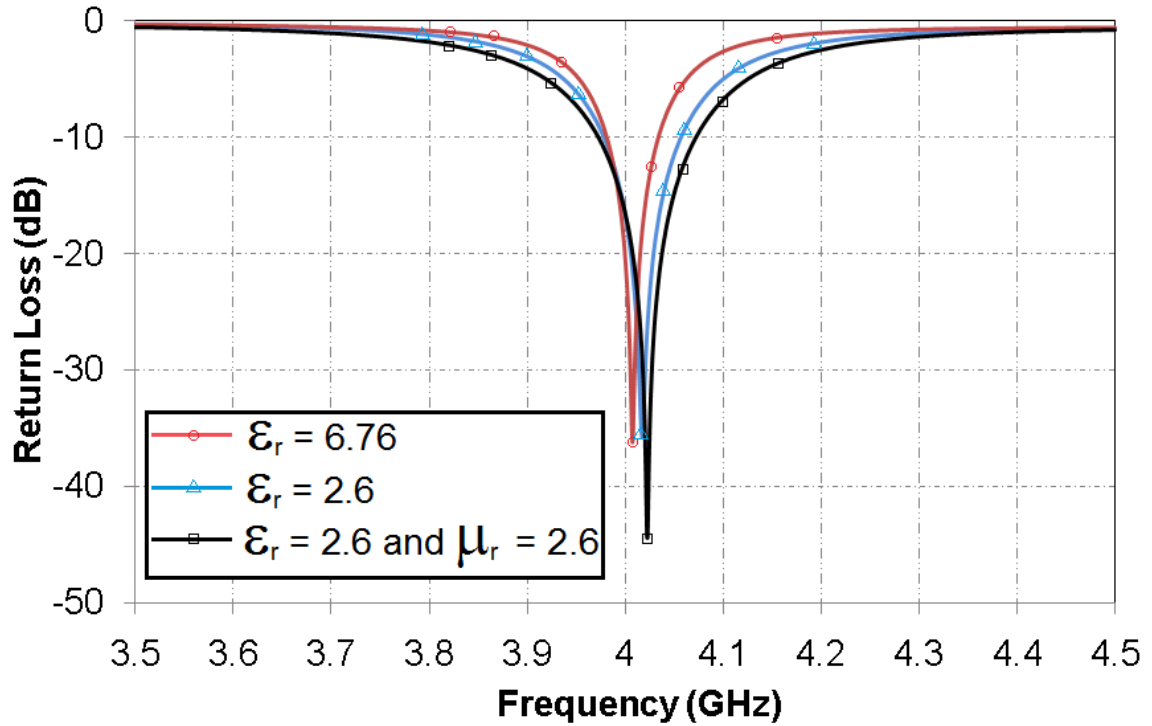
Figure 2.4 – Simulated return loss (dB) vs. frequency for the microstrip patch antennas, using dielectric-only and magneto-dielectric substrate fillers.

Figure 2.4 presents the return loss versus frequency for each one of the three designs. A marked difference in the antenna bandwidth (i.e., return loss < −10dB) is observed here. The antenna with ε_r =6.76 exhibited the narrowest bandwidth and the antenna with ε_r =2.6 and μ_r =2.6 presented the widest bandwidth. Figure 2.5 shows the broadside gain versus frequency for each one of the antennas. Consistently with the observations in the return loss, the magneto-dielectric antenna (i.e., design 3) presented a much wider gain response along with slightly higher gain level across the entire bandwidth as compared to dielectric antenna with high ε_r substrate (i.e., design 2). Nonetheless, as a consequence of a larger physical area, the highest gain is achieved in the dielectric antenna with ε_r =2.6 (i.e., design 1).
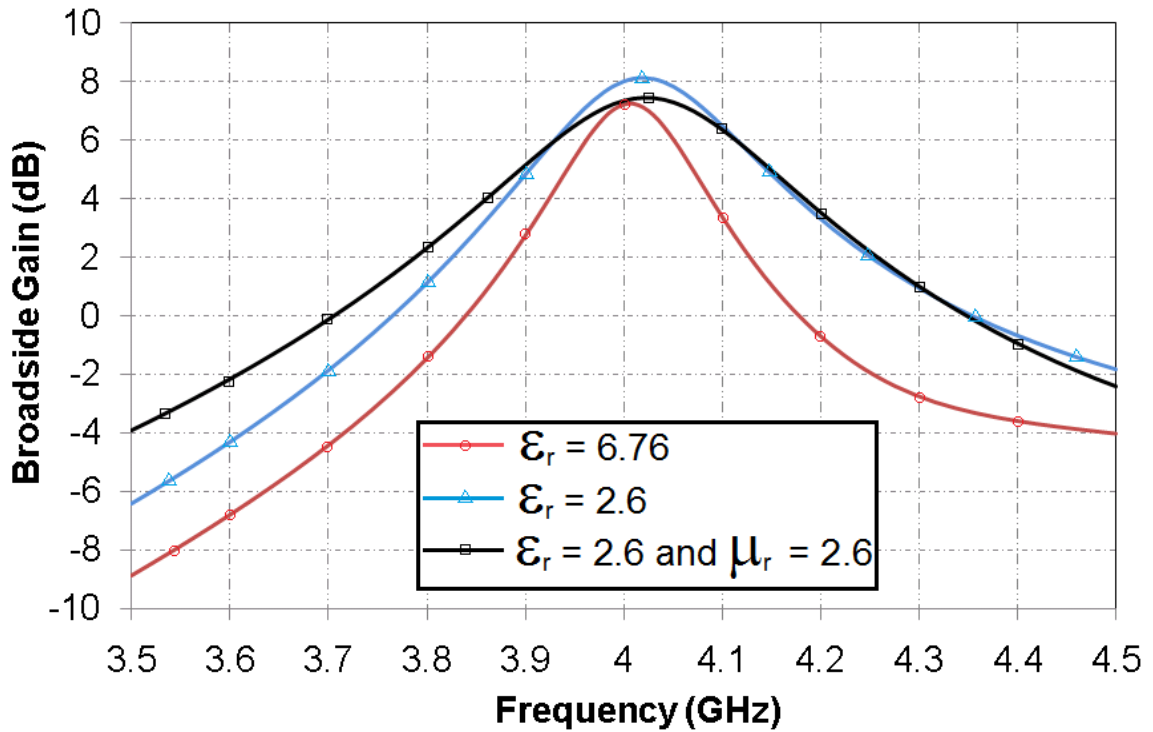
Figure 2.5 – Simulated broadside gain (dB) vs. frequency for the microstrip patch antennas, using dielectric-only and magneto-dielectric substrate fillers.

Table 2.2 presents a comparison between the performances of the microstrip patch antennas with different substrate fillers. It can be seen that designs 2 and 3 showed the same miniaturization factor of 1.98 (roughly 50%) as compared to design 1. However, design 3 presents the widest bandwidth of 100MHz (2.5%@4GHz), which is 1.9 times wider than the bandwidth of design 2. Undoubtedly, the magneto-dielectric material properties play an important role in the antenna miniaturization, without compromising the bandwidth of the miniaturized antenna.

Table 2.2 – Miniaturization, bandwidth and gain for the microstrip patch antennas using different fillers.

Design	Filler's Description	Patch Dimensions (width, length)mm (Area)mm^2	Bandwidth (%) @4GHz	Broadside Gain	Miniaturization Factor / Bandwidth Enhancement
1	Dielectric-only	(22.2, 27.6) (612.72)	79 MHz (1.98%)	8.13dBi	1 (0%) / 0%
2	Dielectric-only	(15.2, 20.4) (310.08)	52.5 MHz (1.31%)	7.24dBi	1.9 (49.4%) / -33.54%
3	Magneto-dielectric	(15.2, 20.4) (310.08)	100 MHz (2.5%)	7.45dBi	1.9 (49.4%) / 26.58%

For all the aforementioned reasons, many researchers have been focused in the development of magneto-dielectric materials ($\varepsilon_r \approx \mu_r > 1$) to improve the performance of RF/MW antennas.

Chapter 3

Fabrication and Characterization of Magnetite (Fe_3O_4) Polymer Nanocomposite

3.1 Introduction

This chapter presents some background on the fabrication and characterization of the materials used for engineering the magneto-dielectric substrate. Fabrication of polymer nanocomposites using polymeric matrices is herein explained in detail. In the last section, the physical dielectric and magnetic properties of the materials were extracted to analyze their impact on RF and microwave applications.

The nanoparticles implemented in this dissertation work are made of magnetite (Fe_3O_4). This material is a common magnetic iron oxide that has a cubic inverse spinel structure with oxygen forming a face centered cubic (FCC) closed packing, in which iron (Fe) cations occupy interstitial tetrahedral sites and octahedral sites [8][9]. The electrons can hop between Fe^{2+} and Fe^{3+} ions in the octahedral sites at room temperature, rendering magnetite as an important class of half-metallic material [8]. In the past, magnetite nanoparticles have been used as ferrofluids (e.g. rotary shaft sealing, oscillation damping, and position sensing) [8].

Biomedical and biological applications have also been targeted by using surface treated nanoparticles. Using the proper chemical treatment and surfactants, magnetic nanoparticles had been dispersed into water and other

biocompatible solvents [8][10]. Such a suspension is very useful in application where external magnetic fields are applied for positioning in specific areas, facilitating image diagnosis (i.e., magnetic resonance imaging) and assisted cancer therapy (i.e., killing cancer cells selectively by the heat generated due to hysteresis) [8][11].

Substrates and materials used for RF and microwave antenna implementation are required to have low dielectric and magnetic losses. For this reason, magneto-dielectric polymer nanocomposites must retain the superparamagnetic properties presented in the nanoparticles, avoiding clustering formation and achieving an excellent dispersion and interaction with the polymeric matrix. Additionally, nanoparticles with a narrow size distribution are required to obtain homogeneous interaction between them, for which the particles must be uniform in their physical and chemical properties [8]. Nonetheless, it is very difficult to produce non-agglomerated magnetite nanoparticles with a desired size and a narrow size distribution. By means of the synthesis process that is described in the following section, it is possible to obtain polymer nanocomposites with excellent monodispersion of magnetite nanoparticles.

3.2 Setup for Synthesis of Magnetite (Fe_3O_4) Nanoparticles

The nanoparticle synthesis follows a chemical procedure that requires a special setup that guarantees a controlled and stable environment, necessary to obtain particles with the right chemical composition and a tight size distribution. The reaction takes place in a 500ml three neck flask where all the chemicals are

combined. This vessel was laid on a heating mantle/magnetic stirrer setup. The center neck of the flask is connected to an allihn condenser, while the necks to the right and the left are connected to a thermocouple and a needle with controlled argon flow, respectively. The allihn condenser helps in the reflux of the solution that is heated above its boiling point. The thermocouple provides the feedback to a temperature controller which provides the power to the heating mantle.

3.3 Synthesis of Magnetite (Fe_3O_4) Nanoparticles

In this dissertation work, Fe_3O_4 nanoparticles are synthesized via thermal decomposition reaction. Several chemicals are used for the synthesis of magnetite nanoparticles, including Iron(III) acetylacetonate ($\geq$99.9 trace metal basis, also known as $Fe(acac)_3$), oleylamine (technical grade,70%), ethanol (200 proof, anhydrous, $\geq$99.5%), hexane (anhydrous, 95%), benzyl ether (98%) and oleic acid. All these chemicals were not modified to any extent and used as received.

Following a standard chemical procedure, Magnetite (Fe_3O_4) nanoparticles with an average size of 7 nm and coated with surfactants (oleylamine and oleic acid) are synthesized similar to what has been reported in [8][10]-[18]. Ten (10) mmol iron(III) acetylacetonate, 50 mL of oleylamine and 50 mL of benzyl ether are combined in a 500ml three-neck bottom rounded flask. The mixture is magnetically stirred under a continuous flow of argon at room temperature for 5 minutes. For dehydration purposes, the mixture is heated at 110°C for 1h, using a heating rate of 20°C/min. Subsequently, the sample is

quickly heated to reflux at 300°C for 2h, using the same 20°C/min heating rate. During the complete process, the sample is magnetically stirred to ensure homogeneity during the mixing process. Also, a continuous flow of argon gas is kept to maintain an inert environment. The resultant black colored solution is cooled to room temperature followed by addition of 200ml of ethanol into the solution. The precipitate is collected by centrifugation at 5000 rpm for 5 minutes of duration and washed with ethanol several times.
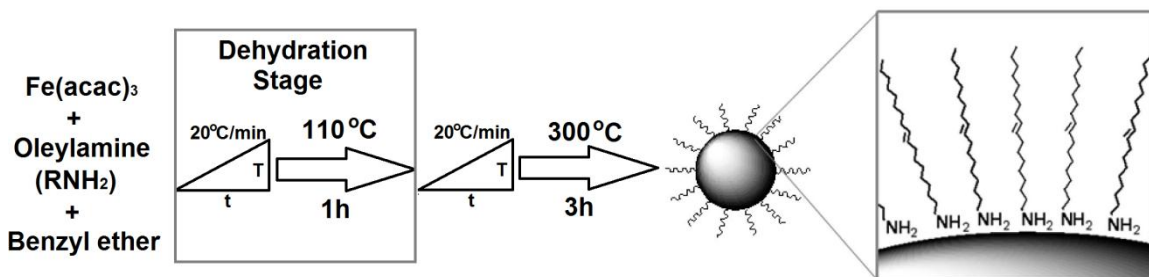
Figure 3.1 – Simplified diagram that illustrates the formation of Fe_3O_4 nanoparticles. Iron (III) acetylacetonate reacts with oleylamine in benzyl ether that acts as solvent. Adapted from Frey *et al.* [12].

Figure 3.1 presents a simplified scheme that illustrates the organic phase synthesis of Fe_3O_4 nanoparticles, through thermal decomposition of the organometallic complex precursor $Fe(acac)_3$ in benzyl ether followed by a reaction with oleylamine. The presence of a considerable amount of oleylamine is the key to provide a strong reductive environment for the thermal decomposition of $Fe(acac)_3$. Oleylamine acts as an excellent reducing agent, which is cheaper and stronger than 1,2-hexadecanediol, a reducing agent that has been previously used as a reducing agent in the synthesis of Fe_3O_4 nanoparticles[12].

Fe(acac)$_3$ is a metal carbonyl with strong tendency to dissociate the carbonyl groups when heated, leaving the zero-valent metal centers to nucleate and grow into nanoparticles[11]. However, the resultant nanoparticles are extremely reactive and subject to fast oxidation. Oleylamine acts as an efficient surface coating that prevents oxygen to penetrate and react with the nanoparticle. The coating is created by the interaction of the NH$_2$ group, existing in the oleylamine chemical structure, with the surface of the nanoparticles. The surface coating process with a non-polar surfactant such as oleylamine, results in nanoparticles with hydrophobic characteristics.

Given the non-polarity of oleylamine, and its implementation as nanoparticle surface coating, a stable nanoparticles suspension requires a nonpolar or weakly polar hydrocarbon solvent, such as toluene or hexane. The synthesized Fe$_3$O$_4$ nanoparticles were then suspended in a mixture of hexane (anhydrous, 95%) with 0.05 ml of oleylamine and 0.05ml of oleic acid. The presence of these two surfactants helps stabilize the particles in hexane for a longer period of time. Finally, the product is dried at room temperature when needed. By using this synthesis technique and the amounts of chemicals specified above, a successful experiment produces 0.65±0.2g of Fe$_3$O$_4$ nanoparticles.

3.4 Characterization of Magnetite (Fe$_3$O$_4$) Nanoparticles

3.4.1 Characterization of Nanoparticles Using X-Ray Diffraction

X-Ray Diffraction (XRD) measurements are made to analyze the crystallographic structure of magnetite (Fe$_3$O$_4$) nanoparticles. The sample is

prepared on a 2 inch silicon wafer with a well-recognized response when XRD is performed. As the particles are suspended in hexane and a layer coating with significant thickness is required for the XRD analysis, silicone adhesive resin is used to cast a rectangular shape receptacle that facilitates the deposition of the magnetite nanoparticle solution. Using a Pasteur pipette, several drops are deposited inside the receptacle and the hexane is evaporated at room temperature. After several repetitions, a layer with the desired thickness for the XRD measurements is obtained.

The XRD response of magnetite has been reported by Hanawalt *et al*. [19] as shown in the Table 3.1.

Table 3.1 – Summary of all the peaks in the XRD response for magnetite (Fe_3O_4) as reported by Hanawalt *et al.* [19].

Peak No.	h	k	l	D [Å]	2Theta [deg]
1	1	1	1	4.85	18.277
2	2	2	0	2.97	30.064
3	3	1	1	2.53	35.452
4	2	2	2	2.42	37.121
5	4	0	0	2.10	43.038
6	4	2	2	1.71	53.547
7	5	1	1	1.61	57.168
8	4	4	0	1.48	62.728
9	6	2	0	1.33	70.785
10	5	3	3	1.28	73.997
11	4	4	4	1.21	79.079
13	7	3	1	1.09	89.934

As seen in Figure 3.2, the measured XRD response confirms 12 out of the 13 peaks enlisted in Table 3.1 and previously reported in [19]. This pattern was measured with 2θ ranging from 10° to 100°, and all the peaks found herein

corresponded to the expected cubic inverse spinel structure with oxygen forming a face centered cubic (FCC) closed packing, in which Fe cations occupy interstitial tetrahedral sites and octahedral sites. [311] and [200] peaks are combined due to the close proximity between them. Aside from the XRD measurements, the existence of some of the primary crystal orientations is further confirmed in the following section, when a High Resolution Transmission Electron Microscopy (HR-TEM) of magnetite from the same batch is presented.
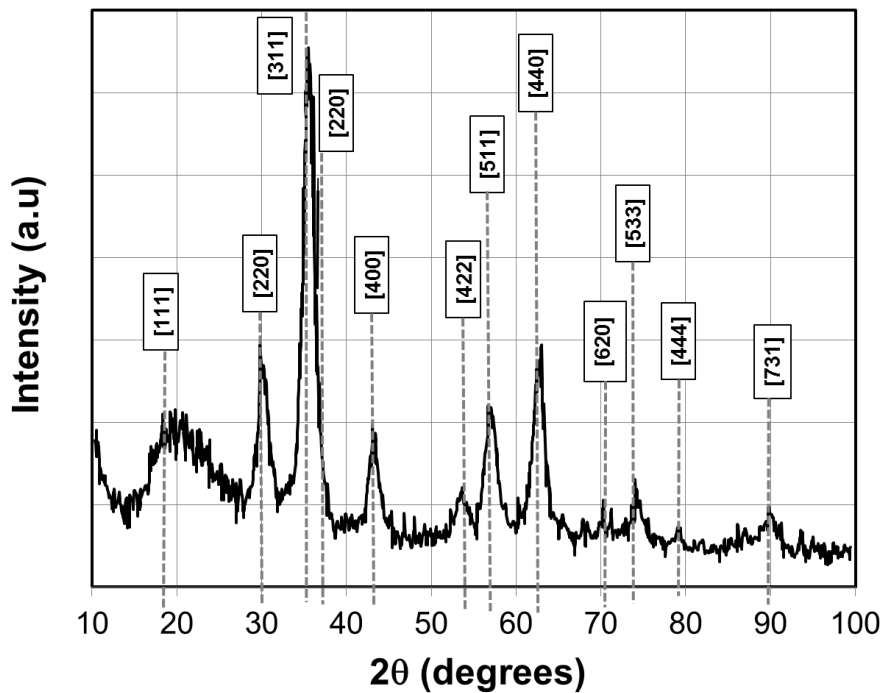
Figure 3.2 – X-Ray diffraction pattern of as-synthesized magnetite (Fe_3O_4) nanoparticles.

3.4.2 Characterization of Fe_3O_4 Nanoparticles Using TEM

Transmission Electron Microscopy (TEM) was used to study the dispersion and morphology of the Fe_3O_4 nanoparticles. Two different TEM tools (Tecnai F20 and Morgagni 268D, both from FEI Company) have been used to obtain the images. 0.6g of Fe_3O_4 nanoparticles were suspended in 30ml of

Hexane in a 40ml vial. The solution was agitated by a vortex mixer at 2200rpm for five minutes and ultrasonicated for another five minutes. Subsequently, a low concentration sample was prepared by applying a few drops of the Fe_3O_4 Hexane solution into a vial filled with 2ml of hexane, until the sample becomes brown/amber translucent, followed by two minutes of further vortex agitation at 2200 rpm and two more minutes of ultrasonication. The TEM samples are prepared on copper formvar coated grids (FCF400-Cu) from Electron Microscope Sciences. One drop of Fe_3O_4/hexane solution was applied on the TEM grid, followed by evaporation of the solvent at 60°C for five minutes.
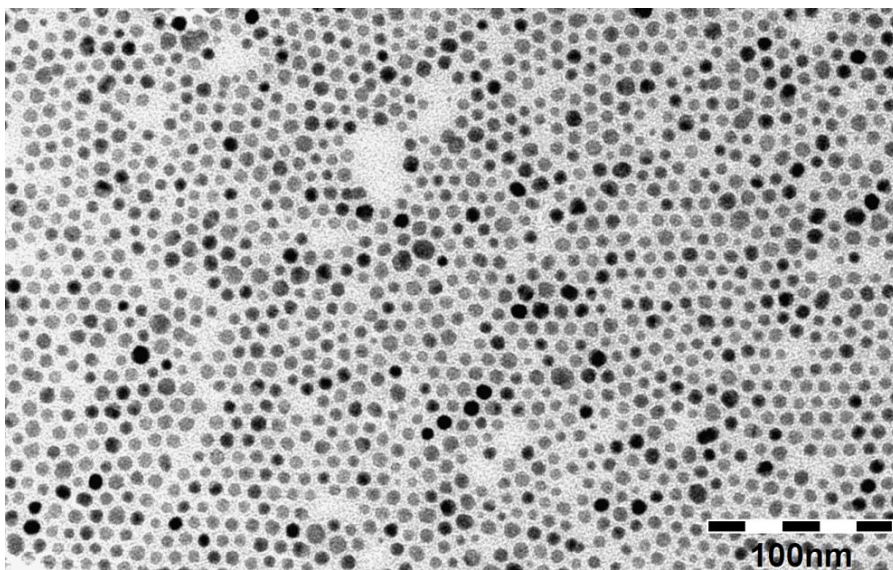
Figure 3.3 – Transmission Electron Microscopy (TEM) of Fe_3O_4 nanoparticles with mean size 7.5±3 nm. An excellent monodispersion (non-agglomeration) is observed.

Figure 3.3 presents a typical TEM image of the chemically synthesized, surfactant coated Fe_3O_4 nanoparticles with mean size of 7.5±2nm. As mentioned by Z. Xu *et al.*, particle size can be tuned from 7 to 10nm by varying the volume ratio of benzyl ether and oleylamine, the higher the ratio of oleylamine to benzyl

ether, the smaller the resultant Fe_3O_4 nanoparticles [12]. In their experiment, 7nm Fe_3O_4 nanoparticles were obtained using oleylamine only and ~10nm nanoparticles were obtained using a 1:1 volume ratio of oleylamine to benzyl ether. As shown in Figure 3.3 and Figure 3.4, for the process developed for this dissertation work, the size of the synthesized nanoparticles is 7.5nm±2nm, which implies that even smaller nanoparticles (below the minimum size reported in [12]) can be obtained by increasing the ratio of oleylamine to benzyl ether.

As seen in Figure 3.3 and Figure 3.4, Fe_3O_4 nanoparticles do not form clusters, as a consequence of the surface modification performed during the synthesis and suspension process. Nanoparticles are surface functionalized, coated by oleylamine and oleic acid, which prevents their agglomeration. Oleylamine and oleic acid also act as a buffer between the magnetic particles to ensure there is minimum level of interaction or coupling between them, even if they have physical contact. This would allow the nanoparticles to display largely non-interacting or a weakly interacting superparamagnetic response [18].
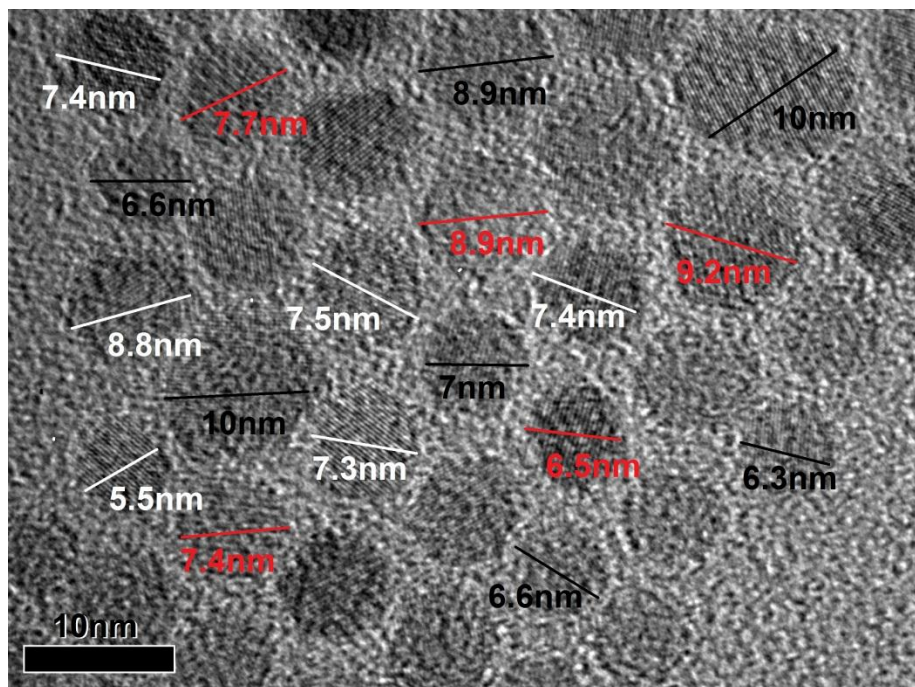
Figure 3.4 – High resolution (TEM) image of as-synthesized magnetite (Fe_3O_4) nanoparticles.

Figure 3.3 presents a high resolution TEM image of the Fe_3O_4 nanoparticles prepared on top of a TEM grid, indicating all the particles have a well-defined rounded shape. In addition, this TEM image also confirms the measured nanoparticle size distribution of 7.5±2nm. Aside from their shapes, a blurry region surrounding each nanoparticle can be observed in the magnified TEM image shown in Figure 3.5. The irregular shape of this blurry region could be ascribed to the presence of the surfactant coating on the particles instead of an effect caused by the particle interaction with the electron beam or possible lens aberration.
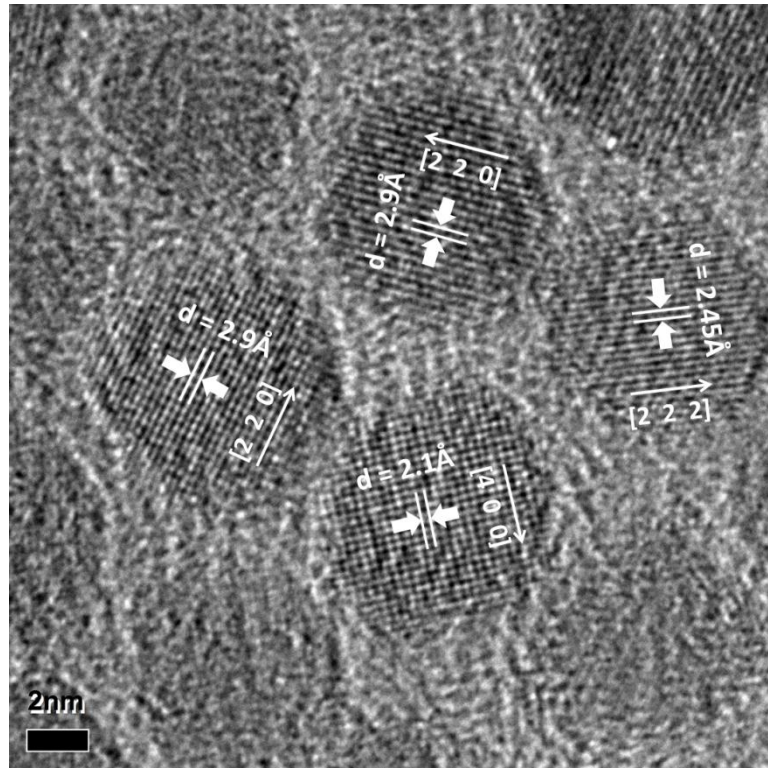
Figure 3.5 – Magnified high resolution (TEM) image of as-synthesized Fe_3O_4 nanoparticles, revealing the co-existence of different crystal orientation planes.

Figure 3.5 also shows the presence of the crystal orientation planes for the as-synthesized Fe_3O_4 nanoparticles. Interplanar distances were measured and compared with those reported by Hanawalt *et al.* [19]. The crystallographic orientation found in this image denotes the existence of [2 0 0], [4 0 0] and [2 2 2] planes, with interatomic spacing (d-spacing) of 2.9Å, 2.45Å and 2.1Å, respectively. As shown in Figure 3.5, each particle holds a different orientation of their crystal planes, which depicts that particle-to-particle interaction does not cause alignment of the particles in a specific direction. The suspended nanoparticles do not have a common crystal orientation as exhibited by bulk magnetic materials. This can explain why the effective magnetic properties of

nanocomposites are very difficult to specify and the presence of permeability and permittivity tensors is not easy to demonstrate or model.

3.5 Preparation and Characterization of PDMS-Fe$_3$O$_4$ Polymer Nanocomposites

The polymer matrix chosen for this work is Polydimethylsiloxane (PDMS) acquired from Dow Corning Corporation (also known as Sylgard® 184 elastomer kit), which is a two-component systems composed of a base resin and a curing agent. Detailed chemical compositions of the base resin and the curing agent in the elastomer kit are provided in Table 3.2 and Table 3.3, respectively [20].

Table 3.2 – Chemical composition of PDMS (Sylgard® 184, Dow Corning™) base resin.

Component Name	Concentration (by weight %)
Dimethyl siloxane dimethylvinyl-terminated	>60
Dimethylvinylated and trimethylated silica	30.0 – 60.0
Tetra(trimethylsiloxy) silane	1.0 – 5.0
Xylene	0.5
Ethylbenzene	< 0.10

Table 3.3 – Chemical composition of PDMS (Sylgard® 184, Dow Corning™) curing agent.

Component Name	Concentration (by weight %)
Dimethyl, methyhydrogen siloxane	55 .0 – 75.0
Dimethyl siloxane dimethylvinyl-terminated	15.0 – 35.0
Dimethylvinylated and trimethylated silica	10.0 – 30,0
Tetramethyl tetravinyl cyclotetrasiloxane	1.0 – 5.0
Xylene	0.19
Ethylbenzene	< 0.10

PDMS is chosen for this work because it simultaneously holds attractive mechanical and electrical properties (an elastomer is useful for the elaboration of

flexible electronics) while allowing ease of processing. In particular, Sylgard®

184 can be cured at low temperature (@90°C for 45min), safeguarding the

integrity of nanoparticles during the curing process.

The electrical properties of Sylgard 184 are presented in Table 3.4 [20].

Table 3.4 – Electrical properties of PDMS (Sylgard® 184, Dow Corning™) when a 10:1 mixing ratio of base resin to curing agent is applied.

Electrical Property	Value [units]
Dielectric Strength	14 [kV/mm]
Dielectric Constant @100KHz	2.68
Dielectric Constant @8GHz*	2.75*
Volume Resistivity	2.9×10^{14} [ohm-cm]
Dielectric Loss Tangent ($tan\delta_d$) @100KHz	0.0013
Dielectric Loss Tangent ($tan\delta_d$) @8GHz*	0.022*

*Data not provided by the manufacturer, which are measured with microstrip transmission-line test fixtures and techniques developed in this dissertation work.

As shown in Table 3.4, the high volume resistivity will help prevent the

generation of parasitic currents (current leakage) when this material is used as

the substrate material. Along with this characteristic, low dielectric constant

makes easier to obtain a matched magneto-dielectric condition ($\mu_r = \varepsilon_r$) with the

mixing with magnetic nanoparticles (i.e. magnetite nanoparticles).

Base resin and curing agent are mixed in a 10:1 ratio. A controlled amount

of this mixed two-component polymer was dissolved in hexane to decrease its

viscosity and facilitate the dispersion of Fe_3O_4 nanoparticles. A controlled amount

of dried nanoparticles is also suspended in hexane followed by vortex-agitation

for two minutes at 2200rpm along with two minutes of ultrasonication. Finally, the

polymer and nanoparticle solution are mixed in a glass vial at the desired

concentration, followed by vortex agitation for five minutes and ultrasonication for 4 minutes.

3.5.1 Characterization of PDMS-Fe$_3$O$_4$ Nanocomposites Using TEM

The TEM samples are prepared on copper formvar coated grids (FCF400-Cu) from Electron Microscope Sciences. One drop of the Fe$_3$O$_4$-PDMS nanocomposite solution was applied on the TEM grid, followed by evaporation of the solvent and curing at 90°C during four hours under 30 inHg of vacuum. Figure 3.6 presents the TEM image of the polymer nanocomposite, showing an excellent polymer-to-particle interaction. Nanoparticles tend to form islands, showing the existence of weak interactions between them. However, each nanoparticle can be individually observed and differentiated among the others, revealing the non-agglomeration of the particles while embedded in the polymeric matrix.

In order to confirm the good interaction between polymer matrix and nanoparticles, a new sample is prepared with slightly elevated concentration of particles. Figure 3.7 presents a HR-TEM image of the high loading concentration polymer nanocomposites, confirming the highly uniform dispersion of the particles in the polymer matrix. Given that the nanoparticles are covered by a layer of PDMS, it is very difficult to reach optimal focus on the particles, and thus the atomic crystal orientation of the particles is not easily observed.
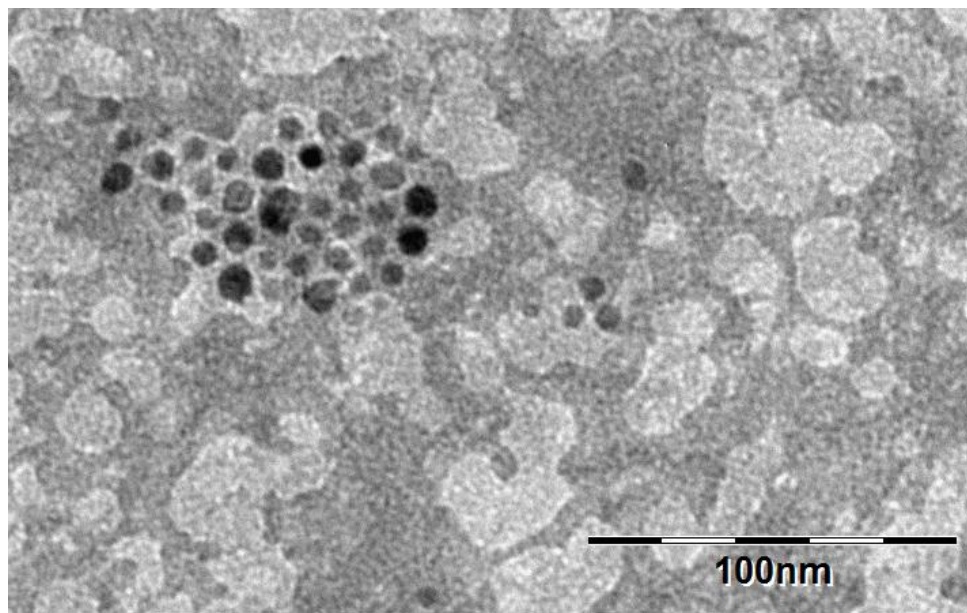
Figure 3.6 – TEM image of Fe_3O_4-PDMS polymer nanocomposite at relatively low particle loading concentration.
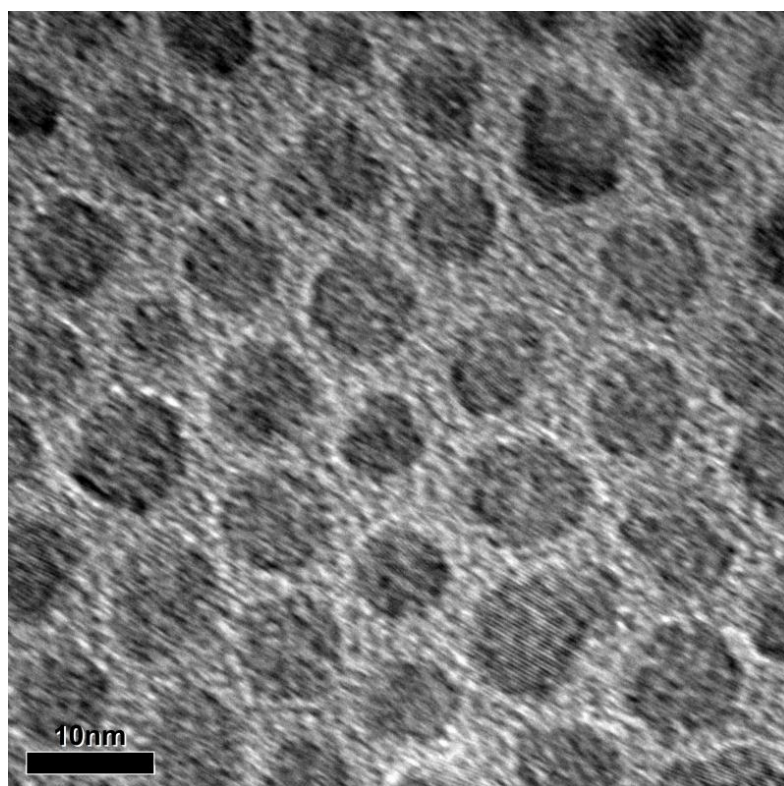
Figure 3.7 – High resolution (TEM) image of Fe_3O_4-PDMS polymer nanocomposite with high particle loading concentration.

3.5.2 Characterization of the Magnetic Properties of Fe_3O_4 Nanoparticles Using a Physical Properties Measurement System (PPMS)

Magnetization measurements were conducted over the plain magnetite (Fe_3O_4) nanoparticles and magneto-dielectric PDMS-Fe_3O_4 polymer nanocomposites with 30%, 50% and 80% magnetite loading concentrations by weight (w.t.). The commercial Physical Property Measurement System (PPMS) model 6000 from Quantum Design was used for this experiment. The measurements were carried out at the Functional Material Laboratory, University of South Florida, with the collaboration of Dr. Hariharan Srikanth and Kristen Stojak. Figure 3.8 presents the measured magnetization curves for all the four materials, under the presence of magnetic field in the range of -60kOe to +60kOe and ambient-like temperature conditions (300°K).
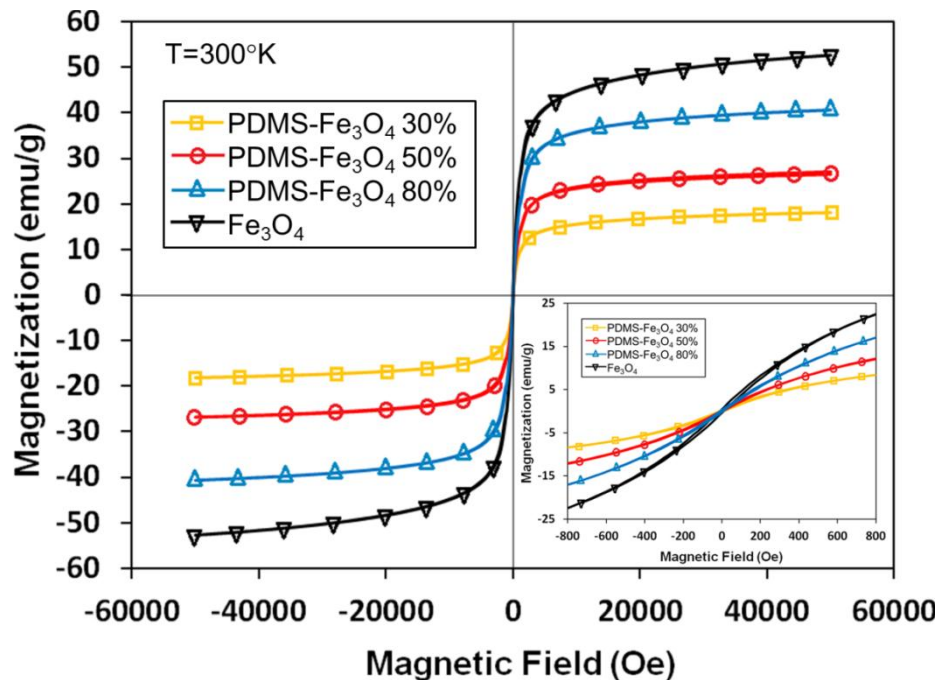
Figure 3.8 – Magnetization curves for as-synthesized magnetite (Fe_3O_4) nanoparticles and the PDMS-Fe_3O_4 polymer nanocomposites at different concentrations (30%, 50% and 80% w.t.). The inset on the lower right corner presents the expanded view of the low field region.

The inset in the lower right corner depicts the absence of magnetic hysteresis at ambient temperature (300°K) under all three particle loading concentrations, confirming the retention of superparamagnetism for all the materials under test. This is a highly desirable condition that is crucial for low loss RF/microwave materials. Such a property can only be realized through a combination of effective nanoparticle surface functionalization, homogenous nanoparticle dispersion and excellent interaction between the nanoparticles and the PDMS matrix. Furthermore, saturation magnetization (M_S) values were extracted from magnetization curves, leading to a M_S of 81emu/g for plain Fe_3O_4 nanoparticles. Besides, the PDMS-Fe_3O_4 nanocomposites at 80%, 50% and 30% loading concentrations have exhibited M_S values of 40.44emu/g, 27.06emu/g and 18.12emu/g, respectively. The increase of the M_S with incremented particle loading concentration, was expected to occur given the increasing of the magnetic material volume concentration in the PNCs [14][16].

To complete the magnetic characterization, magnetization vs. temperature measurements were also carried out in the temperature range from 10°K to 300°K and vice versa. Both field cooled (FC) and zero field cooled (ZFC) measurements were carried out as they provided relevant material characteristics; specifically, the blocking temperature (T_B) for the nanoparticles and polymer nanocomposite systems corresponds to the temperature where the maximum of the ZFC curve occurs. The blocking temperature T_B of the nanoparticles marks the temperature above which the particles are superparamagnetic. It is therefore critical to keep the blocking temperature below

the ambient temperature, under which most of the electronics and RF and microwave devices operate. Furthermore, other information details concerning to the nanoparticle size distribution, particle to particle interaction and nanoparticle clustering could be inferred from the FC and ZFC measurement results.

T_B of a single domain particle can be described as follows [16]:

$$T_B = \frac{KV}{25k_B}$$ (3.1)

where K is the magnetocrystalline anisotropy, V is the volume of the nanoparticle and k_B is the Boltzmann constant. As T_B is related to the volume of the nanoparticles, the peak width at the ZFC curve is related to the relaxation time distribution and correspondingly to the particle size distribution in the sample [16].

Many studies have revealed the increase of T_B when the average inter-particle distance is decreased, which could be ascribed to dipolar interactions between the particles [16]. This also opens the possibility of widening of the ZFC peak due to the presence of a small amount of nanoparticles clustering. In this case, the agglomerated particles must be small enough to maintain single-domain systems, thus allowing the retention of superparamagnetic properties for the bulk material.

Figure 3.9 depicts the FC and ZFC curves at 200Oe of externally applied magnetic field obtained from plain Fe_3O_4 nanoparticles. The results presented in this figure are characteristic of a single domain nanoparticle system with a blocking temperature T_B=81°K. The data shown in Figure 3.9 along with the hysteresis loop measurements, demonstrate that the Fe_3O_4 nanoparticle system

studied by this work retains superparamagnetic properties at ambient temperature (300°K).
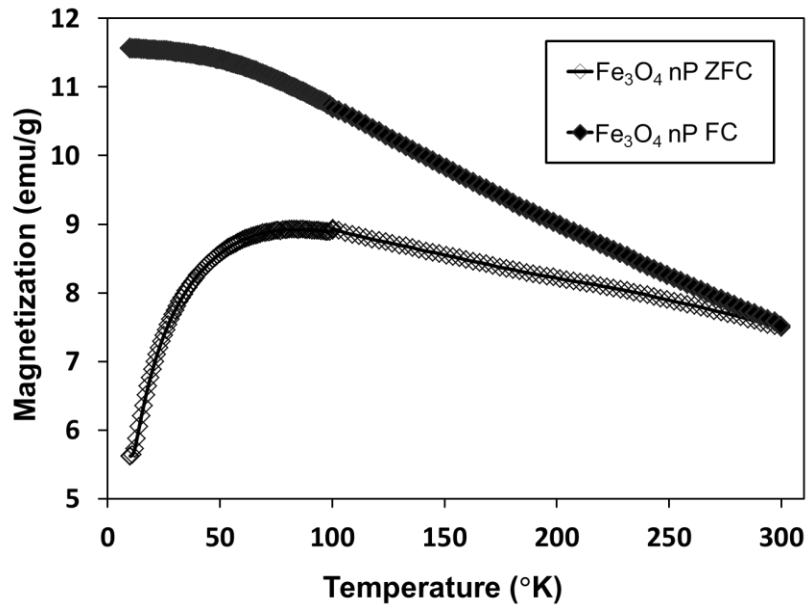
Figure 3.9 – Field Cooled (FC) and Zero-Field Cooled (ZFC) curves under 200Oe of applied magnetic field for plain Fe_3O_4 nanoparticles. ZFC curve presents a peak indicating a blocking temperature T_B of 81°K.

Figure 3.10 depicts the FC and ZFC curves at 200Oe for the PDMS-Fe_3O_4 polymer nanocomposites at 30% w.t. concentration. Results presented in this plot are characteristic of a single domain nanoparticle system with blocking temperature T_B=51.86°K. This data along with the hysteresis loop measurements demonstrate that the Fe_3O_4 nanoparticle system at the aforementioned concentration retains superparamagnetic properties at ambient temperature (300°K), while being embedded in the PDMS matrix. The reduction of the T_B value as compared to that of the plain magnetite may be due to the increment of the inter-particle distance, thus leading to a weak magnetic interaction between the Fe_3O_4 nanoparticles.
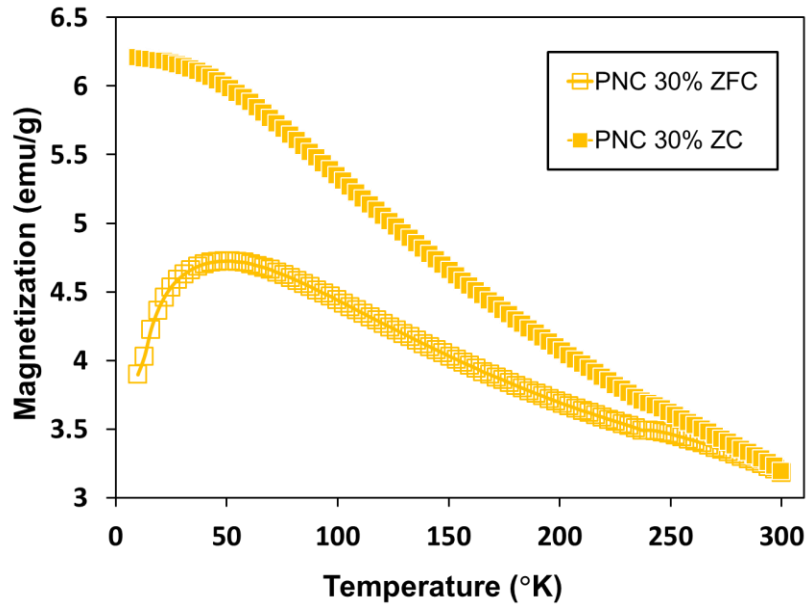
Figure 3.10 – Field Cooled (FC) and Zero-Field Cooled (ZFC) curves at 200Oe for PDMS-Fe$_3$O$_4$ polymer nanocomposites at 30% w.t. concentration. ZFC curve presents a peak indicating a blocking temperature T_B of 51.86°K.
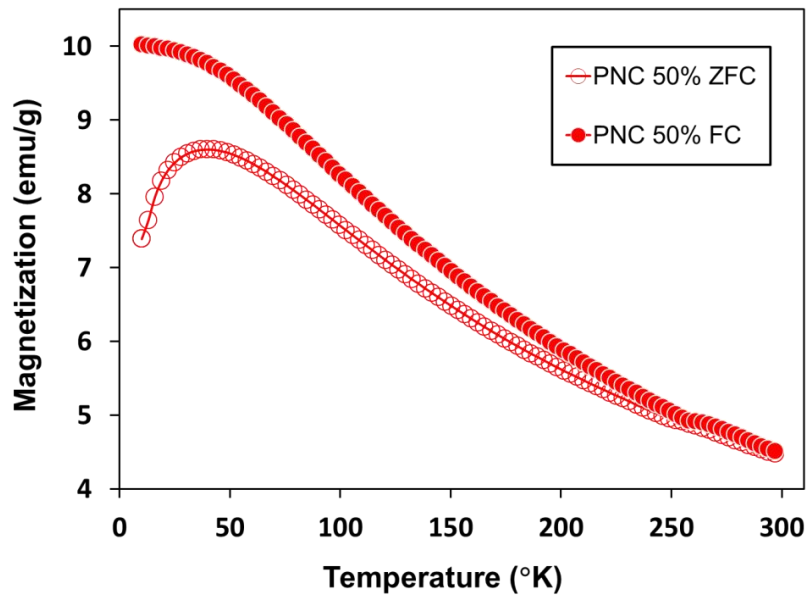
Figure 3.11 – Field Cooled (FC) and Zero-Field Cooled (ZFC) curves at 200Oe for PDMS-Fe$_3$O$_4$ polymer nanocomposites at 50% w.t. concentration. ZFC curve presents a peak indicating a blocking temperature T_B of 39.92°K.

Figure 3.11 depicts the FC and ZFC curves at 200Oe for the PDMS-Fe$_3$O$_4$ polymer nanocomposites at 50% w.t. concentration. Results presented in this plot reveal the measured magnetization vs. temperature characteristic of a single domain nanoparticle system with T_B=39.92°K, confirming the retention of superparamagnetic properties at ambient temperature (300°K) while being embedded in the PDMS matrix. Although a higher value for T_B was expected for this nanoparticle loading concentration, given the reduction of inter-particle spacing as the particle loading was increased, the measured blocking temperature is lower to that of PNC at 30% w.t. concentration. This may be due to the presence of some nanoclusters in the PNC at 30% w.t. concentration which leads to a higher blocking temperature as compared with the PNC at 50% concentration [21].
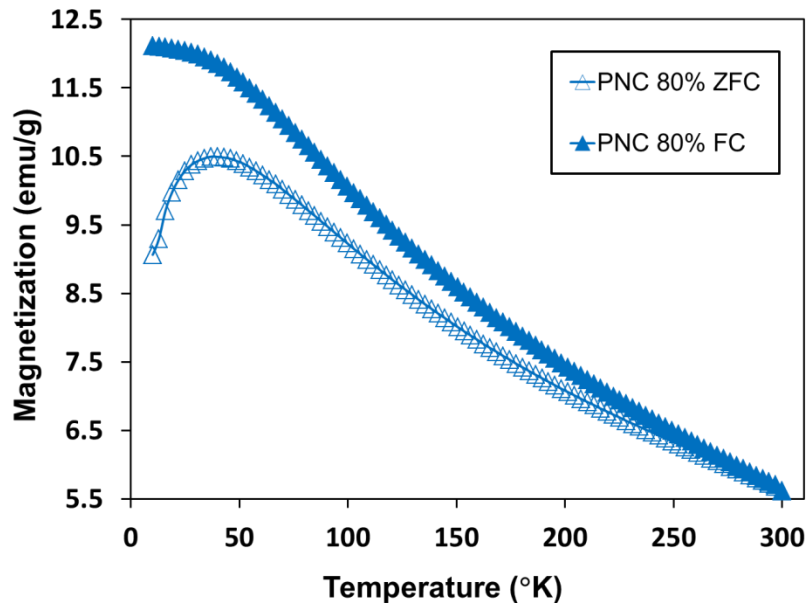
Figure 3.12 – Field Cooled (FC) and Zero-Field Cooled (ZFC) curves at 200Oe for PDMS-Fe$_3$O$_4$ polymer nanocomposites at 80% w.t. concentration. ZFC curve presents a peak indicating a blocking temperature T_B of 36.91°K.

Figure 3.12 presents the FC and ZFC curves at 200Oe for the PDMS-Fe$_3$O$_4$ polymer nanocomposites at 80% w.t. concentration, which correlates to the highest concentration of nanoparticles in the PDMS polymer matrix studied in this work. This newly-engineered nanocomposite system presented of a single domain nanoparticle system with blocking temperature T_B=36.91°K, retaining superparamagnetic behavior at ambient temperature (300°K). In this case, the blocking temperature is very close to the 39.92°K obtained from the PNC at 50% w.t. concentration. Also here, a higher value for T_B was expected for the PNC at 80% w.t. concentration given a higher density of more proximity of the nanoparticles as compared with the PNC 50% w.t. and PNC 30% w.t. systems. However, less nanoclustering may be present at this concentration, thus leading to a lower blocking temperature [21].
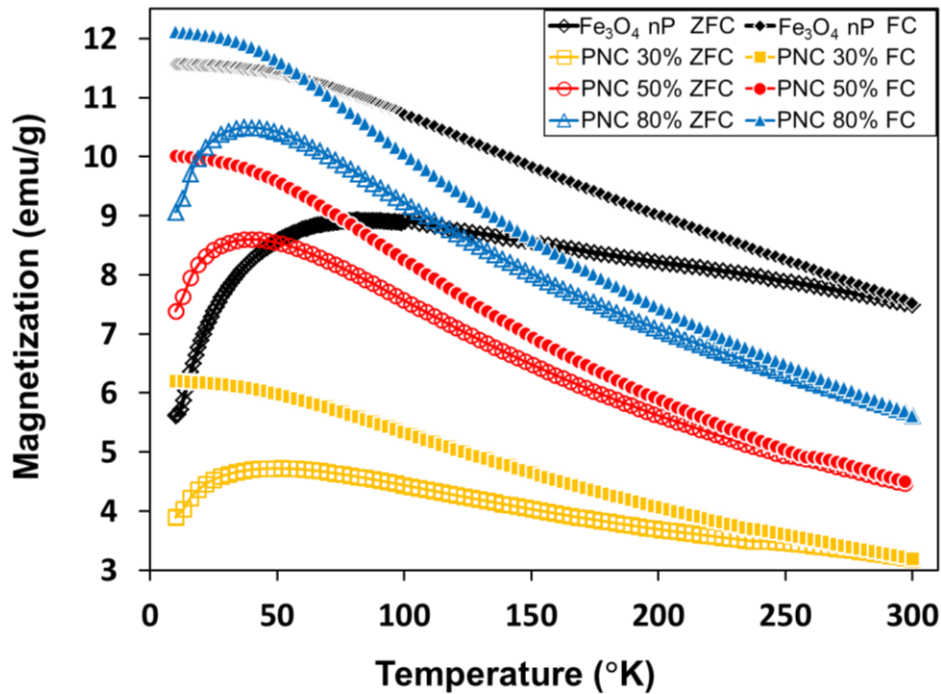
Figure 3.13 – Comparison of the FC and ZFC curves at 200Oe for plain Fe$_3$O$_4$ and PDMS-Fe$_3$O$_4$ polymer nanocomposites with particle loading concentrations of 30% w.t., 50% w.t. and 80% w.t., respectively.

Figure 3.13 presents a direct comparison of the FC and ZFC curves for pure Fe_3O_4 nanoparticles and Fe_3O_4-PDMS nanocomposites at all three different Fe_3O_4 nanoparticle loading concentrations. The plot clearly shows the consistency of the value for the blocking temperature T_B for all three polymer nanocomposites studied in this work, which are moderately lower from the blocking temperature T_B obtained from the plain Fe_3O_4 bulk system. In addition, the peak is noticeably narrower for the polymer nanocomposite systems than for plain bulk Fe_3O_4. As all material systems shared identical particles with the same size distribution and prepared from the same synthesis batch, these results indicate that the PDMS polymer matrix enabled uniform and well controlled particle dispersion, thus weakening the dipolar interaction between the Fe_3O_4 nanoparticles.

Table 3.5 summarizes the saturation magnetization and blocking temperatures for the Fe_3O_4 nanoparticles and the PDMS-Fe_3O_4 polymer nanocomposites at all three aforementioned particle loading concentrations.

Table 3.5 – Blocking temperatures and saturation magnetization for the Fe_3O_4 nanoparticles and PDMS-Fe_3O_4 PNCs.

Sample	Blocking Temperature T_B (°K)	Saturation Magnetization M_S (emu/g)
Plain Magnetite (Fe_3O_4)	81	52.69
PDMS-Fe_3O_4 PNC 80% w.t	36.91	40.44
PDMS-Fe_3O_4 PNC 50% w.t	39.92	27.06
PDMS-Fe_3O_4 PNC 30% w.t	51.86	18.12

Chapter 4

Characterization and Extraction of Complex Permeability and Permittivity of

Magnetite-Based Polymer Nanocomposites at Microwave Frequencies

4.1 Introduction

This chapter explains in detail how classical techniques, such as the

Nicolson-Ross-Weir and Barker Jarvis methods, were adapted and jointly used

for custom-built multilayer microstrip test structures. Through these techniques,

the electrical properties of magneto-dielectric nanocomposite materials were

extracted and explored.

4.2 Characterization and Extraction of Microwave Properties Using Microstrip

Transmission Line Test Fixtures

Two-port microstrip-based test fixtures were designed to study the

microwave properties of the polymer nanocomposite as described in [14]. These

devices were designed to extract the properties of the material under the

influence of an external transverse magnetic field, as shown in Figure 4.1.

Nonmagnetic SMA connectors and cables were used to avoid unwarranted

motion, as well as any interference during measurements. In addition, a DC

magnetic flux meter was used to measure the magnetic field $\vec{B}$ applied to the

sample [14].
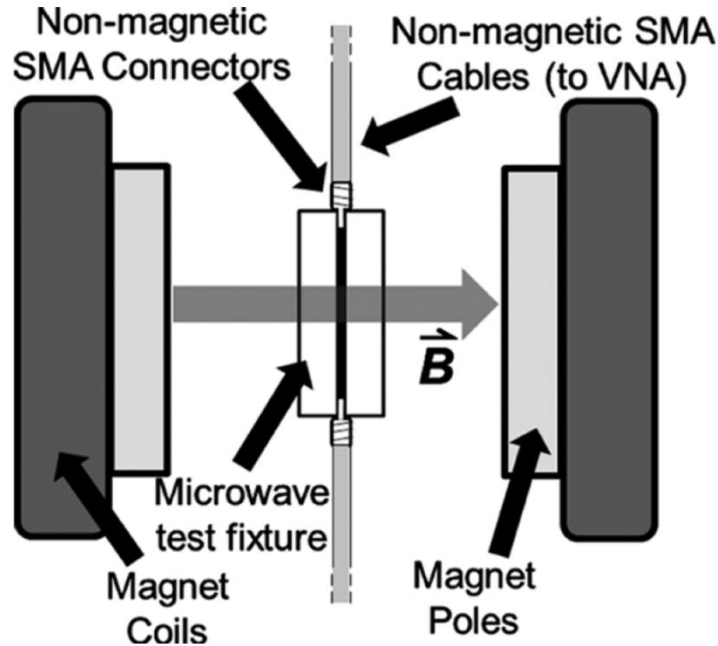
Figure 4.1 – Schematic of two-port microwave test setup with fixed electromagnet. From Morales *et al.* [14].

The test fixtures consist of multilayer structures that include an embedded cavity filled with the nanocomposite material. They were constructed by bonding two printed circuit board (PCB) laminates together, as shown in Figure 4.2. The laminate used was Rogers RT/Duroid 6010LM (ε_r = 10.2, $tan\delta_d$=0.0023) with a thickness of 635μm, which offers a high dielectric constant that helps increasing the electrical length of the microstrip transmission line, thus providing higher sensitivity in the extraction of permeability and permittivity of the polymer nanocomposite material. The nanocomposite polymer is deposited in the 435μm cavity (bottom laminate) using a volumetric syringe. The required volume for solvent-diluted nanocomposite polymer to completely fill the embedded cavity is determined by taking into account the amount of hexane, a solvent that dissolves the polymer nanocomposite. The amount of solvent that will evaporate is

considered in the total volume calculation of the applied material. After curing, profilometer measurements demonstrated a difference of less than 0.5μm between the heights of the substrate and the deposited material [14].
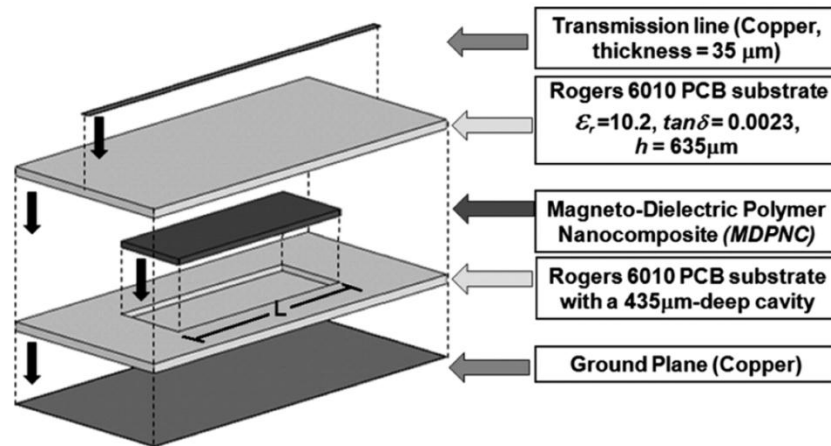
Figure 4.2 – 3D perspective-view schematic of the multilayer microstrip test fixture for extraction of the microwave properties of the magneto-dielectric polymer nanocomposites. From Morales *et al.* [14].

Thereafter, the bottom laminate containing the sample was heated in a vacuum oven at 90°C and 27inHg of vacuum for 4 hours to cure the composite materials. The vacuum is applied in order to prevent oxidation or annealing of the sample. Thus, it would be beneficial to purge the oven using Nitrogen or Argon gas before vacuum is applied. Finally, the top laminate is attached to the bottom one using a very thin layer of epoxy while applying vacuum to avoid air trapping or bubble formation. PCB edge-mount connectors were solder-attached to each end of the fixture [14].

Room-temperature S-parameter measurements covering 1–8 GHz were carried out using the thru-reflect-line (TRL) calibration procedure. Six microstrip lines were designed to carry out the calibration procedure. These lines

correspond to four delay-lines of different lengths, one thru-line and one open-line. All the calibration standards were designed over a Rogers RT/Duroid 6010LM with thickness of 1.27mm, and 50Ω copper microstrip lines with thickness of 35μm and width of 1.2mm. The lengths and operational frequencies of the calibration standards are described in Table 4.1. The calibration was verified by measuring the thru-line, obtaining S_{11} and S_{22} below -35dB, S_{21} and S_{12} between $\pm$ 0.05dB. Also the open-line was measured obtaining S_{11} of 0dB for frequencies below 5.5GHz and a decreased response always above -0.25dB for frequencies up to 8GHz. Finally the delay lines were used to validate the calibration by comparing the measured and simulated results of the phase of S_{21}, obtaining excellent agreements.

Table 4.1 – TRL calibration standards on Rogers RT/Duroid 6010LM.

Standard Description	Length (mm)	Operational Frequency
Delay 1	51.53	1GHz-1.327GHz
Delay 2	37.09	1.327GHz-2.635GHz
Delay 3	29.86	2.635GHz-5.179GHz
Delay 4	26.24	5.179GHz-8GHz
Thru-line	22.6	1GHz-8GHz
Open	11.3	1GHz-8GHz

Using the described TRL calibration procedure, the reference planes were set at the edge of the embedded cavity to avoid uncertainty caused by the carrier

substrate and connectors. The measured scattering parameters of the fixtures were subsequently used to extract the microwave properties of the engineered nanocomposite material. For the extraction step, the Nicolson–Ross–Weir formulation along with a conformal mapping method to determine analytical values for the filling factors of the multilayer structure were used [22]-[35], as explained next.

4.2.1 Extraction of the Dielectric/Magnetic Parameters of the Nanocomposite Material Using Multilayer Microstrip Line Test Fixtures

The propagation factor for an electromagnetic wave propagating through the area delimited between the reference planes of the test fixture, as shown in Figure 4.3, is defined as:

$$P = e^{-\gamma L} = e^{-(\alpha + j\beta)L} \tag{4.1}$$

where γ is the propagation constant, α is the attenuation constant, and β is the phase constant which is equal to

$$\beta = \frac{2\pi}{\lambda_g} \tag{4.2}$$

where λ_g is the guided wavelength. ε_r and μ_r are defined in terms of their real and imaginary parts as:

$$\varepsilon_{\text{eff}} = \varepsilon'_{\text{eff}} - j\varepsilon''_{\text{eff}} \tag{4.3}$$

$$\mu_{\text{eff}} = \mu'_{\text{eff}} - j\mu''_{\text{eff}} \tag{4.4}$$

Considering the basic principle implemented by Nicolson, Ross, and Weir, if L were infinite, then the reflection coefficient of a wave incident on the interface from the dielectric substrate would be defined by [22] [23]:

$$\Gamma = \frac{Z_2 - Z_1}{Z_2 + Z_1} = \frac{\sqrt{\mu_{eff2}/\varepsilon_{eff2}} - \sqrt{1/\varepsilon_{eff1}}}{\sqrt{\mu_{eff2}/\varepsilon_{eff2}} + \sqrt{1/\varepsilon_{eff1}}} \tag{4.5}$$

where ε_{eff1} and μ_{eff1} are the effective values for the structure conformed by the Rogers 6010LM substrate, ε_{eff2} and μ_{eff2} are the effective values of the multilayer structure composed of two layers of Rogers 6010LM and one layer of magnetic polymer nanocomposites. Figure 4.3 presents a simplified schematic diagram of the measurement fixture. Note that the carrier substrate is a nonmagnetic material (μ_{eff1} = 1), whereas ε_{eff1} can be calculated for a microstrip line based on its geometry and the microwave properties of the substrate material, including the effects of frequency dispersion [24][25]. Γ is also obtained from the S-parameters for a sample with finite length L [22]:

$$\Gamma = \chi \pm \sqrt{\chi^2 - 1} \tag{4.6}$$

where

$$\chi = \frac{S_{11}^2 - S_{21}^2 + 1}{2S_{11}} \tag{4.7}$$

The appropriate sign must be chosen so that $|\Gamma| \leq 1$.
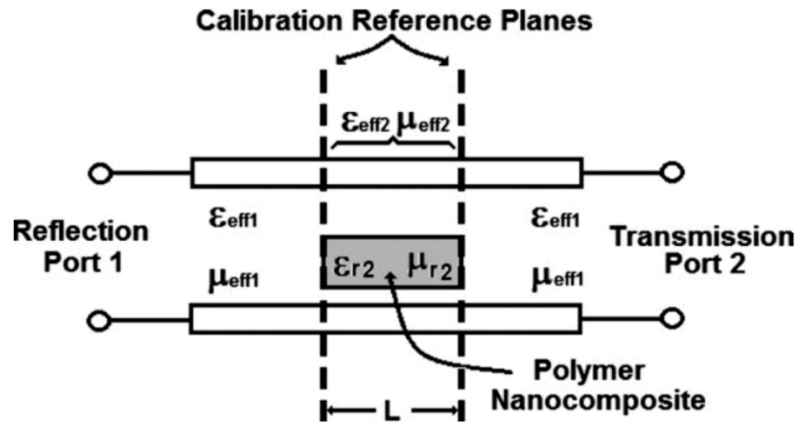
Figure 4.3 – Schematic diagram of the measurement fixture. The reference planes were located at the boundaries of the cavity filled with polymer nanocomposites. From Morales *et al.* [14].

The propagation factor can be found from the *S*–parameters and Γ as follows [22]:

$$P = \frac{S_{11} + S_{21} + \Gamma}{1 - (S_{11} + S_{21})\Gamma} \tag{4.8}$$

Now, from Equation (4.5):

$$\frac{\mu_{\text{eff2}}}{\varepsilon_{\text{eff2}}} = \left(\frac{1+\Gamma}{1-\Gamma}\right)^2 \frac{1}{\varepsilon_{\text{eff1}}} = c_1 \tag{4.9}$$

Complex effective permeability and permittivity can be related to the propagation constant P as [23] :

$$\mu_{\text{eff2}}\varepsilon_{\text{eff2}} = -\left[\frac{c}{2\pi f L} \ln\left(\frac{1}{P}\right)\right]^2 = c_2 \tag{4.10}$$

where f is the frequency in hertz. From Equations (4.9) and (4.10):

$$\mu_{\text{eff2}} = \sqrt{c_1 c_2} \tag{4.11}$$

$$\varepsilon_{\text{eff2}} = \sqrt{\frac{c_2}{c_1}} \tag{4.12}$$

As mentioned by Weir [22], Equation (4.8) is ambiguous and has an infinite number of roots because the phase of the propagation factor P does not change when the length of the section, that includes the composite material under test and the Rogers 6010LM, is increased by a multiple of $\lambda_{\text{g}}/2$. However, this situation can be resolved by finding the correct roots. The group delay at each frequency is computed for each solution of $\varepsilon_{\text{eff2}}$ and μ_{eff2} by assuming that their changes are negligible over small increments of frequency [23]

$$\tau_{\text{gn}} = L \cdot \frac{d}{df}\left(\left\{\frac{\varepsilon_{\text{eff2}}\mu_{\text{eff2}}}{[c/(2\pi f)]^2}\right\}^{1/2}_n\right) \tag{4.13}$$

τ_{gn} is the group delay in seconds for the nth solution of Equations (4.11) and (4.12). In addition, the measured group delay based on the slope of the phase of the propagation factor versus frequency can be calculated [23]:

$$\tau_g = \frac{1}{2\pi}\left(\frac{d(-\phi)}{df}\right) \tag{4.14}$$

where ϕ is the phase of the propagation factor P from Equation (4.8) in radians. The correct roots, $n = k$, are selected when the following condition is satisfied [23]:

$$\left|\tau_{gn} - \tau_g\right| \cong 0 \tag{4.15}$$

Using the aforementioned procedure, the equations are algebraically unstable as $S_{11} \to 0$, which occurs at frequencies corresponding to integer multiples of $\lambda_g/2$. In addition, for small $|S_{11}|$, the VNA phase uncertainty is large and small calibration plane positioning errors can cause large inaccuracies in the S_{11} phase [26]. This inaccuracy is significantly bypassed by the implementation of a two-port calibration in conjunction with the execution of an iterative algorithm. Discontinuities generated by the instability of the Nicholson–Ross–Weir method were eliminated and replaced by iteratively calculated values of ε_{eff2} and μ_{eff2} that satisfy Equations (4.6) to (4.12) with the measured S-parameters and the consequently derived Γ and P values. The solutions derived from the Nicholson–Ross–Weir method at the starting discrete frequency are used as initial iterative values, and then the new calculated values are used as the initial iteration values for the next frequency. A similar procedure is proposed by Barker-Jarvis *et al.* [26].

Relative permittivity (ε_r) and permeability (μ_r) of the polymer nanocomposites are derived from the extracted ε_{eff2} and μ_{eff2} values. Microwave properties of multilayer microstrip lines have been investigated by various methods such as variational calculus [27] and Green's functions [28]. Even though both methods provide accurate results, they require long computational times. On the contrary, the conformal mapping method presents a simple set of analytical equations for the filling factors and the effective permittivity of multilayer microstrip. Moreover, this method can be extended to have equivalent expressions for multilayer substrates with magnetic properties, as shown by Pucel and Masse [29]. Each individual section of the substrate must be linear, homogenous, and isotropic. For this particular case, the fabricated test structure is a three-layer microstrip structure, as shown in Figure 4.4.
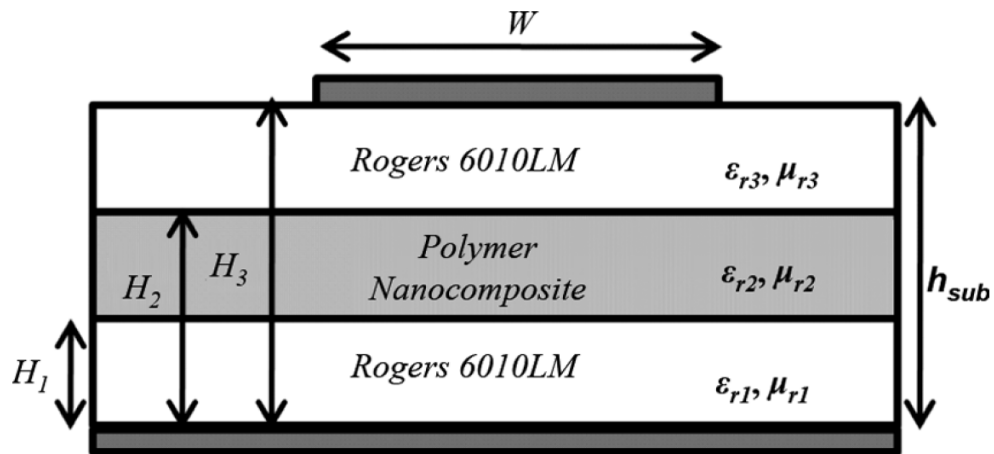
Figure 4.4 – Cross-sectional diagram of the multilayer microstrip. From Morales *et al.* [14].

The filling factors of the dielectric layers are obtained for a narrow microstrip line with $W/h_{sub} \leq 1$ based on the geometrical configuration of the microstrip cell [30]-[32]:

$$q_1 = \frac{\ln A_1}{2\ln(8h_{\text{sub}}/W)}\left[1 + \frac{\pi}{4} - \frac{1}{2}\arccos\left(\frac{W}{8h_{\text{sub}}H_1} \cdot \sqrt{A_1}\right)\right] \qquad (4.16)$$

$$q_2 = \frac{\ln A_2}{2\ln(8h_{\text{sub}}/W)}\left[1 + \frac{\pi}{4} - \frac{1}{2}\arccos\left(\frac{W}{8h_{\text{sub}}H_2} \cdot \sqrt{A_2}\right)\right] \qquad (4.17)$$

$$q_3 = \frac{1}{2} + \frac{0.9}{\pi \cdot \ln(8h_{\text{sub}}/W)} - q_2 \qquad (4.18)$$

where A_i is given by:

$$A_i = \frac{1 + H_i}{1 - H_i + W/(4h_{\text{sub}})} \qquad (4.19)$$

The effective permittivity in a three-layer microstrip line is given by [31] :

$$\varepsilon_{\text{eff}} = \frac{\left(\sum_{i=1}^3 q_i\right)^2}{\sum_{i=1}^3 \frac{q_i}{\varepsilon_{ri}}} \qquad (4.20)$$

where $\varepsilon_{r1} = \varepsilon_{r3}$ is the complex permittivity of the Rogers 6010LM. The equivalent equations for permeability are obtained from the same expressions using duality relationships for dielectric and magnetic substrates, which are derived from the duality of ε and $1/\mu$ in Maxwell's equations and are based on a TEM-mode approximation for the magnetic case [27][30]. The relation then takes the form [29]:

$$\mu_{\text{eff}}\left(\frac{W}{h}, \mu\right) = \frac{1}{\varepsilon_{\text{eff}}(W/h\,,\,\mu^{-1})} \qquad (4.21)$$

Using this set of equations, permeability and permittivity of the polymer nanocomposite $(\mu_{r2}, \varepsilon_{r2})$ were calculated iteratively, until $\varepsilon_{\text{eff}} = \varepsilon_{\text{eff2}}$ and $\mu_{\text{eff}} = \mu_{\text{eff2}}$ following the algorithm described in Figure 4.5. Thereafter, the independent dielectric and magnetic loss tangents are obtained from the extracted parameters

$$tan\delta_d = \frac{\varepsilon_{r2}''}{\varepsilon_{r2}'} \qquad (4.22)$$

$$tan\,\delta_{\mathrm{m}} = \frac{\mu''_{\mathrm{r2}}}{\mu'_{\mathrm{r2}}} \tag{4.23}$$

Also, the combined magneto-dielectric loss tangent is found as:

$$tan\delta = \frac{\delta''_{\mathrm{r}}}{\delta'_{\mathrm{r}}} \tag{4.24}$$

where

$$\delta'_{\mathrm{r}} = \mu'_{\mathrm{r2}}\varepsilon'_{\mathrm{r2}} - \mu''_{\mathrm{r2}}\varepsilon''_{\mathrm{r2}} \tag{4.25}$$

and

$$\delta''_{\mathrm{r}} = \mu'_{\mathrm{r2}}\varepsilon''_{\mathrm{r2}} - \mu''_{\mathrm{r2}}\varepsilon'_{\mathrm{r2}} \tag{4.26}$$
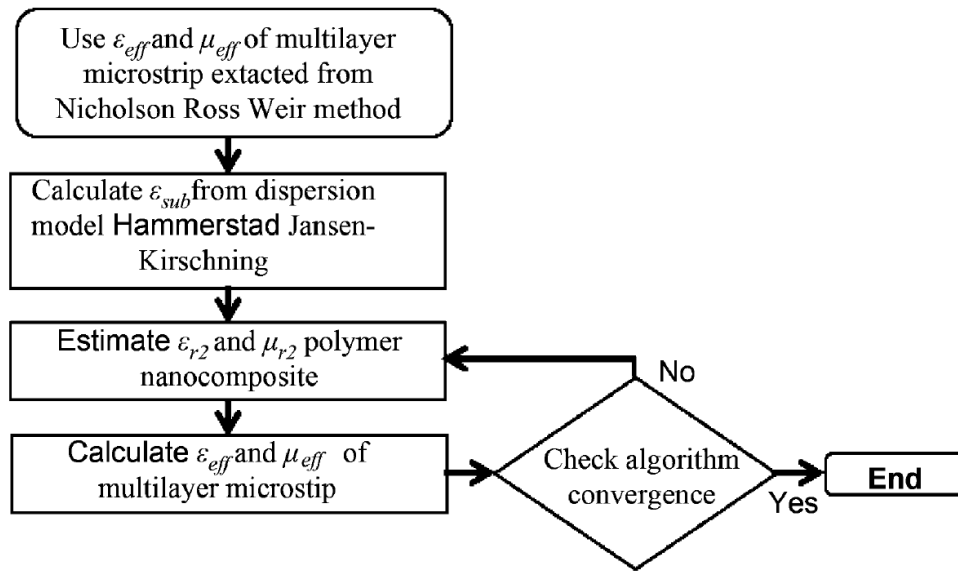
Figure 4.5 – Flux diagram for the iterative calculations of ε_r and μ_r. From Morales *et al.* [14].

This method has been tested using electromagnetic simulation software (Ansoft HFSS v11.1) for the extraction of properties of different magneto-dielectric materials ($\varepsilon_{\text{eff}} > 1$, $\mu_{\text{eff}} > 1$) obtaining errors of less than 3%.

Uncertainty derived from the *S*-parameter measurements affects only the determination of the effective material properties for the multilayer structure and

has been calculated by Baker-Jarvis *et al.* [26]. In [31] and [32], Svacina demonstrated that the results obtained by using his conformal mapping method differed by less than 2% from those obtained by Farrar *et al.* whom started from the numerical determination of Green's functions [28].

4.3 Extracted Dielectric/Magnetic Properties of the PDMS-Fe$_3$O$_4$ Polymer Nanocomposites at Microwave Frequencies

Using the procedure described in section 4.2, the electrical properties of the PDMS-Fe$_3$O$_4$ PNCs were extracted, with and without the application of external magnetic biasing fields.

4.3.1 Electrical Properties without Applied Magnetic Field

Figures 4.6 to 4.9 present the extracted relative permittivity, relative permeability, dielectric loss tangent and magnetic loss tangent versus frequency, for plain PDMS and magneto-dielectric PNCs at 80%, 50%.and 30% w.t. concentrations.
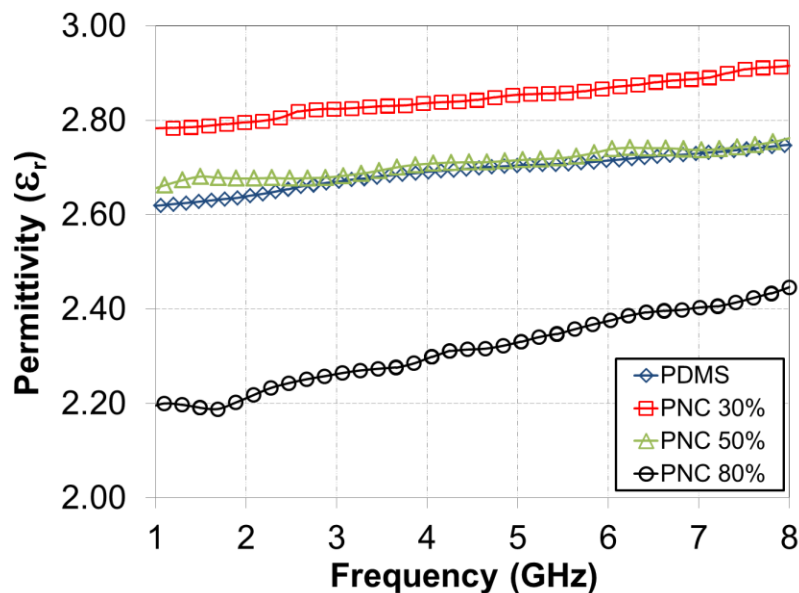
Figure 4.6 – Extracted permittivity for PDMS and magneto-dielectric PNCs without applied magnetic field.

The polymer matrix without nanoparticles fillers (i.e., plain PDMS) exhibits a relative permittivity in the range of 2.6 to 2.75, very similar to that obtained for the 50% PNC, but lower than the value obtained for 30% PNC, contained in the range of 2.8 to 2.9. Contrary to expectations, the trend of the permittivity versus nanoparticle concentration shows an increased value in this property when the concentration is below 50%. Beyond 50% the permittivity exhibits lower values than those obtained in the polymeric matrix without nanoparticle fillers, presenting the lower measured relative permittivity in the range of 2.2 to 2.43 for the 80% PNC. This trend may result from the increase in the bulk conductivity of the PNC when the concentration is increased, and can be ascribed to a possible slight oxidation of the nanoparticles in the PDMS matrix.
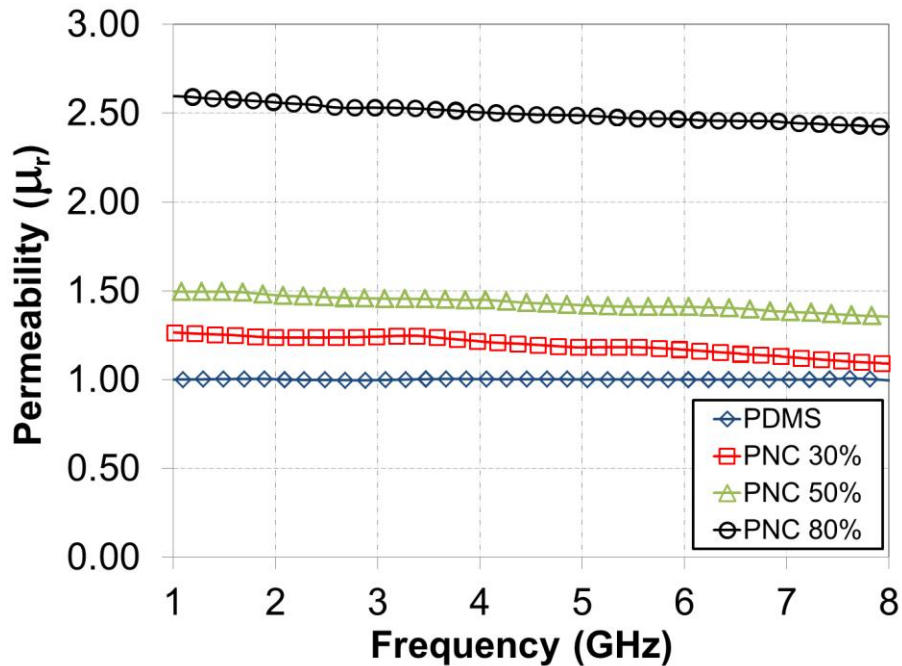
Figure 4.7 – Extracted permeability for PDMS and magneto-dielectric PNCs without applied magnetic field.

Figure 4.7 shows how the relative permeability increases with the augmentation of nanoparticle concentration in the PNCs. The retention of the relative permeability values at high frequencies is a new feature not often experienced with the magnetic materials available for the elaboration of RF and microwave devices. For the 80% PNC, a relative permeability with a magnitude around 2.6 is observed at 1GHz, without substantial degradation at higher frequencies, retaining a magnitude of approximately 2.4 at 8GHz. Another attractive characteristic is that relative permeability and permittivity are very close in magnitude for the 80% PNC, opening the possibility of fabrication of antennas with matched magneto-dielectric condition.
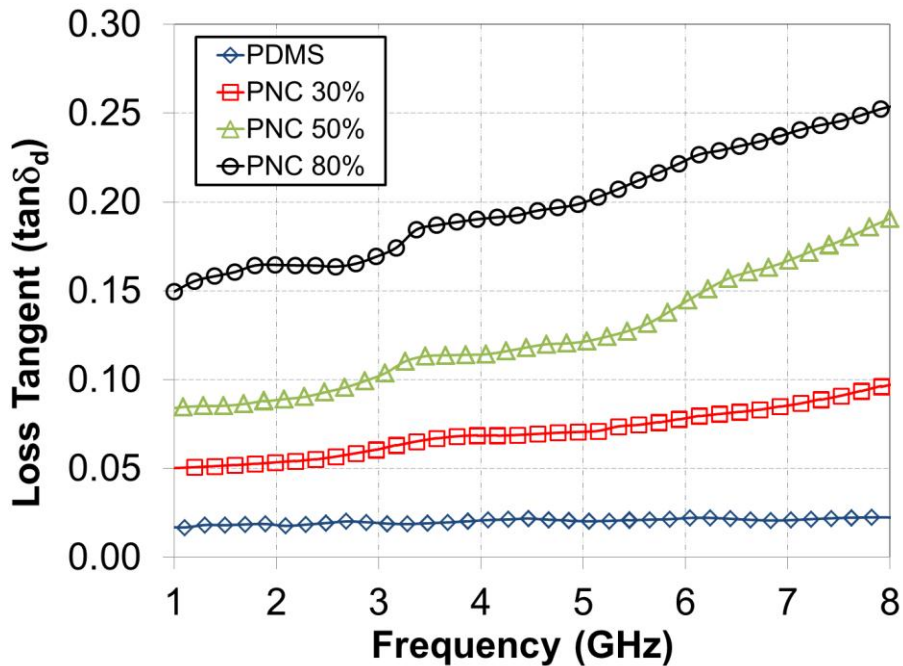
Figure 4.8 – Extracted dielectric loss tangent for PDMS and magneto-dielectric PNCs without applied magnetic field.
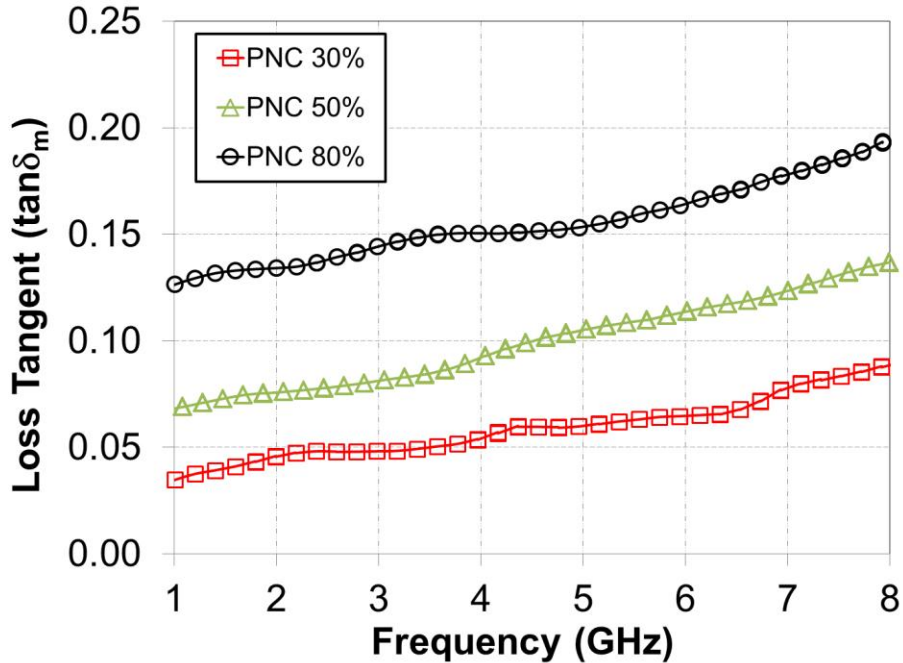
Figure 4.9 – Extracted magnetic loss tangent for PDMS and magneto-dielectric PNCs without applied magnetic field.

As observed in Figures 4.8 and 4.9, both dielectric and magnetic losses for the PNCs slightly increase with frequency as expected. However, there is no substantial augmentation of these losses with the increase of the operational frequency, a factor that allows for implementation of PNCs at higher frequencies than those permitted by conventional bulk magnetic materials.

4.3.2 Electric Properties of PDMS-Fe_3O_4 PNCs at 30% w.t. Concentration with External DC Magnetic Biasing Field Applied

Relative permittivity versus external applied magnetic field for 30% PNC is shown in Figure 4.10. Permittivity shows an increment as the strength of the externally applied magnetic field is increased, which is saturated around 0.2T. At 4 GHz, the obtained value for relative permittivity at saturation is 3.45,

demonstrating a tunability of 21.65% when referenced to its value of 2.83 when no magnetic field is applied.

Figure 4.10 – 3D plot (left) of the complete extracted relative permittivity vs. magnetic field for PDMS-Fe$_3$O$_4$ PNC at 30% w.t. concentration. The 2D plot (right) shows the extracted permittivity only for five magnetic field biasing conditions.

Figure 4.11 – 3D plot (left) of the complete extracted relative permeability vs. magnetic field for PDMS-Fe$_3$O$_4$ PNC at 30% w.t. concentration. The 2D plot (right) shows the extracted permeability only for five magnetic field biasing conditions.

Figure 4.11 presents the relative permeability of the 30% PNC, demonstrating an increase over its plain (pure) PDMS counterpart, due to the presence of magnetic nanoparticles. The maximum relative permeability was achieved at 0.22T at all frequencies. At 4 GHz, the maximum permeability of 1.85

was achieved, demonstrating a tunability of 68% when referenced to the minimum value of 1.1, when a magnetic field of 0.95T is applied. Note that when a magnetic field of strength higher than 0.22T was applied, the permeability was substantially decreased, being close to one at 0.95T.
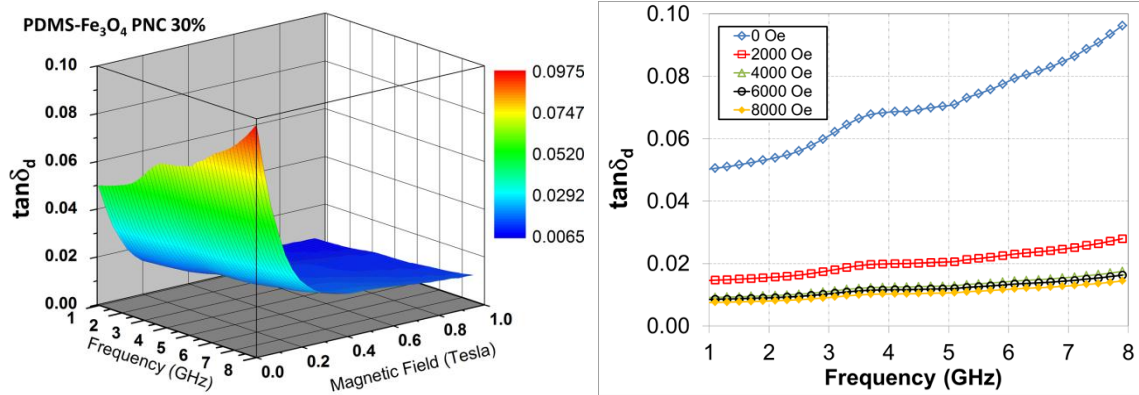
Figure 4.12 – 3D plot (left) of the complete extracted dielectric loss tangent vs. magnetic field for PDMS-Fe$_3$O$_4$ PNC at 30% w.t. concentration. The 2D plot (right) shows the extracted dielectric loss tangent only for five magnetic field biasing conditions.
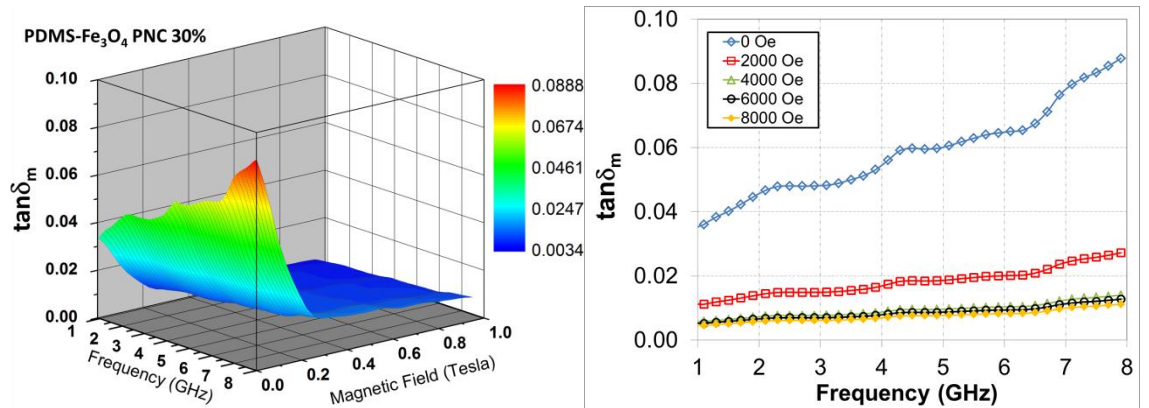
Figure 4.13 – 3D plot (left) of the complete extracted magnetic loss tangent vs. magnetic field for PDMS-Fe$_3$O$_4$ PNC at 30% w.t. concentration. The 2D plot (right) shows the extracted magnetic loss tangent only for five magnetic field biasing conditions.

As observed in Figures 4.12 and 4.13, dielectric and magnetic loss tangents decrease while the strength of the applied magnetic field is increased.

Both losses are considerable diminished by more than a factor of 7 when a magnetic field above 0.25T was applied. However, if higher magnetic fields are applied, the magnitude of the permeability will decrease considerably and permittivity will remain at its maximum value, hence the material encompasses over dominant dielectric effects, which are not desirable for the implementation of bandwidth-enhanced antennas.

4.3.3 Electric Properties of PDMS-Fe$_3$O$_4$ PNC at 50% w.t. Concentration with External DC Magnetic Biasing Field Applied

Relative permittivity versus external applied magnetic field for 50% PNC is shown in Figure 4.14. As in the previous sample, permittivity shows an increment as the strength of the externally applied magnetic field increases. Saturation of the permittivity is achieved at 0.2T. At 4 GHz, the obtained value for relative permittivity at saturation is 3.29, demonstrating a tunability of 21.9% referenced to its value of 2.7 when no magnetic field is applied.
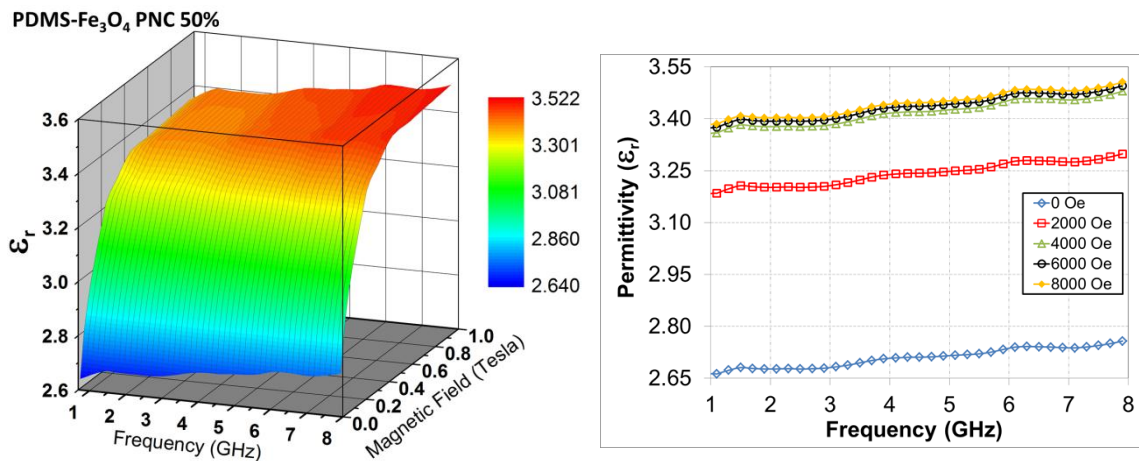
Figure 4.14 – 3D plot (left) of the complete extracted relative permittivity vs. magnetic field for PDMS-Fe$_3$O$_4$ PNC at 50% w.t. concentration. The 2D plot (right) shows the extracted permittivity only for five magnetic field biasing conditions.
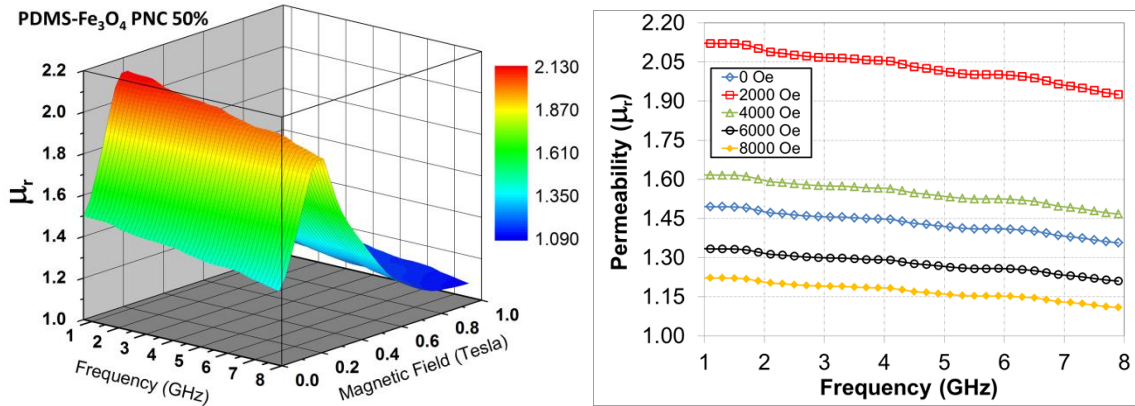
Figure 4.15 – 3D plot (left) of the complete extracted relative permeability vs. magnetic field for PDMS-Fe$_3$O$_4$ PNC at 50% w.t. concentration. The 2D plot (right) shows the extracted permeability only for five magnetic field biasing conditions.

Figure 4.15 presents the relative permeability of the 50 % PNC. As in the 30% PNC sample, the maximum relative permeability was achieved at 0.22T for all frequencies. At 4 GHz, the maximum permeability of 2.06 is achieved, demonstrating a tunability of 76% referenced to the minimum value of 1.17 when a magnetic field of 0.95T is applied. Also here for 50% PNC, the application of magnetic field strengths higher than 0.22T causes substantial decreasing of the relative permeability.
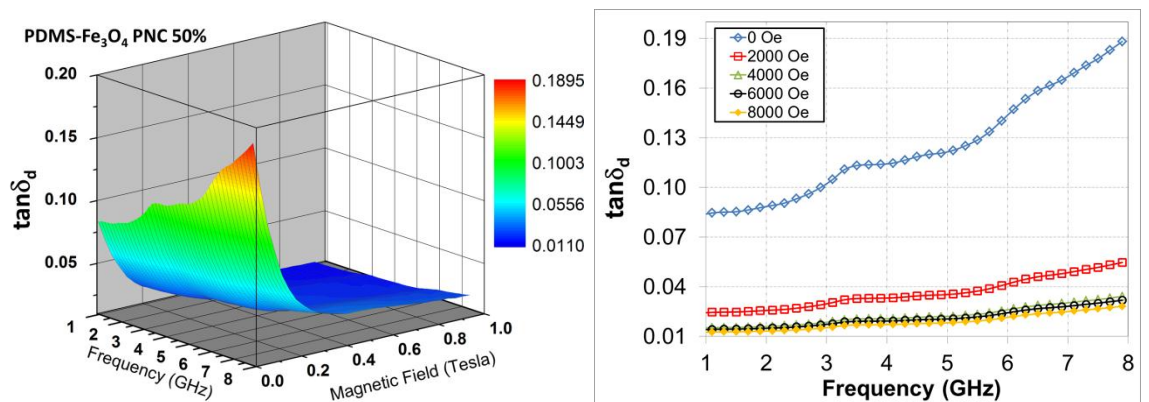
Figure 4.16 – 3D plot (left) of the complete extracted dielectric loss tangent vs. magnetic field for PDMS-Fe$_3$O$_4$ PNC at 50% w.t. concentration. The 2D plot (right) shows the extracted dielectric loss tangent only for five magnetic field biasing conditions.
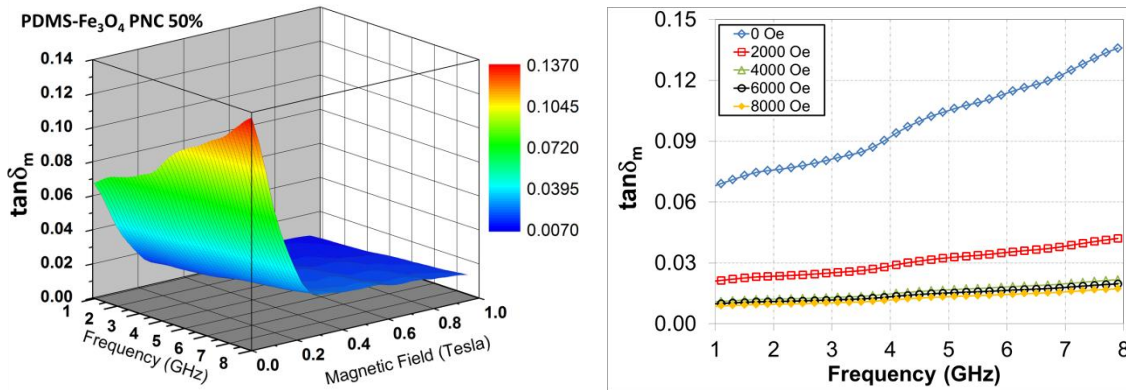
Figure 4.17 – 3D plot (left) of the complete extracted magnetic loss tangent vs. magnetic field for PDMS-Fe$_3$O$_4$ PNC at 50% w.t. concentration. The 2D plot (right) shows the extracted magnetic loss tangent only for five magnetic field biasing conditions.

Figures 4.16 and 4.17 present dielectric and magnetic loss tangents, respectively. As expected, the same trend observed in the 30%PNC. is presented for the 50% PNC. Dielectric and magnetic losses were decreased more than 7 times when magnetic field strengths above 0.25T were applied.

4.3.4 Electric Properties of PDMS-Fe$_3$O$_4$ PNC at 80% w.t. Concentration with External DC Magnetic Biasing Field Applied

Relative permittivity versus external applied magnetic field for 80% PNC is shown in Figure 4.18. As in the 30% and 50% PNCs, permittivity shows an increment as the strength of the externally applied magnetic field increases, experimenting saturation at a field of 0.2T. At 4 GHz, the obtained value for relative permittivity at saturation is 2.79, demonstrating a tunability of 21.3% referenced to its value of 2.3 when no magnetic field is applied.
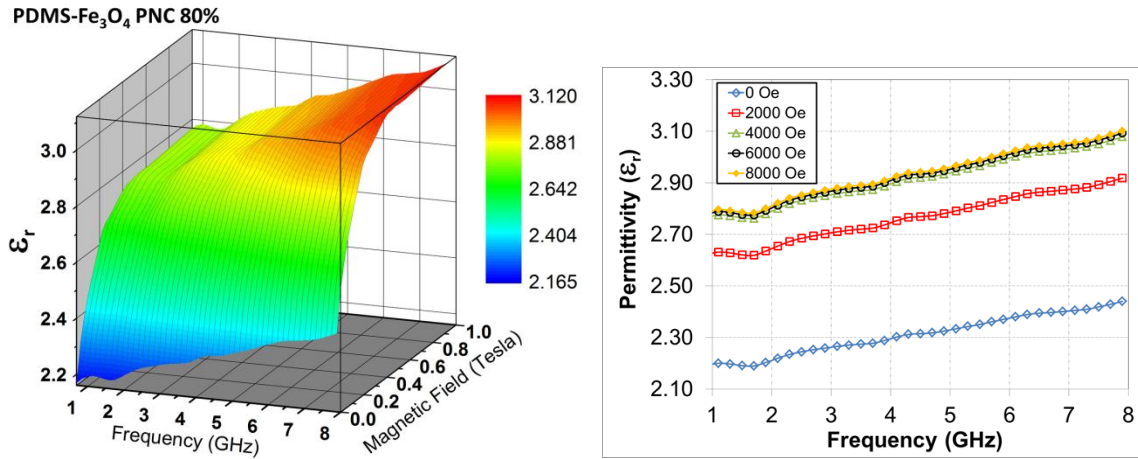
Figure 4.18 – 3D plot (left) of the complete extracted relative permittivity vs. magnetic field for PDMS-Fe₃O₄ PNC at 80% w.t. concentration. The 2D plot (right) shows the extracted permittivity only for five magnetic field biasing conditions.
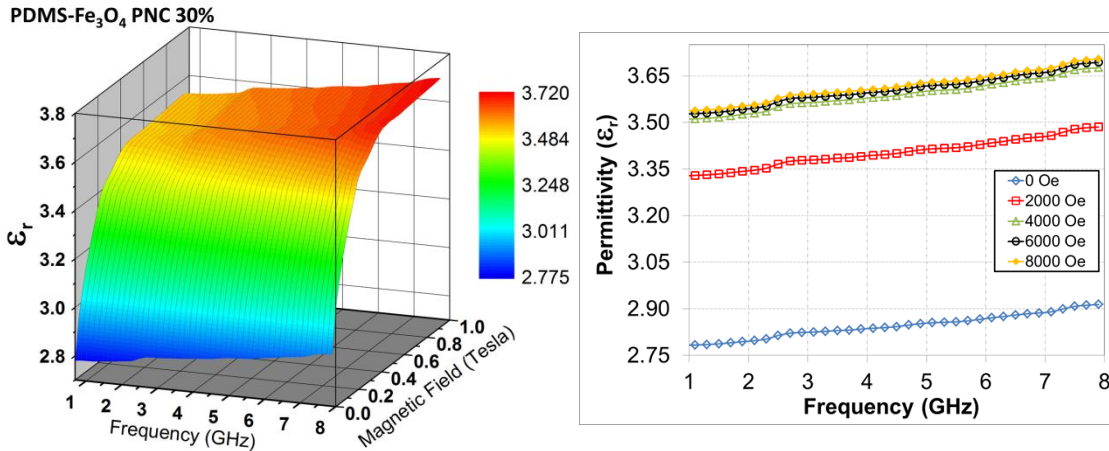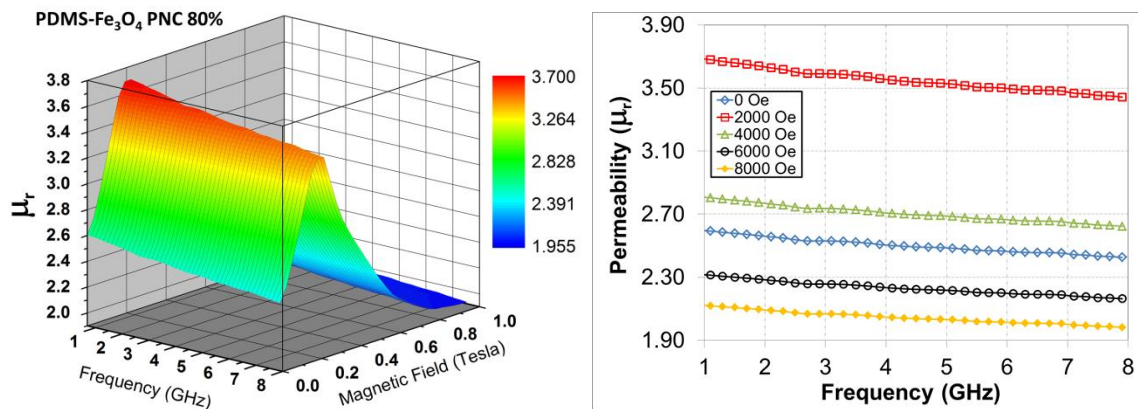

Figure 4.19 – 3D plot (left) of the complete extracted relative permeability vs. magnetic field for PDMS-Fe₃O₄ PNC at 80% w.t. concentration. The 2D plot (right) shows the extracted permeability only for five magnetic field biasing conditions.

Figure 4.19 presents the relative permeability of the 80 % PNC. As in the 30% and 50% PNCs samples, the maximum relative permeability was achieved at 0.22T at all the frequencies. At 4 GHz, the maximum permeability of 3.55 is achieved, demonstrating a tunability of 82% referenced to the minimum value of 1.95 when a magnetic field of 0.95T is applied. As seen in Figure 4.19, the application of magnetic field strengths beyond 0.22T causes a decrease in the

67

relative permeability, but for the 80% PNC case still keeps a significant magnitude.
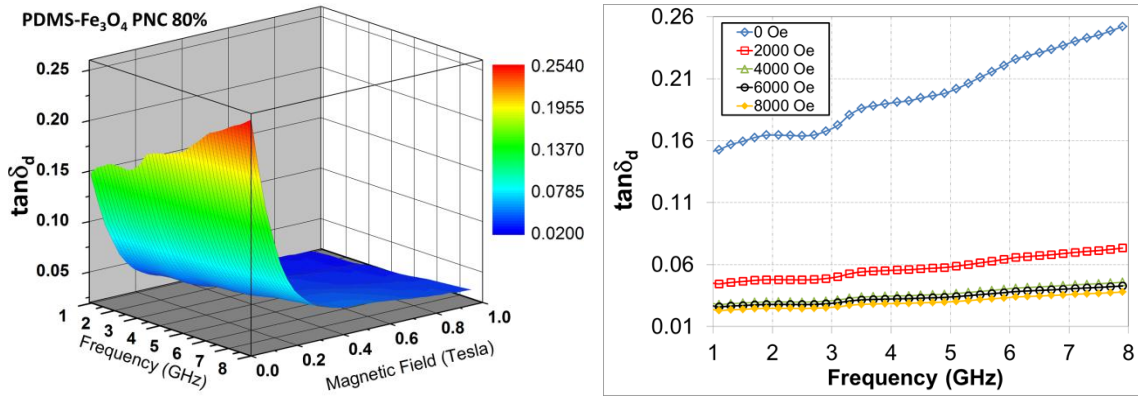
Figure 4.20 – 3D plot (left) of the complete extracted dielectric loss tangent vs. magnetic field for PDMS-Fe$_3$O$_4$ PNC at 80% w.t. concentration. The 2D plot (right) shows the extracted dielectric loss tangent only for five magnetic field biasing conditions.
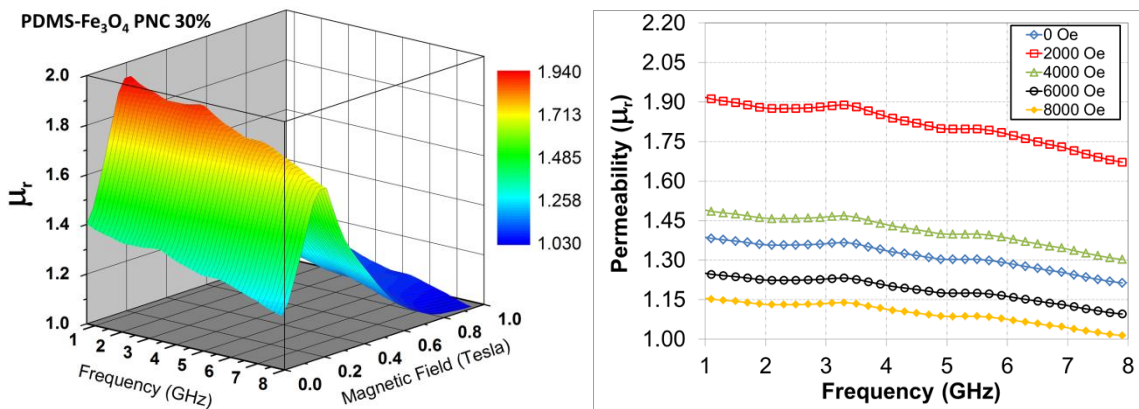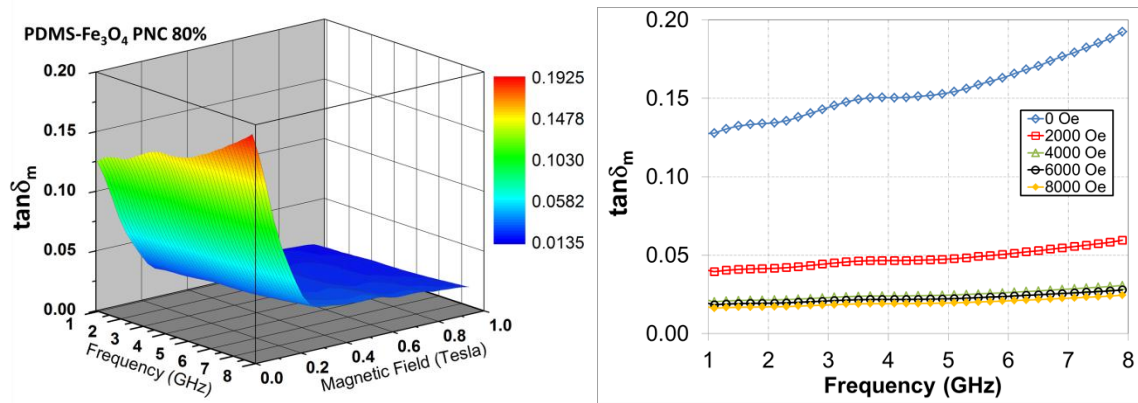

Figure 4.21 – 3D plot (left) of the complete extracted magnetic loss tangent vs. magnetic field for PDMS-Fe$_3$O$_4$ PNC at 80% w.t. concentration. The 2D plot (right) shows the extracted magnetic loss tangent only for five magnetic field biasing conditions.

Figures 4.20 and 4.21 present dielectric and magnetic loss tangents, respectively. As expected, the same trend observed in the 30% and 50% PNCs is presented for the 80% PNC. Dielectric and magnetic losses were decreased

more than 7 times when magnetic field strengths above 0.25T were applied, and more than 10 times when the maximum field of 0.95T is applied to the sample.

4.4 Magnetic Field Strength Consideration for Optimal Operation of Antennas

Several conditions are important to achieve optimal operational conditions for antennas using magneto-dielectrics materials. For the Fe_3O_4 PNC case, tunability of its electrical properties by the application of external biasing field, allows for the tuning of convenient values of permittivity and permeability, thus ensuring the enhancement of characteristics such as antenna miniaturization, bandwidth and radiation properties.

For this purpose, the relative permittivity, permeability and the product between the magnitudes of these two relative properties, for the 80% PNC at 4GHz, have been plotted in Figure 4.22.

The best miniaturization is found when the product of the relative permittivity and permeability (i.e., $\varepsilon_r \times \mu_r$) is at its maximum magnitude, which is obtained when a magnetic field of ~ 0.2T is applied to the PNCs, as observed in Figure 4.22. Coincidentally, the best bandwidth, which takes place when the permeability is at his maximum value, occurs when the same biasing magnetic field is applied to the PNCs. Moreover, the best wave impedance matching with the surroundings is found at the so-called magneto-dielectric condition (i.e., $\varepsilon_r = \mu_r$), which occurs when a magnetic field of ~ 0.37T is applied to the PNCs. All these conditions, defined the best operational area, which is delimited in the plot by the dotted lines. This area corresponds to the application of a magnetic field with a magnitude of 0.2T to 0.37T. This condition occurs simultaneously, at the

69

same values of externally applied magnetic field for all the concentrations of PNCs (30%, 50% and 80% w.t.).
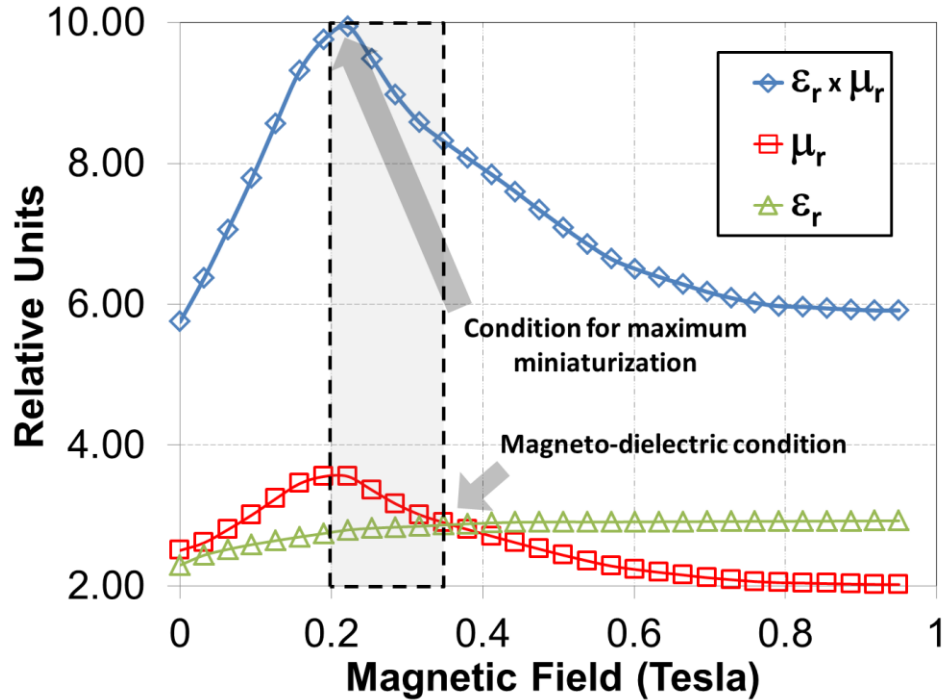
Figure 4.22 – Optimal conditions for miniaturization and impedance matching of the antenna with the surroundings (magneto-dielectric condition).

In addition, when a biasing magnetic field higher than 0.2T is applied to the PNCs, the dielectric and magnetic losses are substantially reduced for all of them, as can be observed in the section 4.3. With a magnetic field in the range of 0.2 to 0.4T, dielectric and magnetic loss tangents below 0.02 are ensured for all the measured frequency range. As a positive fact, the magnitudes of the loss properties are below to what has been reported for bulk magneto-dielectric materials, and close to commercially available substrates such as the case of the Flame Retardant 4 (i.e., FR-4).

4.5 Evaluation of the Tunability of Magneto-Dielectric Polymer Nanocomposites Using Microstrip Linear Resonators (MLR)

A microstrip linear resonator (MLR) was designed using the multilayer structure illustrated in Figures 4.2 and 4.4. The resonance frequency of the resonator depends on the effective material properties of the substrate given by:

$$f_r = \frac{v_p}{\lambda_g} = \frac{c}{\lambda_g \sqrt{\mu_{eff} \cdot \varepsilon_{eff}}} \tag{4.26}$$

where

$$\lambda_g = \frac{2L}{n} \tag{4.26}$$

L is the length of the inner conductor, which resides on the embedded cavity filled with nanocomposites of the same length, and n represents the n_{th} frequency harmonic.

Figure 4.23 presents the measured transmission characteristic S_{21} of the resonator versus applied DC magnetic field. As the strength of the magnetic field is increased, the variation in the resonance frequency, insertion loss and quality factor (Q) are measured. Variations in the resonance frequency are attributed to the variations in the permeability and permittivity of polymer nanocomposites. Concurrently, the insertion loss decreases and the loaded Q increases, both of which can be explained by the variation in the effective losses [14].

The influence of the DC magnetic field on the resonance frequency and of the MLR is shown in Figure 4.24. A deviation of 57 MHz in the resonance frequency was observed (from 2.537 to 2.480 GHz). Additionally, the maximum loaded Q factor of 67 is demonstrated under an external field of 4kOe [14].
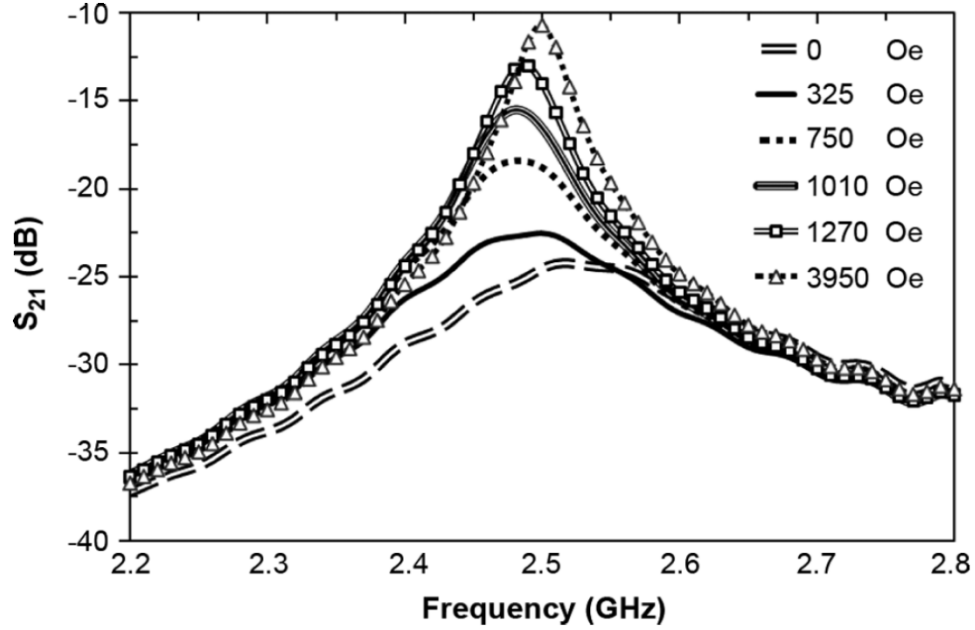
Figure 4.23 – Measured transmission characteristics (S_{21}) of the MLR with embedded polymer nanocomposites. The loaded Q factor, transmitted power, and resonance frequency are dependent upon the strength of the applied magnetic biasing field. From Morales *et al.* [14].
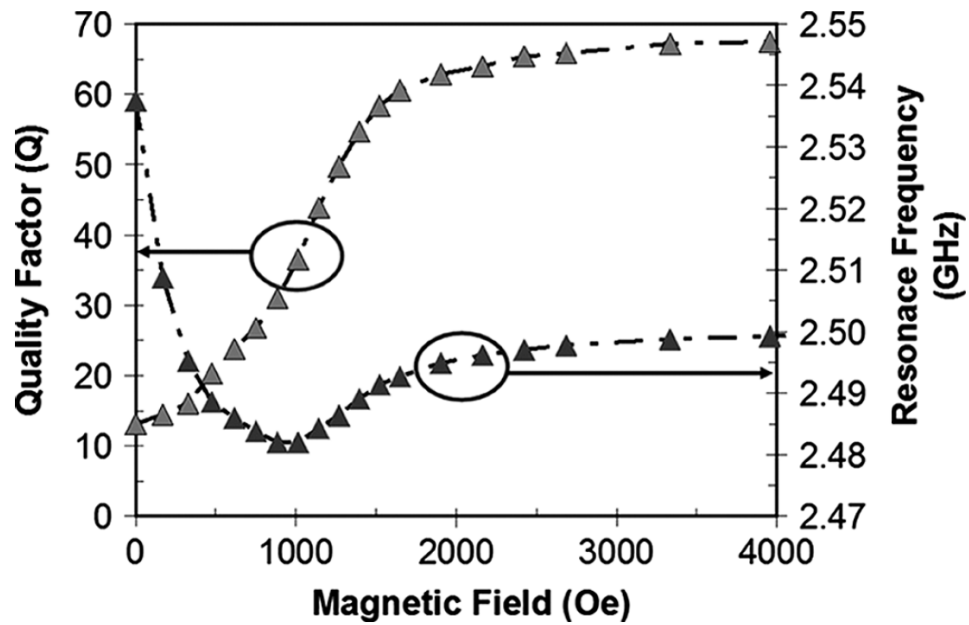
Figure 4.24 – Measured Q-factor and resonant frequency versus DC magnetic field strength. From Morales *et al.* [14].

Chapter 5

Design and Implementation of Multilayer Patch Antennas Using Dielectric and

Magneto-Dielectric Nanocomposite Substrates

5.1 Introduction

In this chapter the fabrication process for multilayer flexible PDMS-based antennas is presented, followed by description of integration of a magneto-dielectric nanocomposite substrate. Subsequently, antenna performance is fully characterized and the results are analyzed based on classical antenna theory.

Four different multilayer microstrip patch antennas have been designed and fabricated to explore the polymer nanocomposite (PNC) material and its implementation as a new class of RF/microwave laminates. The first design consists of a pure Polydimethylsiloxane (PDMS) substrate sandwiched between two Rogers ULTRALAM® 3850 flexible laminates that contain the copper metallization layers. The other three designs are constructed on a PDMS substrate with a cavity completely filled with Fe_3O_4-PDMS PNC at Fe_3O_4 loading concentration of 30%, 50% and 80%, respectively, all of them given by weight percentage (wt%).

5.2 Design of Multilayer Microstrip Antennas

At first sight, it is very difficult to conceive that given the geometrical configuration of a microstrip patch antenna, it can operate with minimal acceptable performance. This reasoning is supported by observing that the

radiation is produced by the horizontal electric surface current in a metallization layer located at a short distance above a ground plane. Based on the predictions using image theory, such current does not radiate well. However, the patch and the ground plane together form a resonant cavity which is filled with the substrate material [36]. Given this characteristic, the microstrip patch antenna has been selected here because of its high sensitivity to the substrate material properties, derived from the high interaction within the patch and its ground plane throughout the substrate.

5.2.1 First Design: Multilayer Patch Antenna on Plain PDMS Substrate

A multilayer patch antenna on pure PDMS substrate has been designed to operate with a resonant frequency of 4GHz. This frequency has been selected in order to achieve a dual benefit: a convenient size to optimize the material resources and to facilitate antenna performance measurements.

In order to retain an attractive radiation efficiency ($\geq$90%), the thickness of the substrates has been selected to be around $0.02\lambda_0$ (1/50 of the signal wavelength in free space), as selected in [36] for a Teflon substrate which exhibits similar electrical characteristics. A thicker substrate selection would lead to improved radiation efficiency, but requires more substrate material. At 4GHz (λ_0~74.95mm) a substrate with a thickness of 62mils (1.5748mm) is selected, which is equivalent to $0.021\lambda_0$.

Figure 5.1 depicts the 3D schematic diagram of the multilayer microstrip patch antenna assembly and identifies the constituent patterned layers and their respective thicknesses. As shown, a 60mil (1.524mm) thick PDMS layer is

74

sandwiched between two Rogers ULTRALAM® 3850 LCP laminates featuring the antenna patch and the ground plane, respectively. Each Rogers LCP laminate has a thickness of 1mil (25.4μm). The bottom side of antenna (i.e., underneath its ground plane) is totally covered by a 100mil (2.54mm) thick PDMS layer, while the top of the antenna is partially covered with a molded 100mil thick PDMS layer, with an opening over the antenna patch and microstrip line. PDMS is not desired on the top of the patch and microstrip as it will reduce the antenna efficiency. Encapsulation with PDMS helps keep the flexibility of the entire antenna assembly, without wrinkling the Rogers LCP laminates and copper clads, whenever the antenna is bent or flexed. Over the upper LCP laminate, seven small anchoring copper features have been located near the edges, in order to prevent the LCP substrate from sliding sideways when the antenna assembly is bent, and improve the bonding between PDMS layer and the flexible Rogers LCP laminate. It has been demonstrated by 3D electromagnetic simulations, that those features do not play any role in the antenna performance.
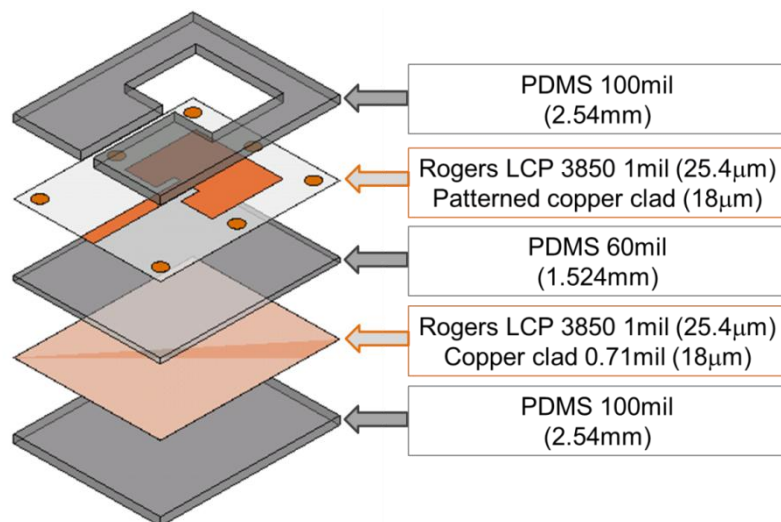
Figure 5.1 – 3D schematic diagram of the multilayer microstrip patch antenna identifying all its layers and their thicknesses.

Figure 5.2 shows the assembled patch antenna in both perspective view and top view, while identifying the key features and dimension parameters. The antenna is designed using the PDMS dielectric and loss properties extracted and shown in the previous chapter. The dimensions of the antenna have been optimized using HFSS v11.1 where the vectors with the extracted permittivity (ε_r) and dielectric loss tangent ($tan\delta_d$) were used. At the target resonance frequency of 4GHS, the extracted values of the electrical properties for PDMS were ε_r =2.7 and $tan\delta_d$=0.019. For the Rogers ULTRALAM® 3850 LCP laminates, ε_r =2.9 and $tan\delta_d$=0.0025 were used, as provided by Rogers Corp in [37].
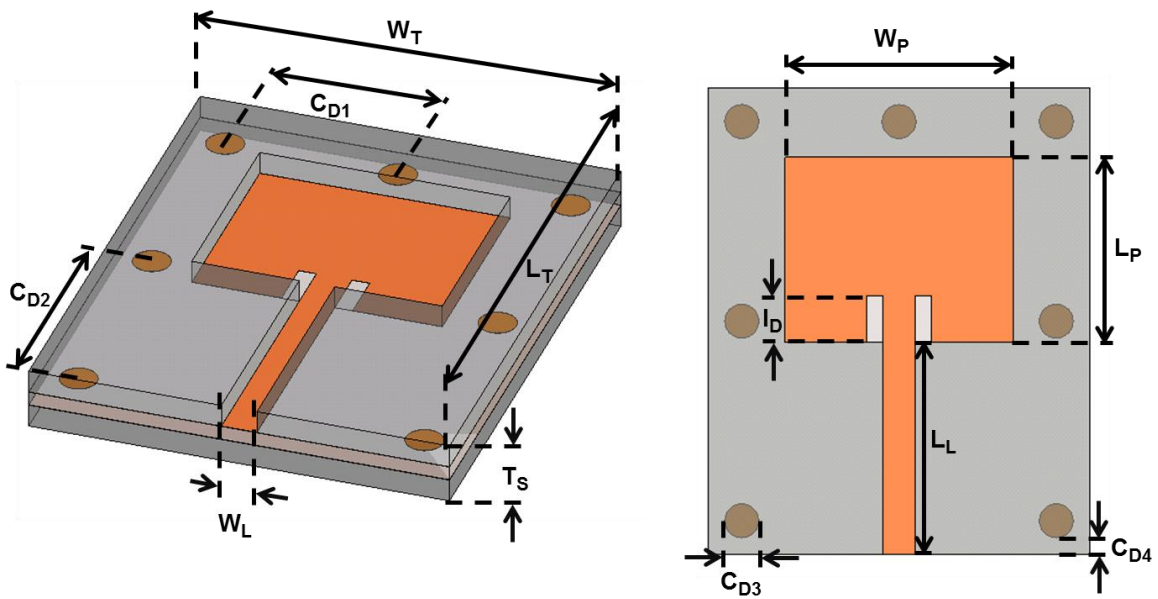
Figure 5.2 – A perspective-view (left) and top-view (right) schematic of the assembled multilayer antenna identifying key features and dimension parameters.

In this design, the total width, length and thickness dimensions of the patch antenna assembly were set to be W_T=1.77in(45mm), L_T=2.16in(55mm) and T_S=262mil(6.65mm), respectively. Usually the width of the patch is assigned in the range of 1.25 to 1.75 times the length. In order to maintain the size to be as

small as possible, the minimum patch dimensions were chosen using the parametric relationship $W_P = 1.25 L_P$, resulting in $W_P = 1.07 in (27.25mm)$, $L_P = 858.3 mil (21.8mm)$ and $I_D = 216.5 mil (5.5mm)$, where the inset length (I_D) is determined for optimum impedance matching. The dimensions of the microstrip feed line are $W_L = 149.6 mil (3.8mm)$ and $L_L = 984.3 mil (25mm)$, with a copper clad layer thickness of $18 \mu m$. Finally, the dimensions related to the circular anchors are specified as $C_{D1} = 1.77 in (45mm)$, $C_{D2} = 925.2 mil (23.5mm)$, $C_{D3} = 157.5 mil (4mm)$ and $C_{D4} = 78.7 mil (2mm)$.

The return loss for the PDMS multilayer patch antenna is obtained by 3D electromagnetic simulations using HFSS v11.1 and shown in Figure 5.3. The simulations results revealed an antenna bandwidth of 140MHz (3.5%) from 3.93GHz to 4.07GHz.
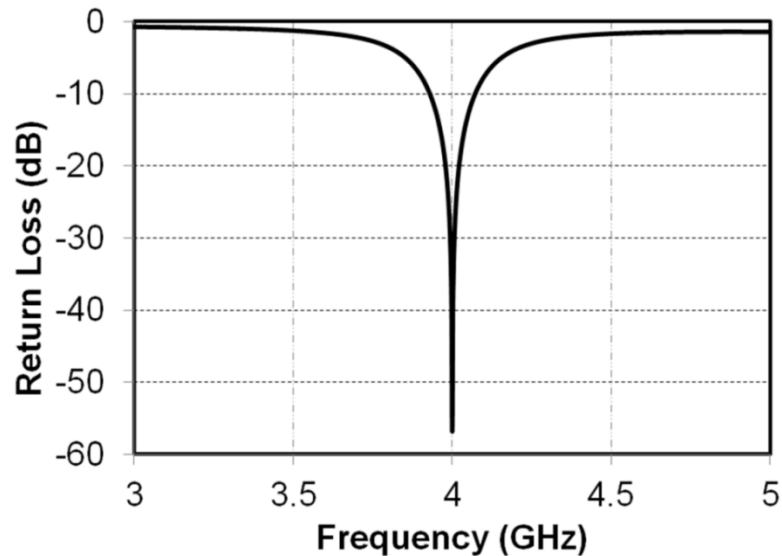
Figure 5.3 – Simulated return loss for a Rogers 3850/PDMS/Rogers 3850 multilayer patch antenna. The resonance frequency has been set to 4GHz using extracted data from PDMS and tuning the physical dimensions of the antenna.

5.2.2 Second Design: Multilayer Patch Antenna on PDMS-Fe$_3$O$_4$ PNC Substrate

A modified version of the multilayer patch antenna with PDMS-Fe$_3$O$_4$ PNC substrate is presented herein. For ease of comparison, this antenna has also been set to work with a resonance frequency of 4GHz. Figure 5.4 presents the 3D schematic diagram of the multilayer microstrip patch antenna assembly while identifying all its layers and their respective thicknesses. As seen, this design differs from the previous in the incorporation of the PDMS-Fe$_3$O$_4$ PNC underneath the patch and between the two Rogers ULTRALAM® 3850 LCP laminates. Also, dimensions of the patch have been adjusted from those in the previous design to retain the same resonance frequency. Figure 5.5 shows the physical dimensions of the new antenna design. Now, W_P=777.56mil(19.75mm), L_P=622.05mil(15.8mm) and the insets are no longer needed (I_D=0). In addition, the dimensions of the PDMS-Fe$_3$O$_4$ PNC filled cavity are W_N=866.14mil(22mm), L_N=669.29mil(17mm) and with the same thickness of the PDMS substrate 60mil(1.524mm). The rest of the physical parameters are kept the same as in the previous design. As noted, since the resonance frequency of the antenna has been kept the same, then size comparison between the antennas could be accomplished based on the areas of the antenna patch in different designs.
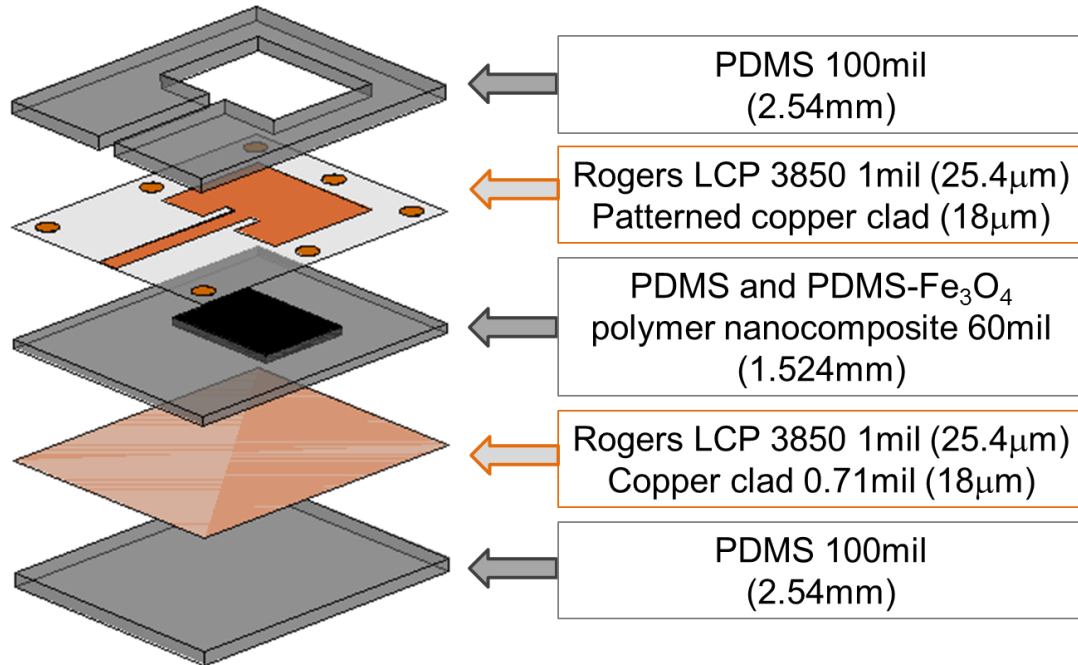
Figure 5.4 – 3D schematic of the multilayer microstrip patch antenna with a cavity embedded completely filled with PDMS-Fe_3O_4 PNC. The composition and thickness for each layer is also clearly specified.
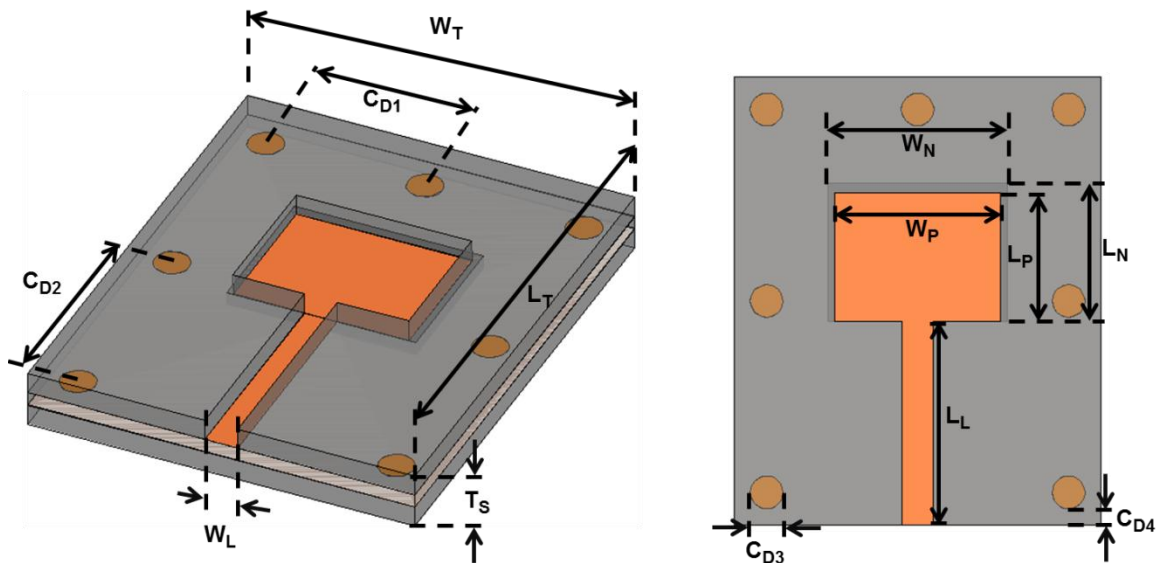
Figure 5.5 – A perspective-view (left) and top-view (right) schematic of the assembled multilayer antenna, which includes a PDMS-Fe_3O_4 PNC filled cavity underneath the antenna patch. Both figures identify key features and dimension parameters. Note that W_N and L_N describe the dimensions of the embedded PNC layer.
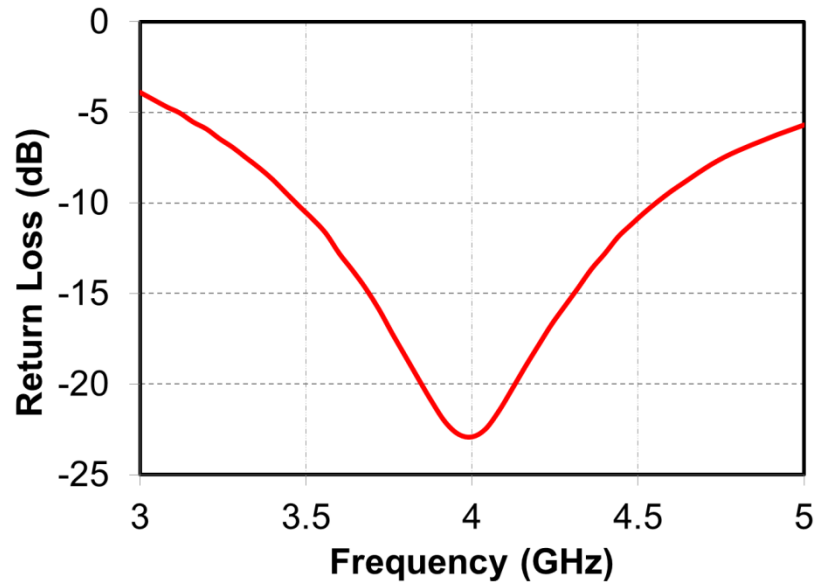
Figure 5.6 – Simulated return loss for the multilayer patch antenna with embedded PDMS-Fe_3O_4 nanocomposite and 80% w.t. loading. The resonance frequency has been set to 4GHz using extracted data from PDMS-Fe_3O_4 PNC at this concentration, and tuning the physical dimensions of the antenna.

The simulated return loss for the PDMS multilayer patch antenna with embedded 80% PDMS-Fe_3O_4 nanocomposites is shown in Figure 5.6. The multilayer antenna exhibited a bandwidth of 1.081GHz (27%) from 3.479GHz to 4.560GHz.

5.3 Fabrication of Multilayer Microstrip Patch Antennas

To assemble the multilayer antenna, the two Roger LCP flexible laminates and the PDMS layers have been patterned using standard photolithography processes and deposited in-house molding techniques, respectively. For the sake of brevity and better organization, the entire fabrication process has been divided into two different subsections. The first one describes the step-by-step processes for fabrication of a multilayer patch antenna on a PDMS substrate. The second one describes the fabrication of the multilayer antenna on a PDMS

substrate with an embedded cavity filled with PDMS-Fe_3O_4 PNC underneath the antenna patch.

5.3.1 Fabrication of Multilayer Patch Antennas on PDMS Substrate

One mil (25.4μm) thick flexible Rogers ULTRALAM® 3850 LCP laminates are used to form the patterned metallization layers (i.e., patch, microstrip feed line and ground plane) of the multilayer patch antenna. Figure 5.7 shows the process flow followed for definition of the ground plane used in the multilayer microstrip antenna assembly. Initially, one of the copper clads is protected by a layer of negative dry film photoresist (416DFR from MG Chemicals). This photoresist is then exposed to UV-light for 2 minutes using a Kinsten KVB30D-AU UV exposure box. Subsequently, the substrate is submerged in ferric chloride solution in a Kinsten ET20 etching tank at 60$°$C with bubble agitation for 8 minutes, followed by rinsing in DI water. The copper clad over the unprotected side is completely removed, while the side protected by the dry film remains unaltered. Finally, the remaining photoresist is stripped away by submerging the substrate in acetone for 3 minutes followed by DI water rinsing until any other chemical residue is removed. As the process described herein involves the use of photosensitive dry film, the entire process step is carried out in a cleanroom facility under "yellow light".
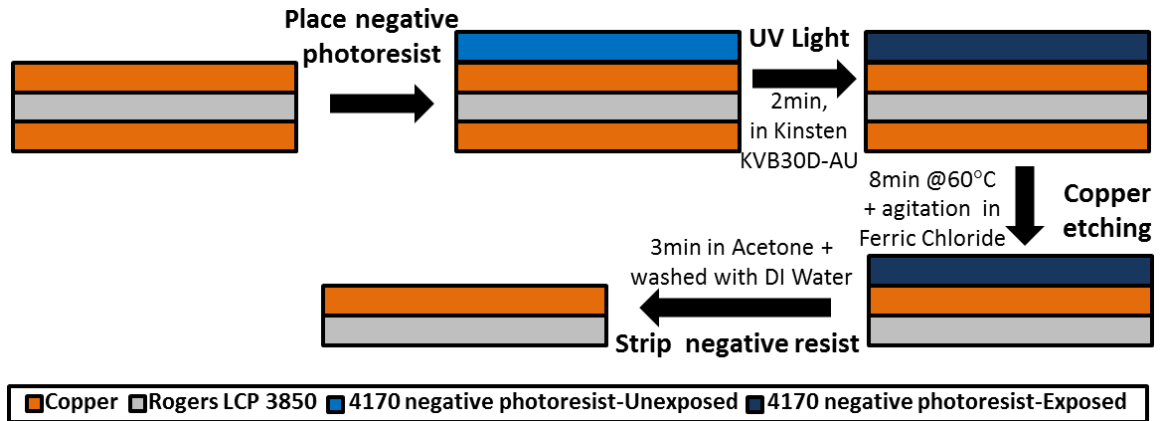
Figure 5.7 – Cross-sectional view diagram of the fabrication process flow for patterning the ground plane on one side of a Rogers LCP 3850 laminate.

As seen in Figure 5.8, for patterning the antenna patch and the microstrip feed line, a similar procedure was followed with addition of one more step. One side of the Rogers LCP 3850 laminate was covered with the dry film photoresist, and exposed to UV-light for 2 minutes through a photo mask in an acetate transparency. The transparency photo-mask for definition of the antenna patch and microstrip feed line was designed using Autodesk AutoCAD, and printed out by an Epson stylish 3800 inkjet printer onto HP premium inkjet transparency film sheets (C3834A). After exposure under UV light for 2 minutes, the negative dry film photoresist was developed for 5 minutes in Negative Photoresist Developer (4170 from MG Chemicals) dissolved in water in a 1:10 ratio. After the development step, the portion of the copper clad for the antenna patch and feedline was protected by the negative photoresist, whereas the exposed copper (including the entire copper clad on the back of the substrate) was removed by ferric chloride copper etchant solution. Finally, the photoresist was stripped using

acetone and the substrate was washed using DI water to remove remaining chemicals.
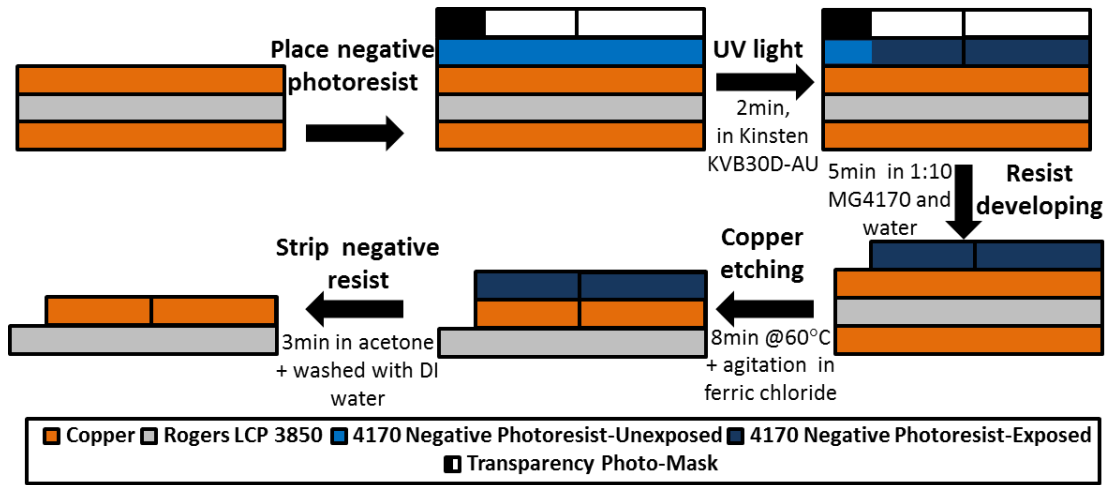
Figure 5.8 – Cross-sectional view diagram of the fabrication process flow for definition of the antenna patch on one side of a Rogers LCP 3850 laminate.

Once the elaboration of the ground plane and antenna patch with its microstrip feed line was concluded, the entire multilayer antenna was eventually assembled by stacking three molded PDMS layers with the two patterned LCP laminates. Figure 5.9 illustrates the step by step process for the assembly of the multilayer patch antenna.

Figure 5.9(a) shows a square-shaped mold with 56.25cm^2 (7.5 cm × 7.5 cm) of area and 2.5cm of height, which is assembled from commercially available glass microscope slides (Fisherbrand® premium plain glass microscope slides 125444). The glass pieces are bonded together using Loctite® glass glue, and the structure is sealed and reinforced by using Loctite® Stik'n Seal® for extreme conditions. This seal will provide excellent bonding and sealing conditions for temperatures up to 120°C. Moreover, the usage of the bonded glass slides

83

system facilitates the casting and de-molding of the PDMS layer as these can be easily detached by bending the structure.

The base resin and curing agents of Sylgard® 184 are mixed in a 10:1 weight ratio. PDMS (Sylgard® 184) has a specific gravity of 1.03 at room temperature. Initially a layer with 100mil (0.254cm) of thickness is deposited. For this purpose, the following basic equations are used:

$$V_S = A_M \cdot T_S \tag{5.1}$$

$$W_{PDMS} = V_S \cdot \rho_{PDMS} \tag{5.2}$$

where V_S and T_S are the volume and desired thickness of the deposited layer respectively, A_M is the area of the mold equivalent to 56.25cm^2, W_{PDMS} is the required PDMS mass to achieve the desired layer thickness and ρ_{PDMS} is the density of PDMS which is 1.03g/cm^3.

Using the pre-designed mold and equations 5.1 and 5.2, a volume V_S of 14.2875cm^3 is required for a desired thickness T_S of 100mil (2.54mm), which results in required PDMS mass W_{PDMS} of 14.7161g.

The mold is placed in an single pan electronic balance (Mettler AE100) and (14.7161+0.48)g of PDMS are poured into the mold. From several experiments, it has been found that an additional PDMS mass of 0.48g is needed to achieve the desired thickness given the amount of residual polymer material adhered to the walls of the mold (meniscus formation).

In a convection vacuum oven (Fisher® 281A), 30inHg of vacuum are applied for 5 minutes to extract the trapped air bubbles in the PDMS. Subsequently the polymer is cured by heating to 90°C for 45 minutes. The mold

is extracted from the oven and cooled down to room temperature, resulting in the structure shown in Figure 5.9(b). From previous experiments, the thickness of the PDMS layer has been measured by using a caliper obtaining a reading of 2.55±0.08mm, which is equivalent to a standard deviation of less than 3.2%.

Thereafter, the ground plane of dimension 55mm × 45mm, patterned on a Rogers ULTRALAM® 3850 LCP laminate, is placed at the center of the mold (Figure 5.9(c)). The LCP laminate and PDMS layer were stuck together spontaneously under vacuum, which also helps avoid bubble formation within their interface.

Subsequently, a 60mil (1.524mm) thick PDMS layer is molded with total amount of PDMS determined by Equations (5.1) and (5.2). (8.83+0.48)g of PDMS are poured into the mold, and placed under 30inHg of vacuum for 5 minutes to remove air trapped bubbles. Finally, the PDMS is cured by heating the sample to 90°C for 45 minutes (Figure 5.9(d)). Once the sample is cured and cooled down to room temperature, the Rogers ULTRALAM® 3850 LCP laminate with patterned antenna patch is positioned at the center of the mold as shown in Figure 5.9(e). The LCP laminate sticks to the surface of the molded PDMS spontaneously. In order to remove the PDMS that will be deposited on top of the antenna, acetate transparency is placed on top of the patch and microstrip line using double-sided adhesive tape, which will be removed after the curing process. 30mmHg of vacuum are applied to remove trapped air bubbles at the interfaces between the two layers. Then the sample is removed from vacuum and (14.7161+0.48)g of PDMS are poured in the mold to form a 100mil(2.54mm)

thick upper layer as shown in Figure 5.9(f). Similarly, vacuum is applied to remove bubbles from the PDMS and the sample is cured at 90°C for 45 minutes.
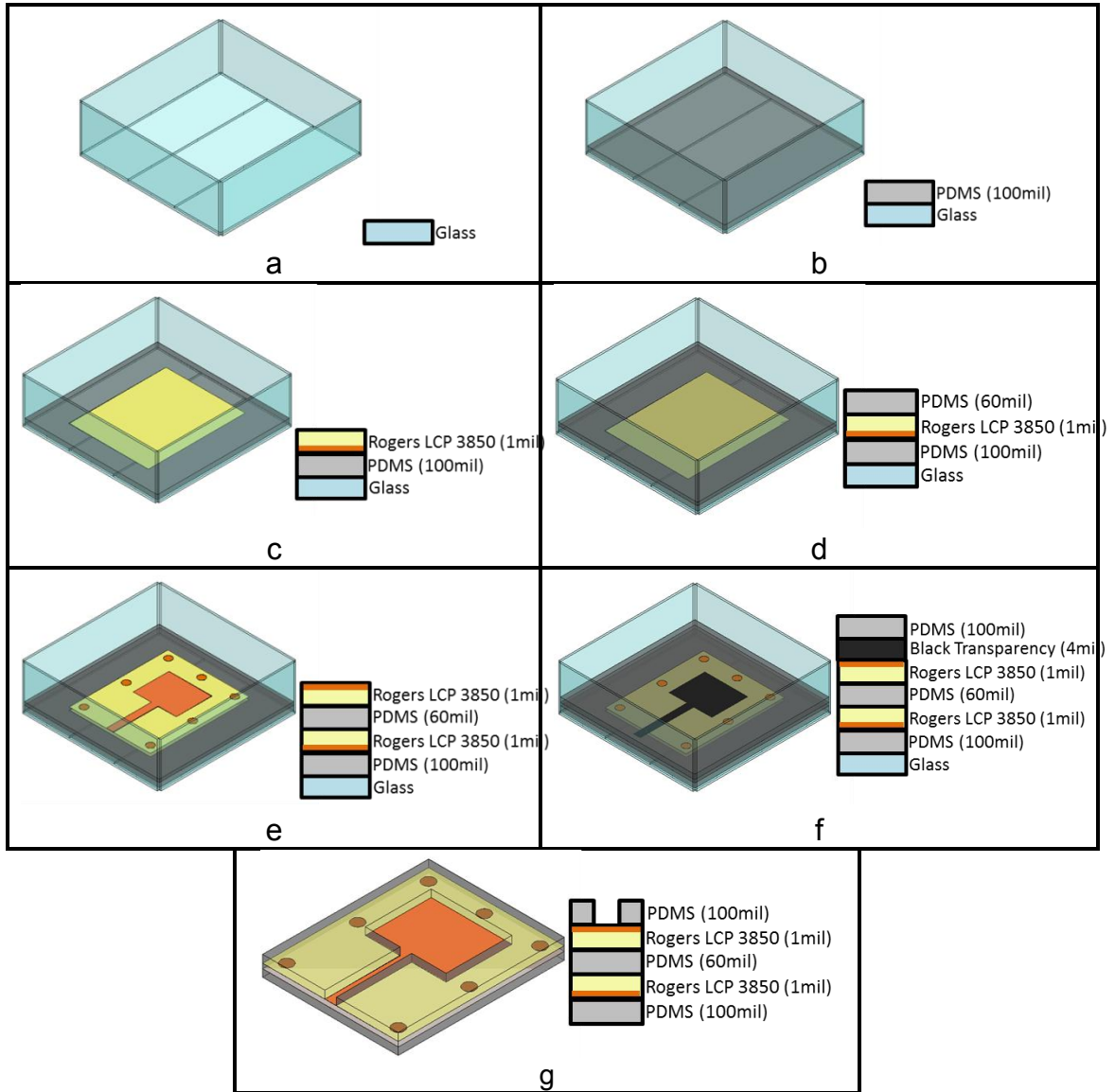
Figure 5.9 – Perspective-view schematic diagram for the step-by-step process flow of the PDMS based multilayer antenna. Process starts with the empty square-shaped mold in (a) and ends with the released antenna in (g). Each processing step is illustrated by both perspective-view and cross-sectional schematics identifying the existing layers at each stage.

Finally, the antenna is released from the mold by eliminating the glass slides. By pulling away the acetate transparency and trimming the edge using a fine exacto blade, the cured PDMS is removed from the top of the antenna patch

leaving it uncovered in the air (Figure 5.9(g)). In addition, a small square portion near the edge of bottom PDMS layer covering the ground plane is removed to accommodate an edge mount SMA connector that is soldered to the microstrip feed line.
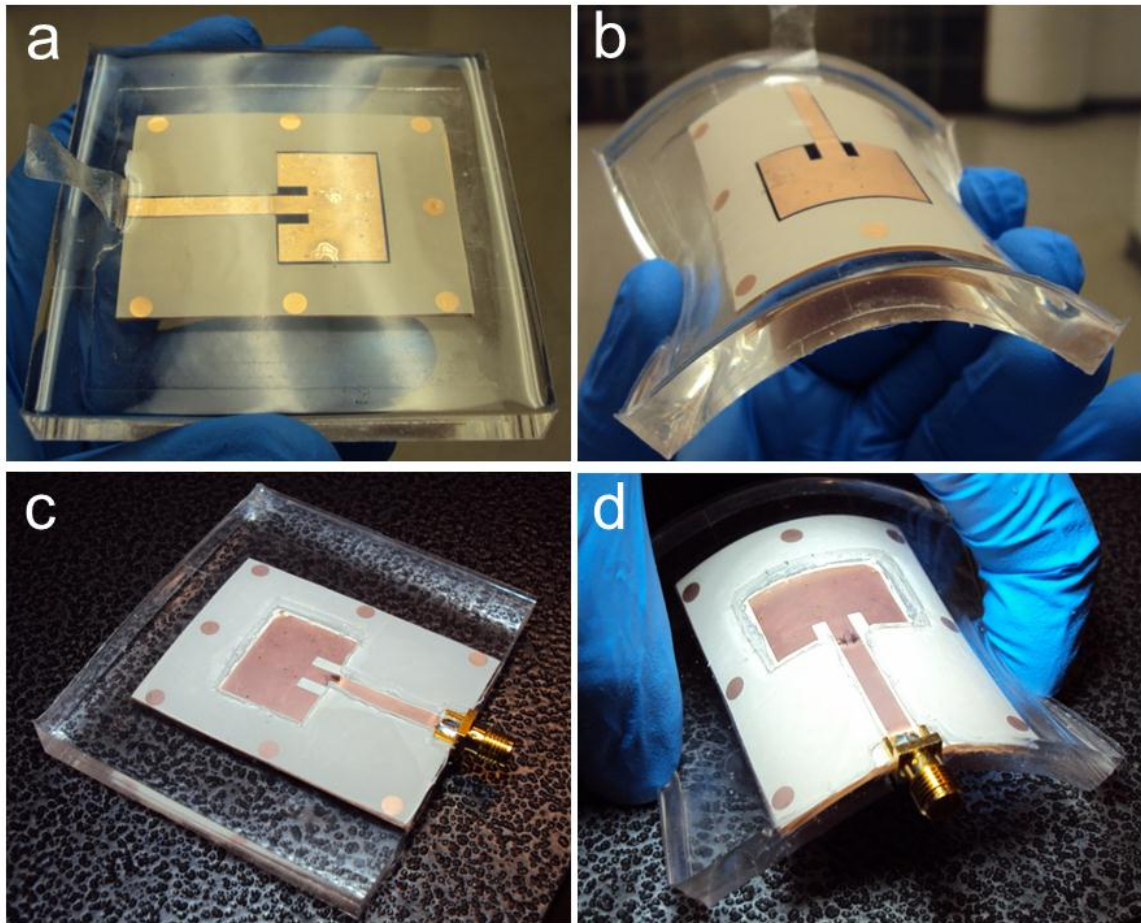
Figure 5.10 – Pictures of the multilayer patch antenna on a molded PDMS substrate using the process flow shown in Figure 5.9.

Figure 5.10 presents four pictures of the multilayer antenna right before and after removal of the PDMS from the top of the patch and feed line. Figure 5.10(a) shows the molded PDMS antenna right after it is released from the glass mold, showing the patch still covered by the embedded sacrificial black transparency. The flexibility of the antenna at this stage is demonstrated in figure

5.10(b), which also verifies no wrinkle formation in the antenna after bending. The final multilayer antenna right after removal of the embedded sacrificial transparency, to fully expose the antenna patch and feed line, is presented in figure 5.10(c). In addition, the antenna feed line and port has been terminated with a coaxial SMA connector. Finally, the completed antenna with SMA connected is bent to demonstrate its flexibility (figure 5.10(d)).

5.3.2 Multilayer Patch Antenna on Hybrid PDMS/Fe$_3$O$_4$-PDMS Substrate

For this design, both metallization layers (ground plane and patch) are constructed on Rogers LCP 3850 flexible laminates following the same process steps as shown in Figure 5.8. As a layer of PDMS-Fe$_3$O$_4$ PNC is incorporated in this design, the fabrication process of the multilayer array is modified to facilitate the integration of the new layer. Figure 5.11 shows the new process used for the construction of the multilayer patch antenna on a hybrid PDMS/Fe$_3$O$_4$-PDMS substrate.

As shown in Figure 5.11(a), the process starts with a custom-built glass mold identical to that used in the previous design. As detailed in the previous section, the multilayer antenna is constructed starting from the bottom side up, inside the mold. The first two layers including the first PDMS layer and the first LCP laminate with patterned ground plane are kept the same as depicted in Figures 5.11(b) and 5.11(c). The third layer (from the bottom up) is a 60mil thick PDMS layer with an embedded cavity filled with PDMS-Fe$_3$O$_4$ PNC, which is molded separately and machined by a LPKF ProtoMat S62 milling machine.
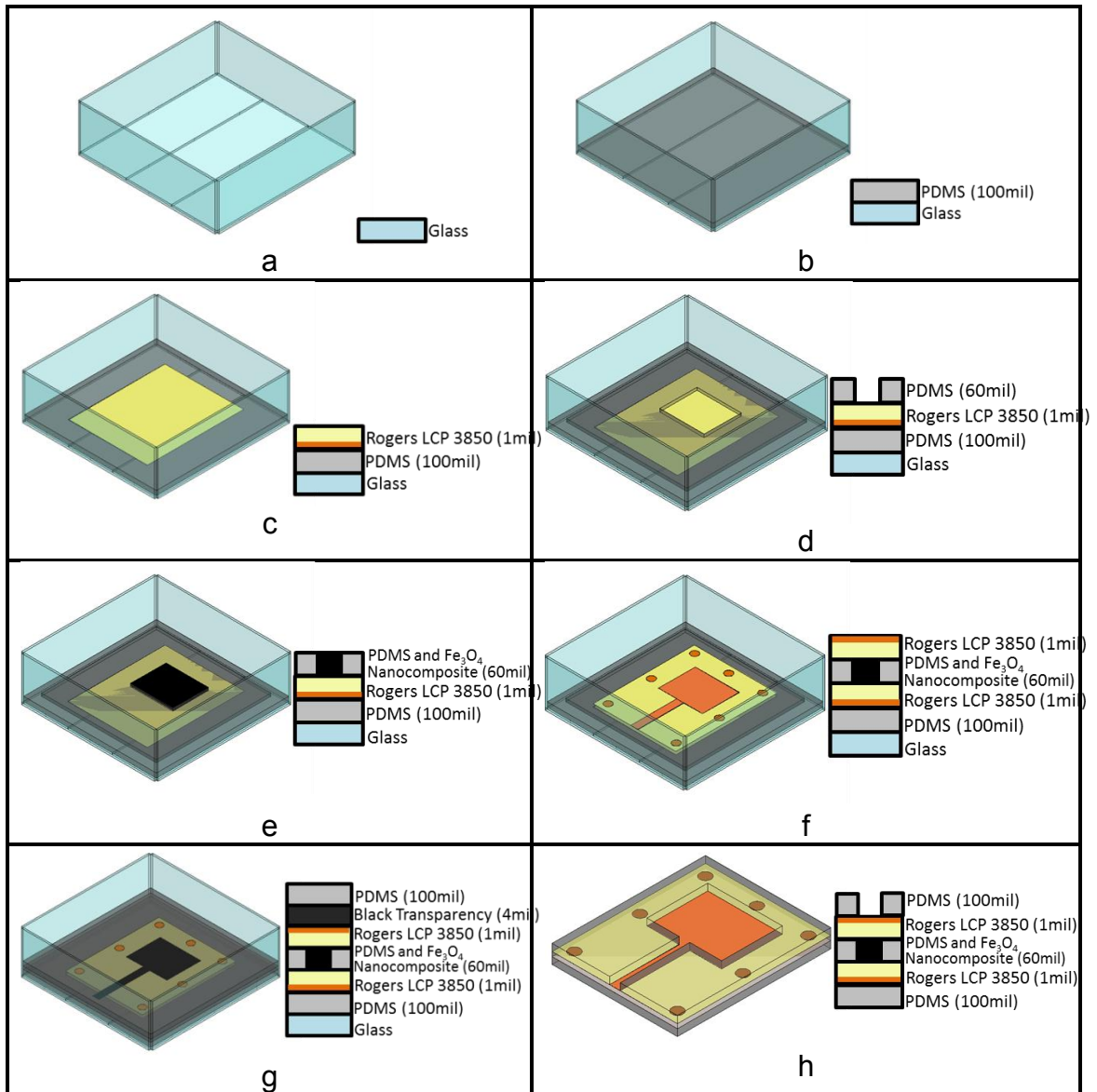
Figure 5.11 – Diagram with the different steps in the construction of the PDMS-Fe$_3$O$_4$ PNC based multilayer antenna. The process starts from the empty glass mold in (a) and ends with the released antenna in (g). Each step plot is complemented (at the right) with and schematic presenting the existing layers at each one of the stages.

Aside from the cavity built at its center, this molded PDMS layer is cut smaller in area and aligned to the center of the mold (see Figure 5.11(d)), which will be bonded to the multilayer stack by molding of the next PDMS layer. PDMS-Fe$_3$O$_4$ PNC, prepared by following the process detailed in section 3.5, is poured

in the cavity followed by evaporation of the solvent and refilling until the cavity is completely filled. After the cavity is filled, the PNC is planarized using a spatula. Figure 5.11(e) shows the structure when the planarization process is completed and the cavity is fully filled with PNC.

As shown in Figures 5.11(f) and 5.11(g), the remaining layers include the flexible LCP laminates with the antenna patch metallization layer, the embedded transparency and the molded PDMS layer (prepared following the aforementioned procedures). Finally, the antenna is released from the custom-built glass mold and cut to the desired dimensions as shown in Figure 5.11(h).
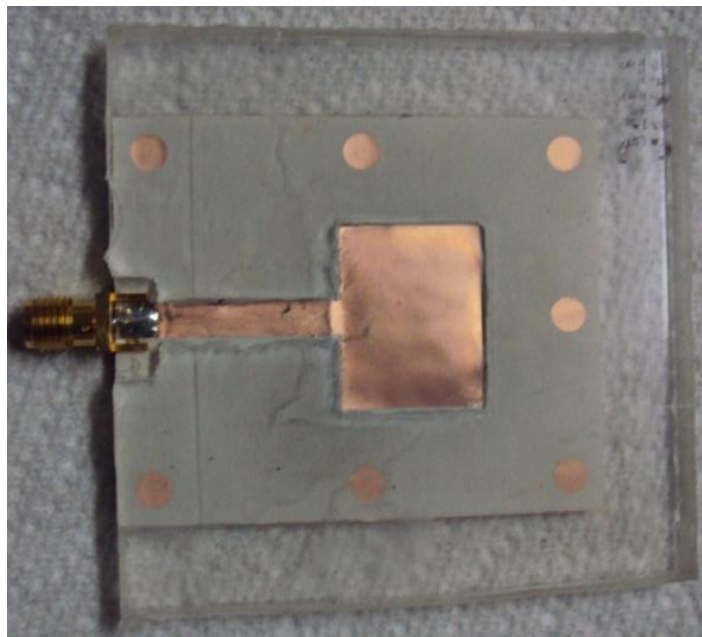
Figure 5.12 – Top-view photo of multilayer patch antenna constructed on PDMS-Fe$_3$O$_4$ PNC substrate following the process flow described in Figure 5.11. The patch and microstrip feed line are exposed to the air (without PDMS overcoat) and terminated with a coaxial SMA connector.

A top-view photo of the finalized patch antenna on PDMS-Fe$_3$O$_4$ PNC multilayer substrate is shown in Figure 5.12. PDMS in the upper layer on the top of the patch and the microstrip feed line has been removed, and the port has

been terminated with a coaxial SMA connector. The embedded cavity filled with PNC is not visible as it is hidden underneath the upper Rogers LCP laminate with the patterned antenna patch.

5.4 Experimental Results

As mentioned before, four different designs with different loading of Fe_3O_4 nanoparticles have been simulated and measured. The return loss and radiation pattern of all the antennas are measured and then compared with the results obtained by simulations using ANSYS™ HFSS® v. 11.1. The PDMS antenna is used as the reference for performance comparison purposes with the other three remaining designs, which include the usage of PDMS-Fe_3O_4 PNCs at different Fe_3O_4 weight concentrations of 80%, 50% and 30%, respectively. For organization purposes, each antenna is analyzed independently and then compared in the final sub-section.

5.4.1 Pure PDMS-Based Antenna (without Fillers)

Simulated and measured return losses for the pure PDMS-based multilayer patch antenna are shown in Figure 5.13. These results show measured and simulated resonance frequencies of 3.931GHz and 4.002GHz, respectively. The difference in the resonance frequencies is only of 71MHz or 1.77%, which confirms that an excellent extraction of the PDMS electrical properties has been implemented. The small frequency offset may be introduced during the simulation (the approximations of the finite element method) and the inclusion of elements such as the SMA feeding connector. For comparison purposes, measured and simulated E-plane and H-plane radiation pattern is

shown in Figures 5.14 and 5.15, respectively. A good agreement is achieved with a main lobe tilted 22° in the simulation and 27° in the measurement. This tilting is originated from the interaction of the patch with the wide 50Ω feeding line.
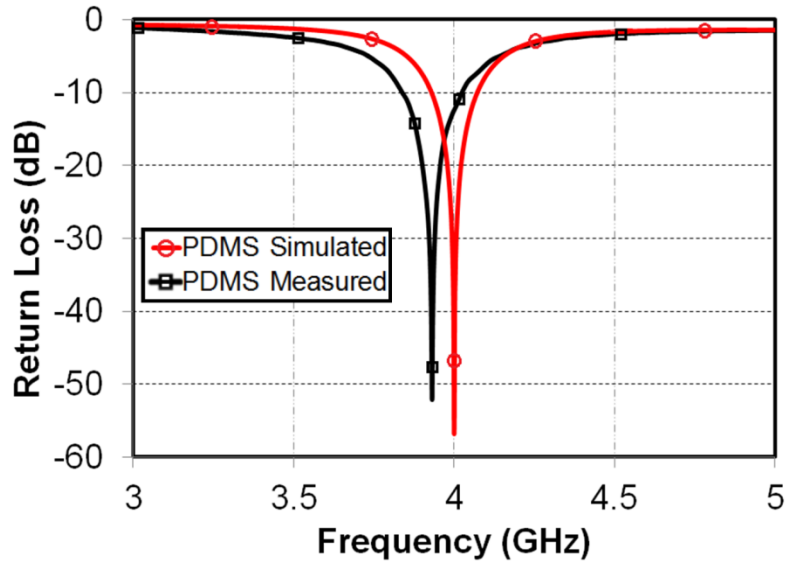
Figure 5.13 – Measured and simulated return loss for the patch antenna on pure PDMS-based molded multilayer substrate, showing acceptable agreement in resonance frequencies.
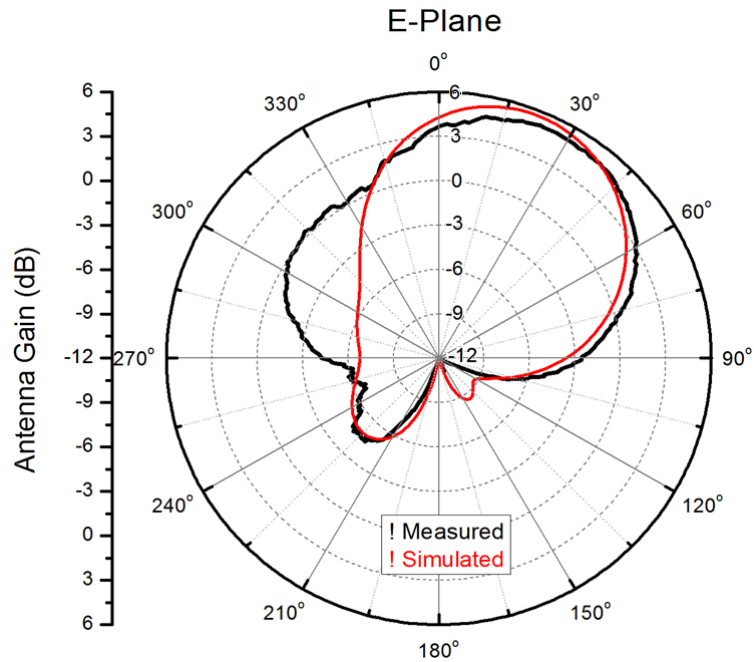
Figure 5.14 – Measured and simulated E-Plane radiation pattern for the patch antenna on molded PDMS-based multilayer substrate.
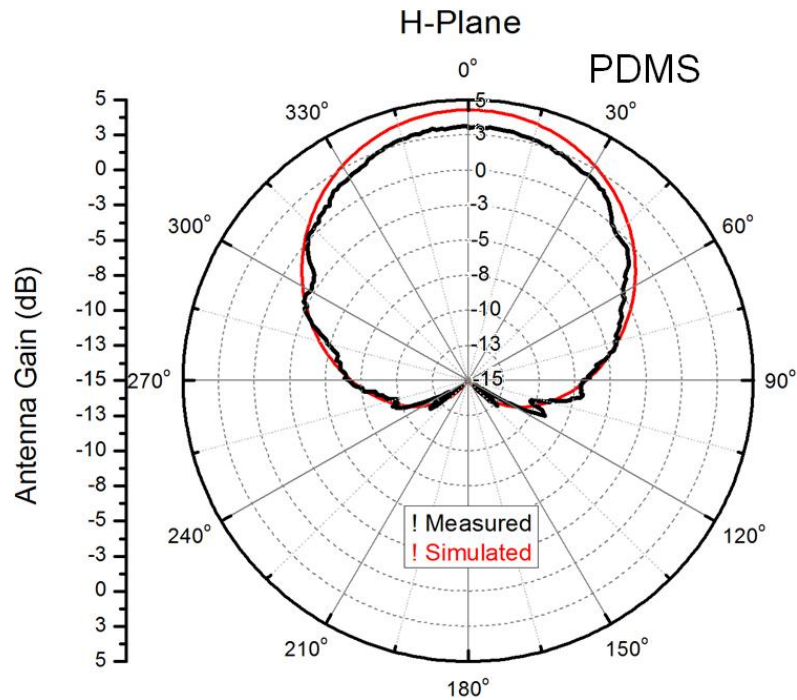
Figure 5.15 – Measured and simulated H-Plane radiation pattern for the patch antenna on molded PDMS-based multilayer substrate.

Also in Figure 5.14, a good agreement in the maximum gain of roughly 5.7 dBi is obtained between simulation and measurement. The existence of a back lobe, with a maximum magnitude of 0 dBi, is observed as the major difference between simulated and measured radiation patterns. However, as seen in Table 5.1, such differences do not lead to any appreciable changes in the antenna parameters (maximum gain, directivity and efficiency).

Table 5.1 – Antenna parameters of plain PDMS-based substrate design.

Description	Resonance Frequency (GHz)	Bandwidth (MHz)	Maximum Gain (dBi)	Directivity (dB)	Total Efficiency
Simulated PDMS Antenna	4.002	145 (3.6%)	5.693	8.441	53.11%
Measured PDMS Antenna	3.931	185 (4.7%)	5.681	8.527	51.91%

Figure 5.15 shows the measured and simulated H-plane gain patterns, depicting the shape which corresponds to a microstrip patch antenna (i.e. maximum gain at 0°). As the beam is slightly more tilted in the constructed (measured) antenna, relatively lower gain has been extracted from measured radiation pattern as compared with simulated result. In the H-plane, the maximum gain values are 4.28dBi and 2.98dBi for simulation and measurement, respectively.

Figure 5.16 shows the measured gain versus frequency of the as-built PDMS multilayer patch antenna. The small ripples in the plot are produced by the vibrations of the rotation mechanism under which the flexible antenna under test is connected at the moment of the radiation pattern measurements. As observed, a maximum gain of 5.681dBi and 5,095dBi are registered at 3.931GHz and 4GHz respectively, providing an excellent agreement between simulated and measured results.
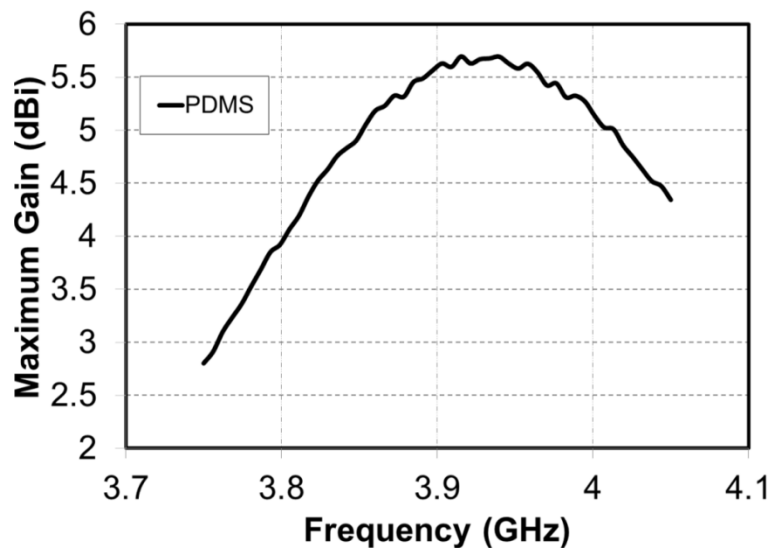
Figure 5.16 – Measured gain vs. frequency for the multilayer patch antenna on molded PDMS-based substrate.

5.4.2 Multilayer Microstrip Patch Antenna with PDMS-Fe$_3$O$_4$ PNC Filler at 80% w.t. Concentration

Simulated and measured return losses for the multilayer patch antenna with PDMS-Fe$_3$O$_4$ PNC at 80% w.t. concentration are shown in Figure 5.17. An excellent agreement between resonance frequency and bandwidth can be observed, however some discrepancy in the return loss is exhibited, which may be ascribed to different impedance matching conditions. As mentioned before, the inclusion of the SMA feeding connector can add some variations to the response of the measured antenna, as well as the preciseness of the finite element method for the antenna simulation.
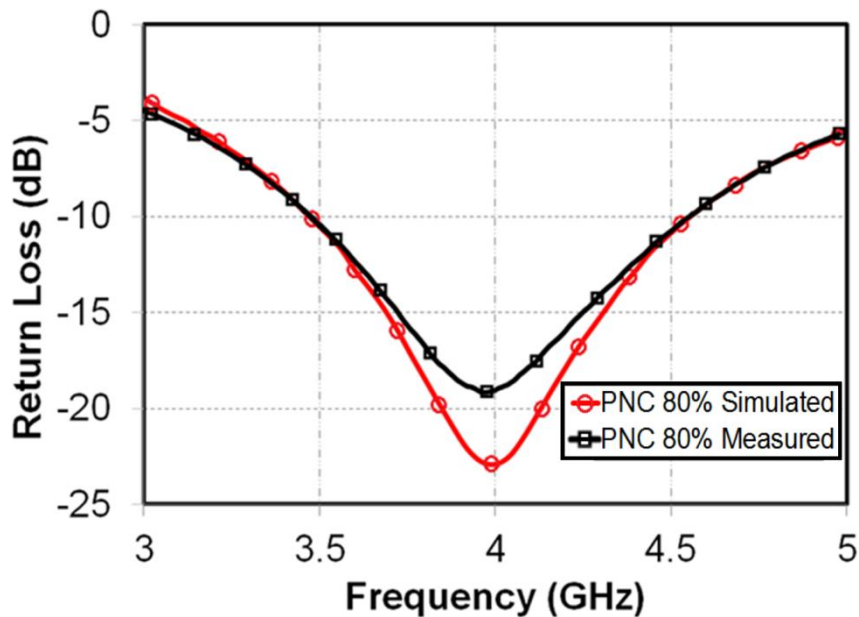
Figure 5.17 – Return loss for microstrip the multilayer patch antenna with PDMS-Fe$_3$O$_4$ PNC at 80% w.t.

The E-Plane and H-Plane radiation patterns are shown in Figures 5.18 and 5.19. The shape of the measured radiation pattern is consistent with the simulated result, keeping very similar antenna gain and efficiency. However, in

95

Figure 5.18 the main lobe appears tilted by 25° and 33° in the simulation and measured characteristics, respectively. The difference in the beam tilting is also reflected in the H-plane, where small discrepancies between the magnitudes of measured and simulated radiation patterns are depicted.

Figure 5.18 – Measured and simulated E-Plane radiation pattern for the multilayer patch antenna on 80% w.t. PDMS-Fe$_3$O$_4$ PNC-based substrate.

The main lobe presents more tilting in the 80% Fe$_3$O$_4$ PNC antenna than in the pure PDMS antenna, which is caused by a stronger effect of the 50Ω microstrip feeding on the patch current distribution. This effect is clearly given that the width of the patch has been decreased for the purpose of antenna miniaturization, while the width of the feeding microstrip line has been kept constant. This phenomenon is not related to the use of magneto-dielectric materials, as it occurred in the pure PDMS patch antenna which contains

96

dielectric only materials. Additionally, the beam tilting is present for the next two cases (PDMS-Fe_3O_4 PNC at 50% and 30%) with almost the same angle. It can be thus concluded that the beam tilting phenomena is a purely geometrical size effect, as the three last designs share the same physical configuration and dimensions.

Figure 5.19 – Measured and simulated H-Plane radiation pattern for the multilayer patch antenna on 80% w.t. PDMS-Fe_3O_4 PNC-based substrate.

Table 5.2 presents a comparison of measured and simulated antenna parameters for the design with PDMS-Fe_3O_4 PNC at 80% w.t. substrate, evidencing excellent agreements achieved between measured and simulated results. Additionally, the constructed antenna presents maximum gain of 1.428dBi and a directivity of 7.698dB leading to a total efficiency of 12.23%. The performance of this antenna is severely affected by the increased loss of the PNC with high loading concentration of Fe_3O_4 nanoparticles. However, the

antenna performance is substantially improved by means of externally applied DC biasing magnetic fields, which will be discussed later in this chapter.

Table 5.2 – Antenna parameters for the PDMS-Fe$_3$O$_4$ PNC 80% w.t. substrate design.

Description	Resonance Frequency (GHz)	Bandwidth (MHz)	Maximum Gain (dBi)	Directivity (dB)	Total Efficiency
Simulated PNC 80% Antenna	3.999	1071 (26.78%)	-1.453	7.650	12.31%
Measured PNC 80% Antenna	3.981	1072.5 (26.95%)	-1.428	7.698	12.23%

5.4.3 Multilayer Microstrip Patch Antenna with PDMS-Fe$_3$O$_4$ PNC Filler at 50% w.t. Concentration

Simulated and measured return loss for the multilayer patch antenna with PDMS-Fe$_3$O$_4$ PNC at 50% concentration is depicted in Figure 5.20, showing good agreements. Minor discrepancies are found and seemed to be related to differences in the matching of the patch to the 50Ω microstrip feed line.
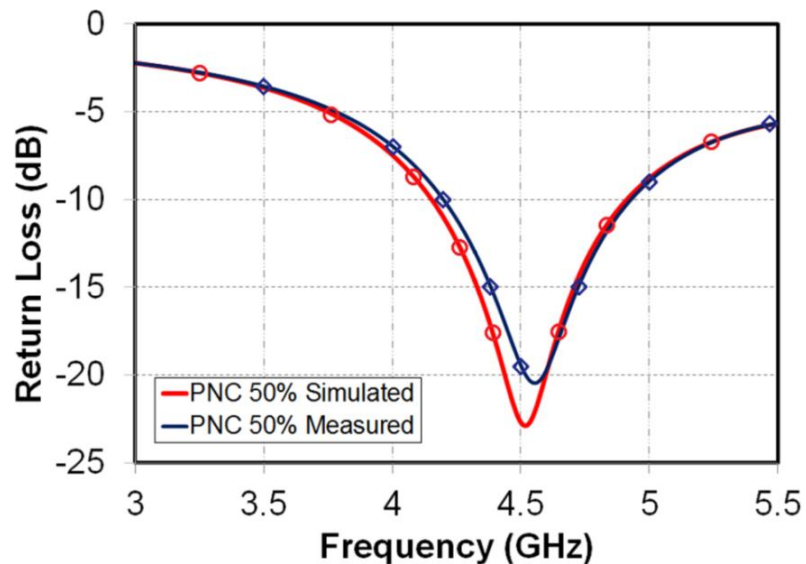
Figure 5.20 – Return loss for microstrip multilayer antenna with PDMS-Fe$_3$O$_4$ PNC at 50% w.t.

E-plane and H-plane radiation patterns are depicted in Figures 5.21 and 5.22, respectively. In the E-plane, maximum antenna gains of 0.62dBi at 24° and 1.2dBi at 32° are observed from simulated and measured results, respectively. This results evidence once again a beam tilting, with angles very similar to those obtained in the design with PNC at 80% w.t., dismissing a direct correlation between the PNC material properties and the inclination of the beam. Additionally, this beam tilting causes a difference in the measured and simulated gains depicted in the H-plane radiation patterns.
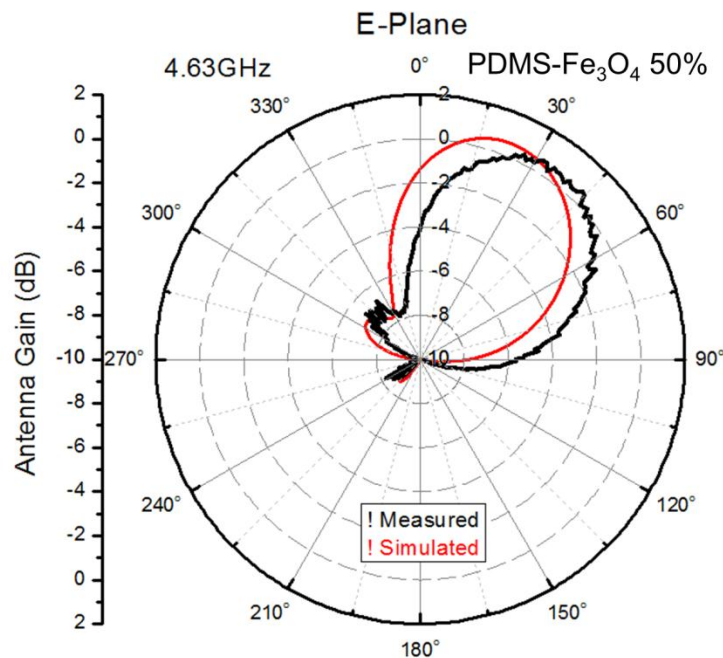
Figure 5.21 – Measured and simulated E-Plane radiation pattern for the multilayer patch antenna on 50% w.t. PDMS-Fe$_3$O$_4$ PNC-based substrate.
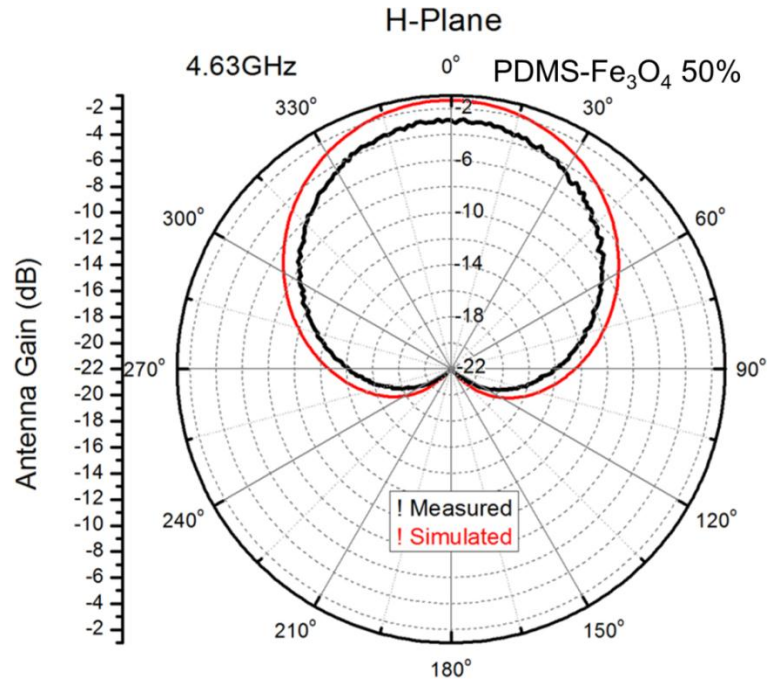
Figure 5.22 – Measured and simulated H-Plane radiation pattern for the multilayer patch antenna on 50% w.t. PDMS-Fe$_3$O$_4$ PNC-based substrate.

Table 5.3 presents the relevant parameters of the PDMS-Fe$_3$O$_4$ PNC 50% w.t. antenna design, providing a better appreciation of the agreement between simulated and measured results. The elaborated 50% PNC antenna presents more attractive performance metrics than those achieved in the 80% PNC design. For instance, maximum gain of 1.206dBi, directivity of 8.07dB, and total efficiency of 17.90% have been achieved in the 50% PNC design. However, a narrower bandwidth of 16.04% and a higher resonance frequency of 4.552GHz, which suggests a reduction in the miniaturization factor, have been achieved. A more detailed analysis regarding to these results will be presented later in this chapter.

Table 5.3 – Antenna parameters for the PDMS-Fe_3O_4 PNC 50% w.t. substrate design.

Description	Resonance Frequency (GHz)	Bandwidth (MHz)	Maximum Gain (dBi)	Directivity (dB)	Total Efficiency
Simulated PNC 50% Antenna	4.510	745 (16.52%)	0.815	7.787	20.08%
Measured PNC 50% Antenna	4.552	730 (16.04%)	0.606	8.070	17.90%

5.4.4 Multilayer Microstrip Patch Antenna with PDMS-Fe_3O_4 PNC Filler at 30% w.t. Concentration

Return loss for the multilayer patch antenna with PDMS-Fe_3O_4 PNC at 30% w.t. is shown in Figure 5.23, presenting an excellent agreement between measured and simulated results. Minor discrepancies are found in the impedance matching of the antenna, but good matching between the frequency responses obtained for both approaches.
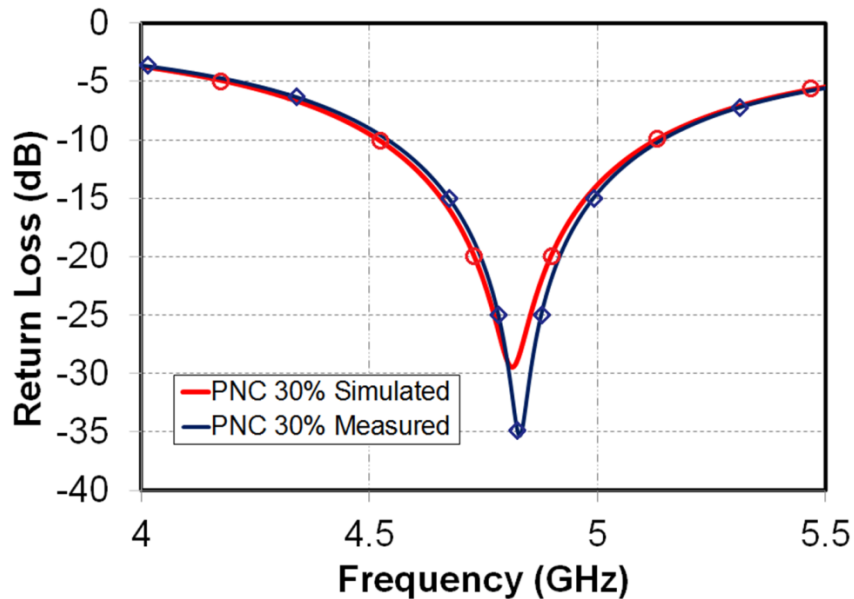
Figure 5.23 – Return loss for the microstrip multilayer antenna with PDMS-Fe_3O_4 PNC at 30% w.t.

E-plane and H-plane radiation pattern plots are depicted in Figures 5.24 and 5.25, respectively. The maximum antenna gains of 2.06dBi at 24° and 1.49dBi at 33° are observed from simulated and measured results in the E-plane, respectively.
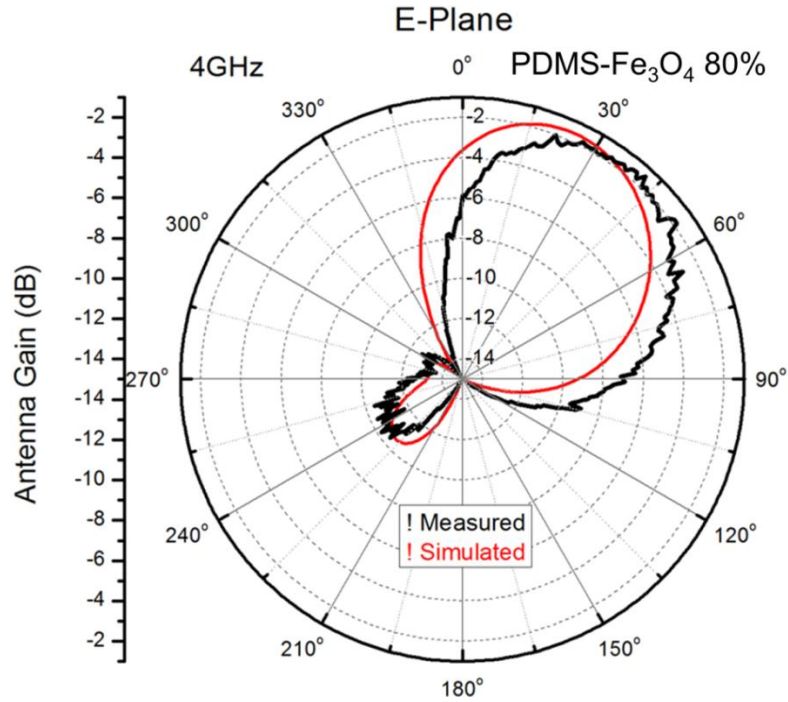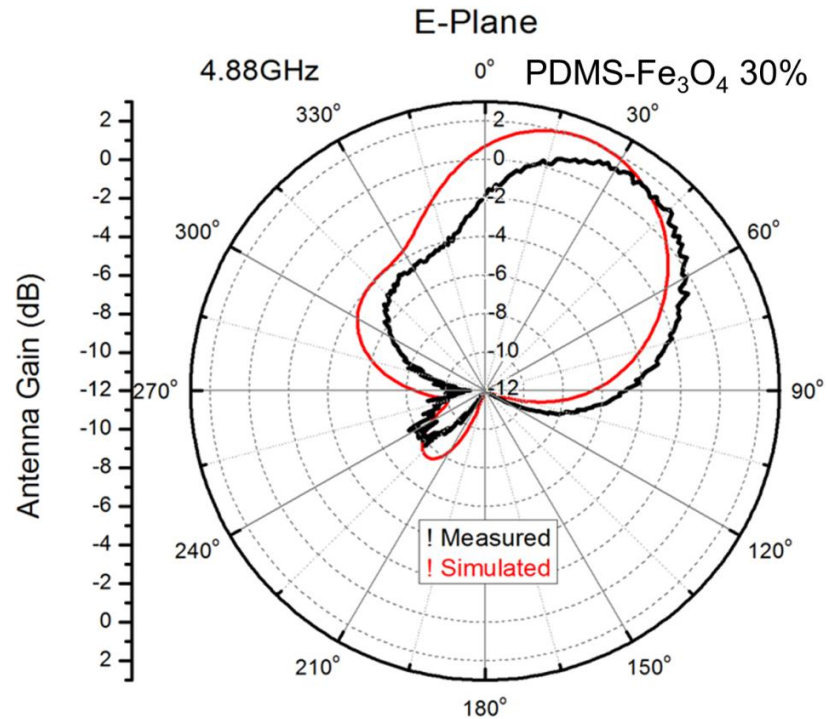

Figure 5.24 – Measured and simulated E-Plane radiation pattern for the multilayer patch antenna on 30% w.t. PDMS-Fe_3O_4 PNC-based substrate.
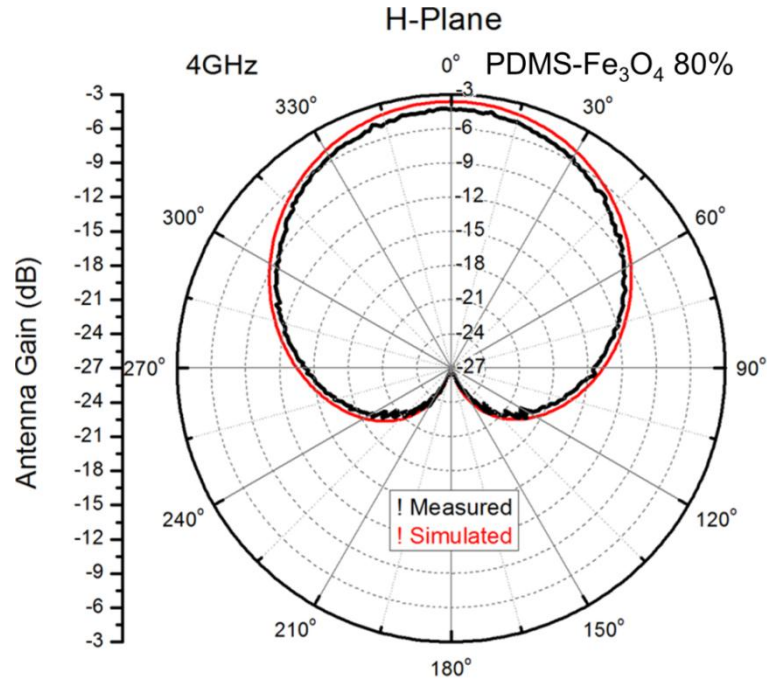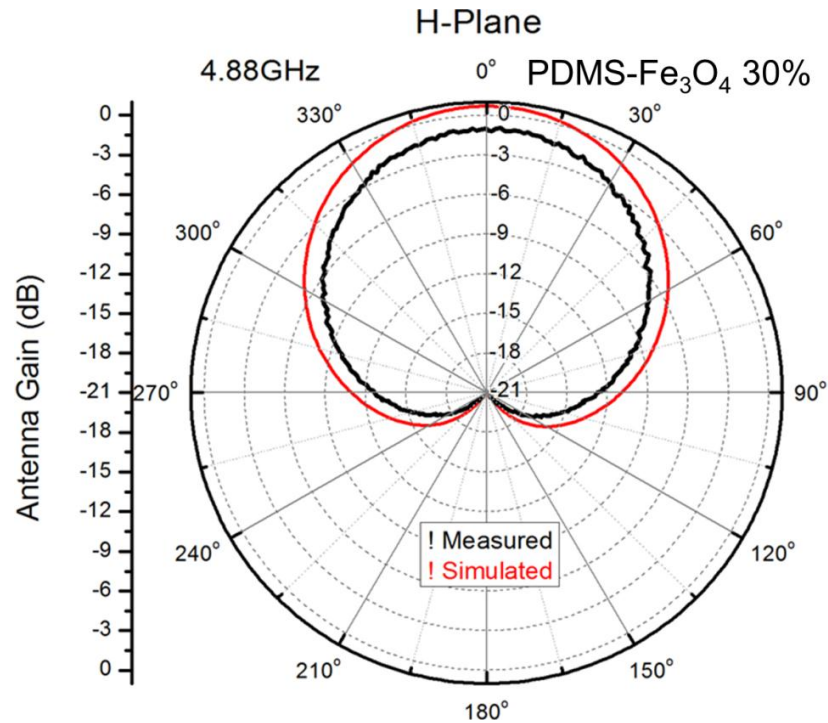
Figure 5.25 – Measured and simulated H-Plane radiation pattern for the multilayer patch antenna on 30% w.t. PDMS-Fe$_3$O$_4$ PNC-based substrate.

Table 5.4 presents a comparison of measured and simulated antenna parameters for the design with the PDMS-Fe$_3$O$_4$ PNC 30% w.t. substrate, providing a better appreciation of the good agreement between simulated and measured results. For the realized antenna, measured performance metrics are more attractive than those achieved in the designs with PNC at 80% w.t. and PNC at 50% w.t. For instance, maximum gain of 2.003dBi, directivity of 8.203dB, and total efficiency of 23.98% have been obtained for this last design, surpassing the results obtained in the other two designs that implement PNCs as substrate fillers. However, the performance metrics of the PNC at 30% w.t. design are not significantly better than those in the PNC 50% w.t. design, as the antenna now exhibits a narrower bandwidth of 12.37% and a higher resonance frequency of

4.832GHz, which corresponds to the reduction of the miniaturization factor. More detailed analysis regarding to these results will be provided later in this chapter.

Table 5.4 – Antenna parameters for the PDMS-Fe_3O_4 PNC 30% w.t. substrate design.

Description	Resonance Frequency (GHz)	Bandwidth (MHz)	Maximum Gain (dBi)	Directivity (dB)	Total Efficiency
Simulated PNC 30% Antenna	4.796	595 (12.40%)	1.987	8.415	22.76%
Measured PNC 30% Antenna	4.832	597.5 (12.37%)	2.003	8.203	23.98%

5.5 Performance Comparison of Multilayer Patch Antennas Built on PDMS-Fe_3O_4 PNC Substrates with Different Particle Loading Concentrations

A systematic analysis of the performance of the antennas is developed, comparing the measurement results obtained from the different designs (PDMS, 80% PNC, 50% PNC and 30% PNC). The primary antenna performance metrics, such as return loss, antenna radiation pattern, maximum gain, directivity and antenna efficiency are analyzed and explored for each design.

Initially, comparisons between the as-constructed antennas are presented without the presence of any biasing magnetic field. Subsequently, comparisons are carried out among the measurement results obtained while a DC biasing magnetic field is applied to the antennas through the employment of a permanent magnet in close proximity to the embedded PNC material.

5.5.1 Performance of PDMS-Fe_3O_4 PNC Multilayer Antennas without Externally Applied DC Biasing Magnetic Field

Figure 5.26 compares the return losses multilayer antennas constructed on the pure PDMS substrate and the PDMS-Fe_3O_4 PNC at 80% w.t. antennas

substrate. Both devices were designed to operate at 4GHz, resulting in resonance frequencies of 3.931GHz and 3.981GHz for the PDMS and 80% PNC designs, respectively. By direct comparison of the return loss responses, the 80% PNC antenna presents an attractive widened bandwidth of 26.95%(1072.5MHz), which is 5.7 times wider than the bandwidth of 4.7%(185MHz) of its plain PDMS counterpart.
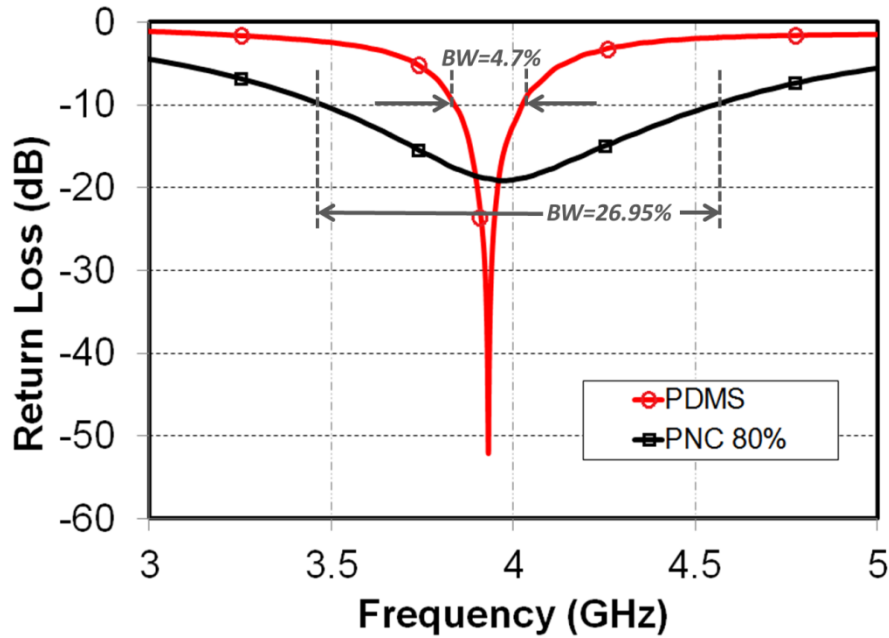
Figure 5.26 – Measured return losses for plain PDMS and 80% w.t. PDMS-Fe$_3$O$_4$ PNC multilayer patch antennas.

As both antennas were designed for 4GHz operation, direct size comparison between them can be performed by measuring the areas of the patches. The miniaturization achieved by the use of PDMS-Fe$_3$O$_4$ PNC at 80% w.t. concentration is evaluated by the calculation of the miniaturization percentage and the miniaturization factor as follows:

$$miniaturization\ percentage = \frac{A_a - A_{ma}}{A_a} \times 100\% \qquad (5.3)$$

$$miniaturization\ factor = \frac{A_a}{A_{ma}} \qquad\qquad (5.4)$$

where A_a and A_{ma} are the physical areas of the original antenna (i.e., PDMS antenna) and miniaturized antenna (i.e. PDMS-Fe$_3$O$_4$ PNC antenna), respectively.

As mentioned in the section 5.2, the areas of the antenna patches are 594.05mm^2 and 312.05mm^2 for the PDMS design and the 80% PNC design, respectively. Taking into consideration these areas, miniaturization percentage of 47.5% or miniaturization factor of 1.9 are achieved by using the PDMS-Fe$_3$O$_4$ PNC at 80% w.t. in the multilayer antenna configuration. Figure 5.27 clearly shows the antenna miniaturization achieved by using embedding the PNC underneath the antenna patch.
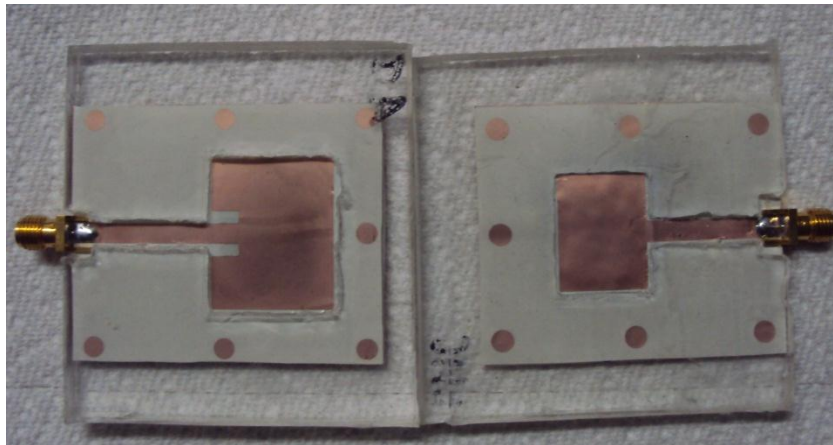
Figure 5.27 – Top-view photo of plain PDMS (left) and 80% w.t. PDMS-Fe$_3$O$_4$ PNC (right) multilayer patch antennas. A notable antenna patch size reduction of 47.5% has been achieved by the employment of 80% PNC as compared to that of the plain PDMS antenna.

However, the pure PDMS patch obtained an acceptable efficiency of 51%, which is much better than the 12.2% efficiency obtained by the 80% PNC antenna. Although an increased bandwidth is expected, caused by the magneto-

dielectric properties of the 80% PNC substrate, such a great difference in the bandwidth is mainly caused by the high loss property introduced by the PNC material, which lowers the antenna quality factor and leads to an increased bandwidth at expenses of degrading the antenna efficiency.
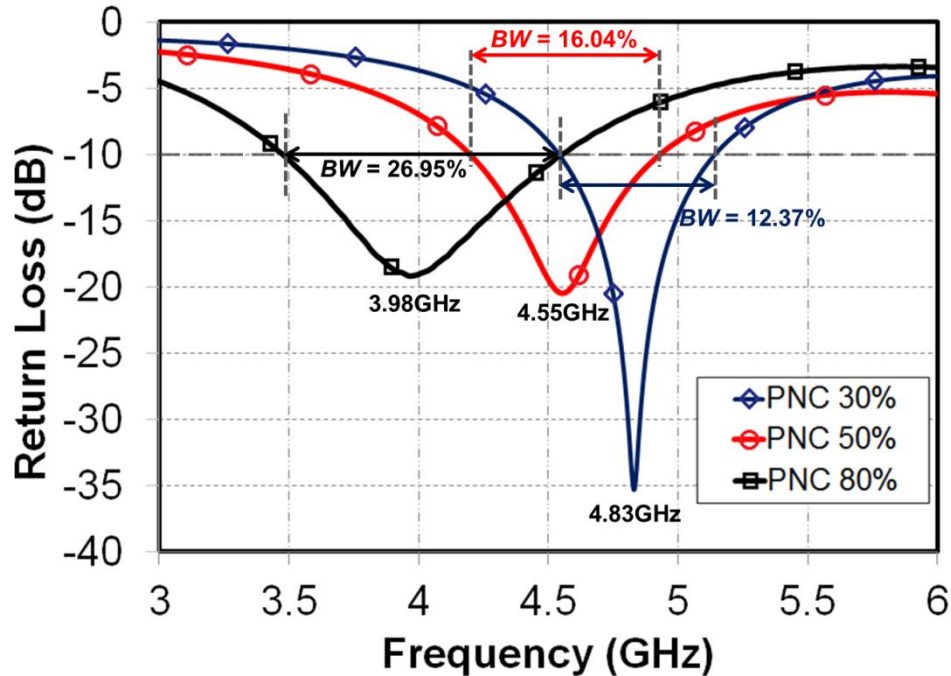
Figure 5.28 – Measured return losses of PDMS-Fe$_3$O$_4$ PNC multilayer patch antennas at 30%, 50% and 80% w.t. concentrations.

Figure 5.28 shows the measured return losses of three multilayer patch antennas with embedded PDMS-Fe$_3$O$_4$ PNCs at different particle loading concentration (80%, 50% and 30%). All these multilayer patch antennas have the same physical dimensions, therefore the different values of effective permittivity ε_r and permeability μ_r for each concentration of PNC can be evidently observed by the frequency offsets between the three patch antennas. The higher the concentration of nanoparticles in the PNC, the higher the product of permittivity

and permeability (i.e. $\mu_r \times \varepsilon_r$) is, and then lowering the antenna resonance frequency.

As the PNC antennas share the same physical dimensions, size comparisons between them are conducted using their resonance frequencies. All antenna sizes can be evaluated by finding their enlargement percentage compared to the PNC 80% multilayer antenna EP_{PNCx}:

$$EP_{PNCx} = \frac{f_{PNCx} - f_{PNC80}}{f_{PNC80}} \times 100\% \qquad (5.5)$$

where f_{PNC80}=3.981GHz is the resonance frequency of the 80% PNC multilayer patch antenna (i.e. the reference antenna) and f_{PNCx} is the resonance frequency of the PNC multilayer antenna with different particle loading concentration.

For the 50% PNC multilayer patch antenna EP_{PNC50}=14.34%, which means that this antenna patch is 14.34% larger than the 80% PNC counterpart. Similarly, for the 30% PNC device, EP_{PNC30}=17.61% was obtained.

To obtain a direct comparison between the plain PDMS multilayer patch antenna and the antennas with different PNC concentrations, and then reveal the effective miniaturization factor, the concept of equivalent area ($EA_{PNCx[f]}$) is hereby introduced. $EA_{PNCx[f]}$ is the equivalent patch area required to build a multilayer patch antenna at the same resonance frequency of the reference antenna by using the PNC filler material. $EA_{PNCx[f]}$ is found as:

$$EA_{PNCx[f]} \cong A_{PNCx} \times \left(1 + \frac{EP_{PNCx}}{100\%}\right) \qquad (5.6)$$

where A_{PNCx} and EP_{PNCx} are the physical area and the enlargement percentage of the referenced antenna. EP_{PNCx} was calculated using Equation (5.5).

In order to obtain a resonance frequency of 3.981GHz (i.e. resonance frequency of the PNC 80% multilayer patch antenna), the equivalent area for the 50% PNC is calculated using Equation (5.6):

$$EA_{PNC50[3.981GHz]} = A_{PNC50} \times \left(1 + \frac{EP_{PNC50}}{100\%}\right)$$

$$EA_{PNC50[3.981GHz]} = 312.05mm^2 \times \left(1 + \frac{14.34\%}{100\%}\right) = 356.81mm^2$$

Also, from Equation (5.6), the equivalent area at a resonance frequency of 3.981GHz is obtained for the 30% PNC antenna patch:

$$EA_{PNC30[3.981GHz]} = A_{PNC30} \times \left(1 + \frac{EP_{PNC50}}{100\%}\right)$$

$$EA_{PNC30[3.981GHz]} = 312.05mm^2 \times \left(1 + \frac{17.61\%}{100\%}\right) = 367.01mm^2$$

Now, considering the PDMS antenna as the benchmark device, the miniaturization percentage for the 50% PNC and 30% PNC antennas can be calculated using Equations (5.3) and (5.4), by replacing A_{ma} with the calculated equivalent antenna areas:

$$miniaturization\ percentage = \frac{A_a - EA_{PNCx[f]}}{A_a} \times 100\% \qquad (5.7)$$

$$miniaturization\ factor = \frac{A_a}{EA_{PNCx[f]}} \qquad (5.8)$$

From Equations (5.7) and (5.8), the 50% PNC antenna patch presents miniaturization percentage of 39.9% and miniaturization factor of 1.66. Similarly, for the 30% PNC antenna, miniaturization percentage of 36.2% (miniaturization factor of 1.57) was achieved.

Figure 5.29 presents the measured maximum gain in dBi for each one of the PNC multilayer patch antennas. It is worthwhile mentioning that the antenna

gain decreases as the concentration of Fe_3O_4 nanoparticles increases, clearly indicating that the additional losses at RF/microwave frequencies are gradually introduced as the concentration of magnetic nanoparticles in the PNC increases. In addition, the maximum gain is shifted towards higher frequencies as the nanoparticle concentration decreases, which the resonance frequencies shown in Figure 5.28. As mentioned before, for antennas with the same geometrical configuration and size, frequency shifting towards higher frequencies reflects a decrease of the product of relative permeability and permittivity ($\mu_r \times \varepsilon_r$), thus resulting in an increase of the effective wavelength.
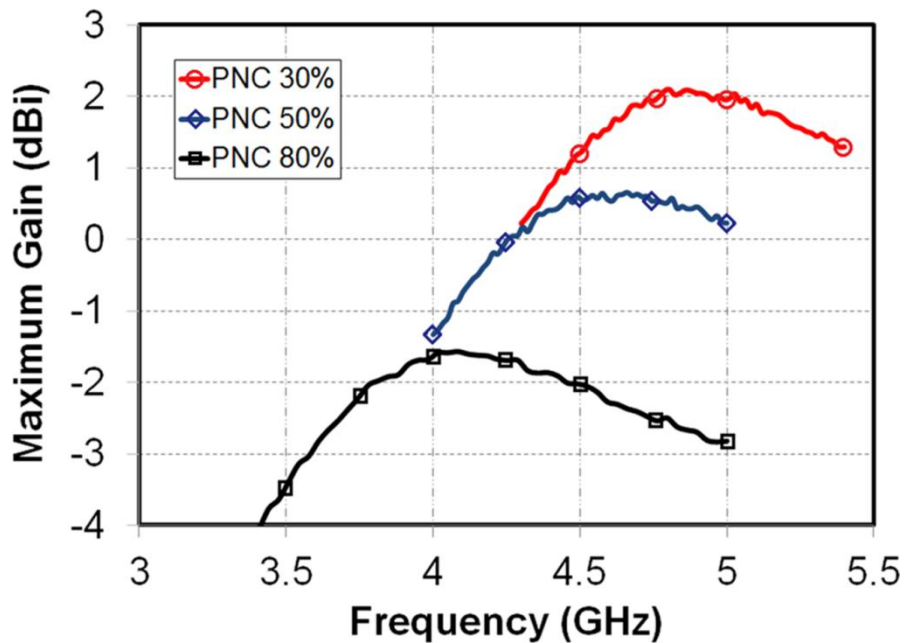
Figure 5.29 – Measured gain of PDMS-Fe_3O_4 PNC multilayer patch antennas at 30%, 50% and 80% w.t. concentrations.

Table 5.5 presents a comparison of measured key performance metrics for all four multilayer patch antenna designs without any applied DC biasing magnetic field. The antenna designs are discriminated by the PNC materials

used as the cavity filler underneath the antenna patch. From this table, it is possible to observe the impact of permeability and permittivity on the antenna miniaturization as discussed in chapter 2. In addition, the antenna bandwidth and efficiency are strongly affected by the dielectric and magnetic losses presented in the substrate fillers, properties which are inherent to the concentration of magnetite nanoparticles in the PNC.

Table 5.5 – Multilayer patch antennas and their relevant properties without any applied biasing magnetic field

Antenna Design	Resonance Frequency (GHz)	Bandwidth (MHz)	Maximum Gain (dBi)	Efficiency	Area (mm^2)	Miniaturization % / Factor
PDMS	3.931	185 (4.7%)	5.681	50.74%	594.05 (27.25x21.8)	---
PDMS-Fe$_3$O$_4$ 80% PNC	3.981	1072.5 (26.95%)	-1.428	12.23%	312.05 (19.75x15.8)	» 47.5% / 1.9
PDMS-Fe$_3$O$_4$ 50% PNC	4.552	730 (16.04%)	0.606	17.90%	312.05 (19.75x15.8)	» 39.9% / 1.66
PDMS-Fe$_3$O$_4$ 30% PNC	4.832	597.5 (12.37%)	2.003	23.98%	312.05 (19.75x15.8)	» 36.2% / 1.57

Increasing the Fe$_3$O$_4$ nanoparticle concentration also raises the PNC material effective permeability thus leading to a wider antenna bandwidth. However, this is accompanied by the increase of additional material losses, which contributes to a significant increase of the bandwidth and a degradation of the antenna efficiency. Fortunately, the additional losses and the antenna gain/efficiency degradation can be addressed by means of externally applied DC biasing magnetic fields as detailed in the next section.

Table 5.6 – Electrical properties of PNC substrates without any applied DC biasing magnetic field.

Substrate Filler	Resonance Frequency (GHz)	Permeability μ_r	Permittivity ε_r	Dielectric Loss Tangent $tan\delta_d$	Magnetic Loss Tangent $tan\delta_m$
PDMS	3.931	2.69	1	0.021	-
PDMS-Fe$_3$O$_4$ 80% PNC	3.981	2.31	2.49	0.19	0.15
PDMS-Fe$_3$O$_4$ 50% PNC	4.552	2.71	1.43	0.12	0.1
PDMS-Fe$_3$O$_4$ 30% PNC	4.832	2.85	1.18	0.07	0.06

Table 5.6 summarizes the electrical properties of the PDMS-based substrate filler materials used in all four antenna designs. This table provides the effective substrate material properties to facilitate a better correlation between them and the measured antenna performance metrics shown in Table 5.5. Note that material electric properties are provided for each material at the respective resonance frequency of each antenna design using these fillers.

5.5.2 Performance of PDMS-Fe$_3$O$_4$ PNC Multilayer Antennas with Externally Applied DC Biasing Magnetic Field

Magneto-dielectric Fe$_3$O$_4$–based PNC has demonstrated tunability of its dielectric and magnetic properties by the application of external DC biasing magnetic fields, thereby reducing its dielectric and magnetic losses as the strength of the magnetic field increases [14]. Moreover, as shown in Figures 4.23 and 4.24, the quality factor Q and the resonance frequency for a microstrip linear resonator in similar multilayer PNC configuration were modulated by tuning the complex permittivity and permittivity using external DC biasing magnetic field.

The same experiment is repeated in order to demonstrate the susceptibility of the dielectric and magnetic properties of PDMS-Fe_3O_4 PNC to the externally applied DC biasing magnetic field. Basically, the employment of moderate level of DC magnetic field result in substantial reduction of the dielectric and magnetic loss tangents (i.e. $tan\delta_d$ and $tan\delta_m$), along with a noticeable increase of relative permittivity and permeability thus enabling for more antenna miniaturization.

A stack array composed of 3 Neodymium magnets was assembled to provide biasing DC magnetic field to the PDMS-Fe_3O_4 PNC embedded in the multilayer patch antenna. The biasing magnetic field has been measured using a DC gauss-meter (Model 1-ST from AlphaLab™ Inc.), at 130mils (3.3mm) of distance from the surface, providing the approximate magnetic field strength exerted on the embedded PNC. The gauss-meter readings showed a magnetic field of 0.35 Tesla close to the edges and 0.20 Tesla at the center of the magnet. These values correspond to the best operational conditions, explained in the section 4.4. In addition, each Neodymium magnet has 2.54cm of length, 2.54cm of width and 3mm of thickness, sufficient to cover the area in which the PNCs are embedded in the multilayer antenna structure.

The Neodymium magnet array is placed underneath the patch and center-aligned to PNC-filled cavity but separated by the bottom PDMS layer next to the ground plane. Figures 5.30 (a) and (b) show how the magnet array is placed in contact with the multilayer antenna, while Figures 5.30 (c) and (d) show how the magnet spontaneously attaches to the antenna structure as a consequence of the attraction with the magneto-dielectric PDMS-Fe_3O_4 PNC.

113
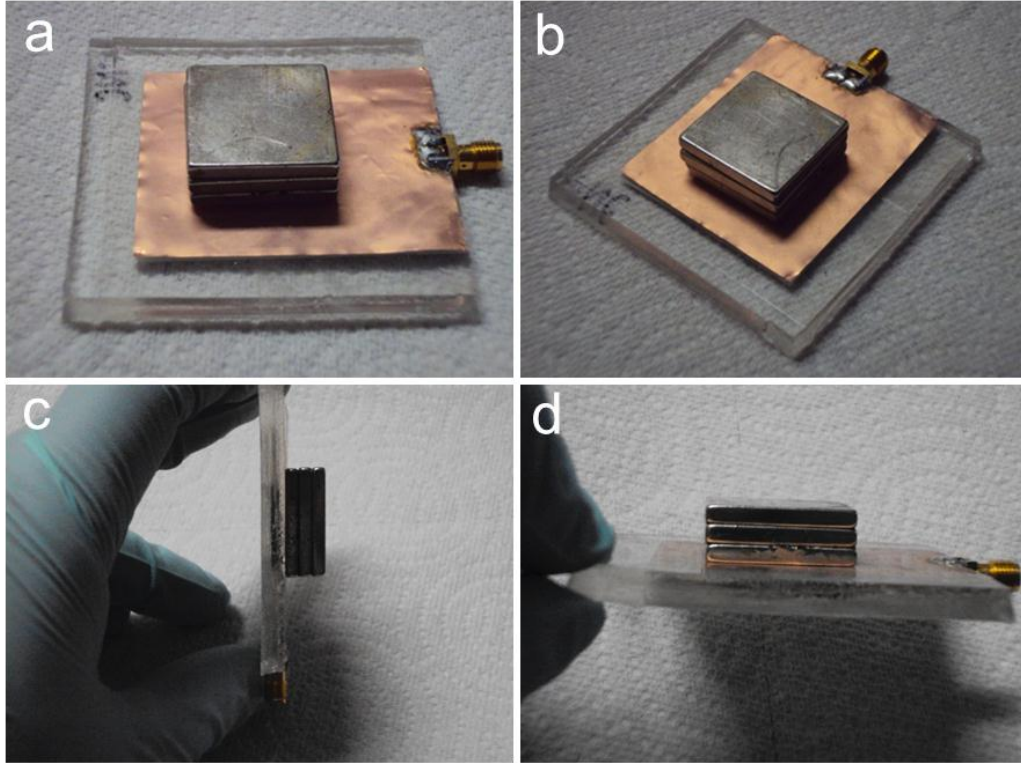
Figure 5.30 – Neodymium magnet array placed in contact with a PDMS-Fe$_3$O$_4$ PNC multilayer antenna. (a) and (b) show how the array is placed in contact with the bottom PDMS layer and center-aligned with the PNC-filled cavity. (c) and (d) show how the magnet array spontaneously attaches to the structure due to the attraction force with the magneto-dielectric PDMS-Fe$_3$O$_4$ PNC.

Unfortunately, given the large variation of the strength of the magnetic field as a function of the position, it is impossible to precisely predict the values of permittivity and permeability of the PNCs under the influence the biasing magnetic field produced by the Neodymium magnet array. Nevertheless, it is anticipated that the influence of the biasing magnetic field is favorable to the decrease of the loss tangent of the PNCs as well as the increment of its relative permeability and permittivity, thus making a positive impact on the antenna performance.
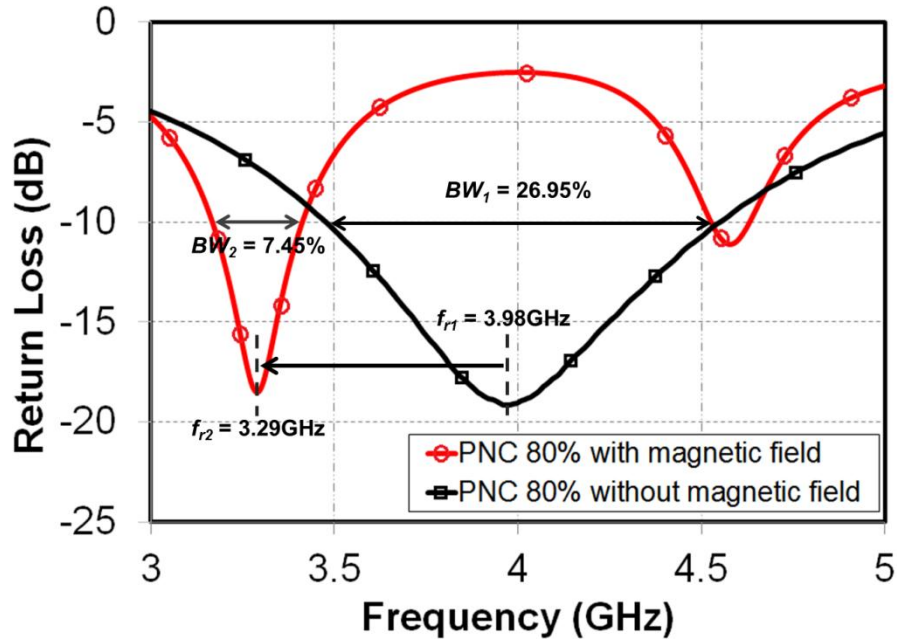
Figure 5.31 – Measured return loss of the PDMS-Fe$_3$O$_4$ PNC multilayer patch antenna at 80% w.t. concentration with and without externally applied DC magnetic field.

Figure 5.31 presents the return loss of the PDMS-Fe$_3$O$_4$ PNC multilayer patch antenna at 80% w.t. concentration, measured under the action of the DC magnetic field provided by the Neodymium magnet array and directly compared to the return loss of the same antenna in absence of magnetic field. As shown, the bandwidth has been reduced considerably from 26.95% to 7.45% under the influence of magnetic field. Although the magneto-dielectric nature of the PNC material has been retained, there is still a field-induced bandwidth reduction, which corresponds to a decrease in the combined dielectric/magnetic losses in the PNC. Moreover, the resonance frequency has been lowered from 3.98GHz to 3.29GHz when magnetic field is applied. As expected, the resonance frequency has dropped to a lower value because of an increase in the product of the relative permeability and permittivity under the influence of DC biasing magnetic field.
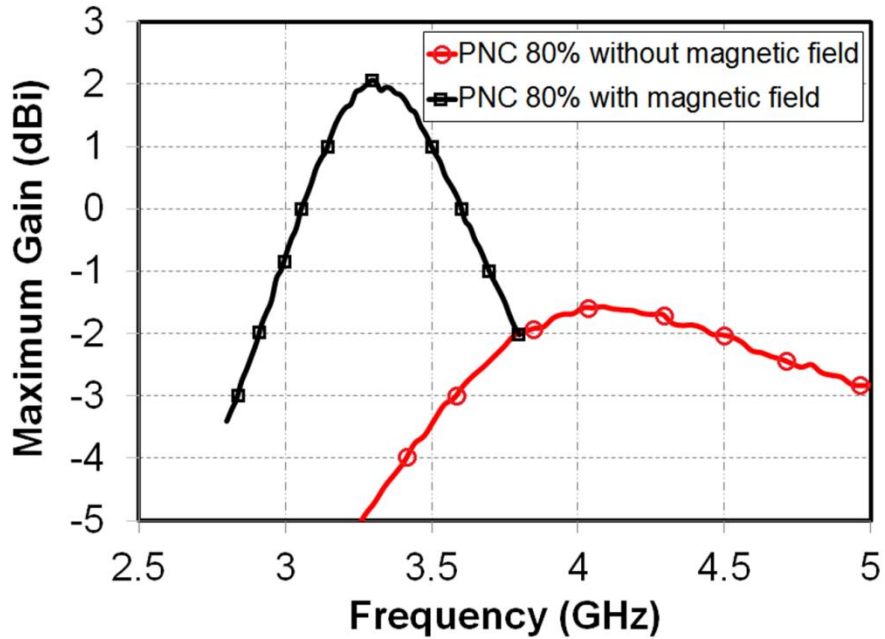
Figure 5.32 – Measured gain of PDMS-Fe$_3$O$_4$ PNC multilayer patch antenna at 80% w.t. concentration with and without DC biasing magnetic field.

Figure 5.32 shows a big contrast between the antenna gain for a device with and without externally applied magnetic field. As shown, the gain has been increased from around -1.5dBi at 3.981GHz without a biasing field to 2dBi at 3.29GHz in the presence of the biasing field, which represents an effective gain increase of 3.5dB or 2.2 times. The increment in the antenna gain and reduction of the antenna bandwidth are clear indications of the reduction of the overall effective loss tangent of the PDMS-Fe$_3$O$_4$ PNC at 80% w.t. concentration due to the presence of the biasing field, and complementing that observed in Figure 5.31.

Figure 5.33 depicts the radiation patterns of antenna built on 80% PNC substrate with and without biasing magnetic field applied. Only the antenna radiation patterns in the E-Plane are here presented here, as it presents enough information about the significant impact of the DC magnetic biasing field on the

antenna radiation characteristics. Notably, the applied DC biasing magnetic field is proven to be instrumental for the enhancing of the antenna gain, while keeping a very similar shape in the radiation pattern.

Figure 5.33 – Measured E-Plane radiation pattern of PDMS-Fe_3O_4 PNC multilayer patch antenna at 80% w.t. concentration with and without applied DC biasing magnetic field.

Table 5.7 presents a comparison of the most relevant antenna performance characteristics measured with and without DC biasing magnetic field applied. The resonance frequency has shifted to a lower frequency, with a frequency drift of 683MHz, indicating that enhanced miniaturization factor is achieved under the presence of the magnetic field. The reduction in the effective loss tangent in the magneto-dielectric material, under the influence of the magnetic field, is evidenced by the augment of the antenna gain and efficiency as well as by the reduction of the antenna bandwidth.

Table 5.7 – Antenna parameters of PDMS-Fe_3O_4 PNC 80% w.t. substrate design with and without applied external DC biasing magnetic field.

Description	Resonance Frequency (GHz)	Bandwidth (MHz)	Maximum Gain (dBi)	Directivity (dB)	Total Efficiency
PNC 80% Antenna with magnetic field applied	3.290	245 (7.45%)	2.02	7.167	30.57%
PNC 80% Antenna without magnetic field applied	3.981	1072.5 (26.95%)	-1.428	7.698	12.23%

In a similar manner, the other two PDMS-Fe_3O_4 antennas were measured under the application of the DC biasing magnetic field produced by the neodymium magnet array.

Figure 5.34 – Measured return loss of PDMS-Fe_3O_4 PNC multilayer patch antenna at 50% w.t. concentration with and without applied magnetic field.

As shown in Figure 5.34, the multilayer patch antenna with embedded PNC at 50% also responded to the DC magnetic field stimulus by changing its resonance frequency and bandwidth. This is caused by the same field-induced

property variations explained in the previous section for the antenna with 80% PNC. For the case of 50% PNC design, the measured frequency shift is 566MHz, which is less severe given the relatively lower concentration of Fe_3O_4 nanoparticles. Furthermore, less miniaturization can be achieved, with the employment of biasing magnetic fields, since the nanoparticle loading concentration has been reduced herein as compared with the 80% PNC design.
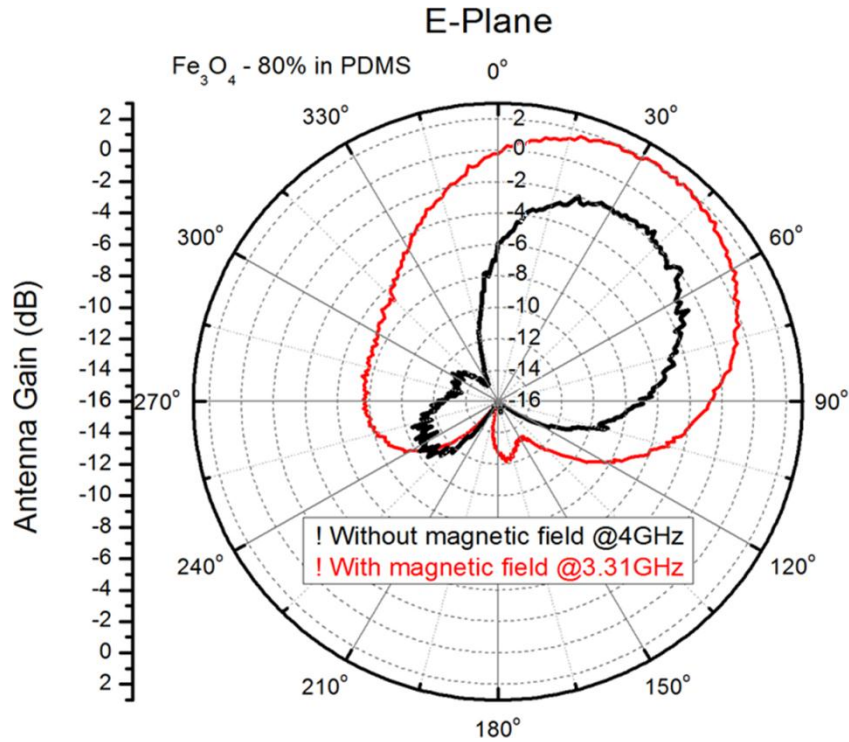

Figure 5.35 – Measured E-Plane radiation pattern of PDMS-Fe_3O_4 PNC multilayer patch antenna at 50% w.t. concentration with and without applied magnetic field.

Figure 5.35 shows the radiation E-plane radiation patterns of the 50% PDMS-Fe_3O_4 PNC design, with and without applied DC biasing magnetic field. As expected, the 50% PNC exhibited a reduction of its total loss tangent when

the biasing magnetic field was applied, thus causing a notable increase of the antenna gain while keeping a very similar radiation pattern characteristics.

Figure 5.36 presents a better contrast between the antenna gain with and without applied magnetic field versus frequency. As shown, the gain has increased from 0.606dBi at 4.55GHz without biasing field to 4.063dBi at 3.986GHz in the presence of biasing field, which represents an effective gain increase of 3.457dB or 2.2 times. It is worthwhile mentioning that the increment in the gain was similar to the measured result for the 80% PNC antenna. The augment in antenna gain and reduction in antenna bandwidth are clear indications of the reduction of the overall effective loss tangent of the 50% PDMS-Fe_3O_4 PNC when DC biasing magnetic field is applied by the usage of the neodymium magnet array.

Figure 5.36 – Measured gain of PDMS-Fe_3O_4 PNC multilayer patch antenna at 50% w.t. concentration with and without applied DC biasing magnetic field.

The last antenna design with embedded 30% PNC also responded to the DC biasing magnetic field stimulus by changing its resonance frequency and bandwidth as shown in Figure 5.37. For this case the measured frequency shifting is 247MHz, which is less severe than those of the 80% PNC and 50% PNC designs. Furthermore, less field susceptibility and less miniaturization are also observed from 30% PNC design. These effects can be ascribed to lower loading concentration of Fe_3O_4 nanoparticles in the PDMS nanocomposites.
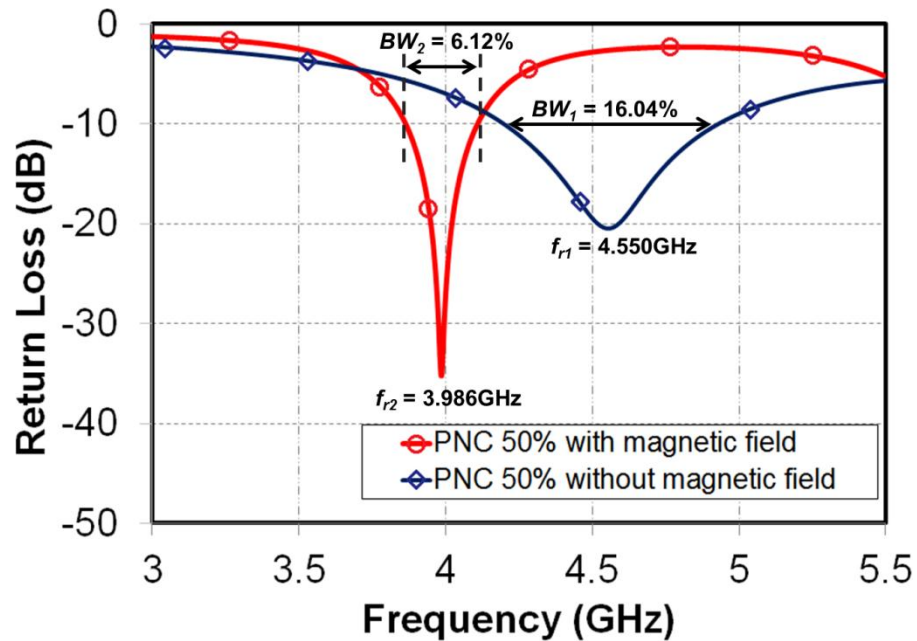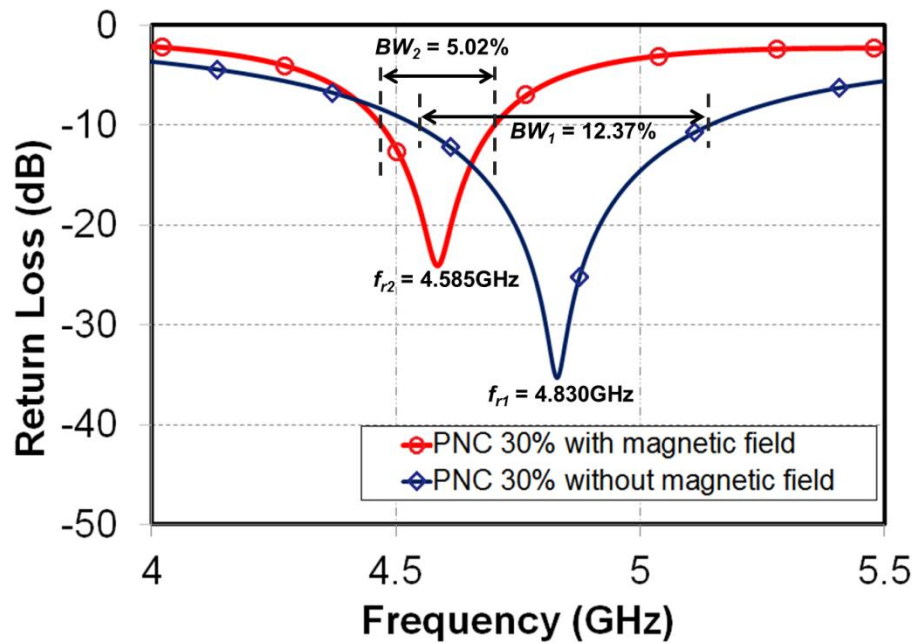

Figure 5.37 – Measured return loss of PDMS-Fe_3O_4 PNC multilayer patch antenna at 30% w.t. concentration with and without applied DC biasing magnetic field.

Figure 5.38 presents the radiation pattern of the 30% PDMS-Fe_3O_4 PNC antenna with and without biasing magnetic field. As expected, there is a significant improvement in the antenna gain induced by external field, while the antenna retains the same shape of the radiation pattern. As explained before,

this increase in the antenna gain can be ascribed to the reduction of the total loss tangent for the 30% PNC when the biasing magnetic field was applied.
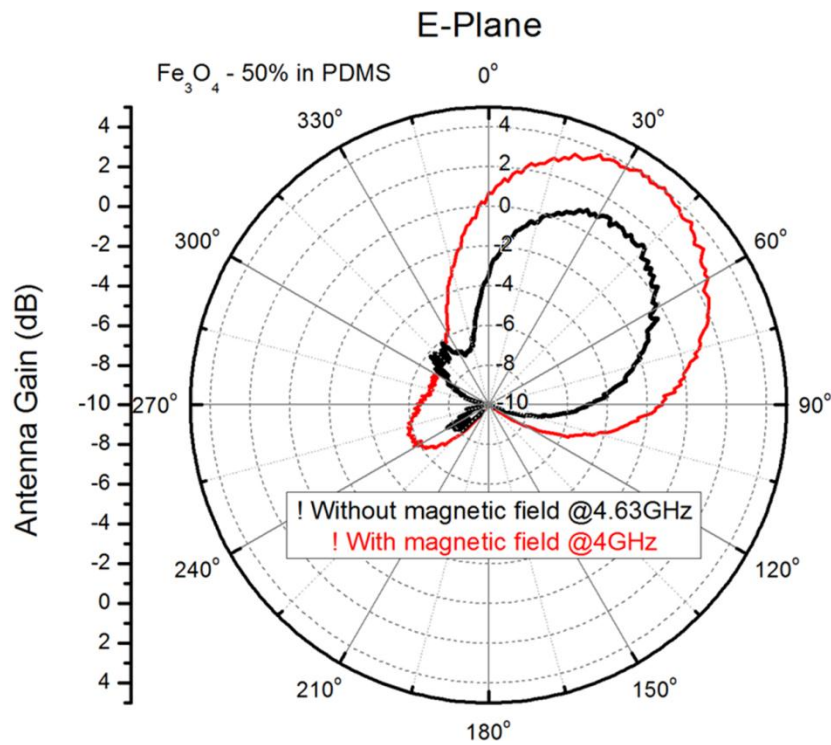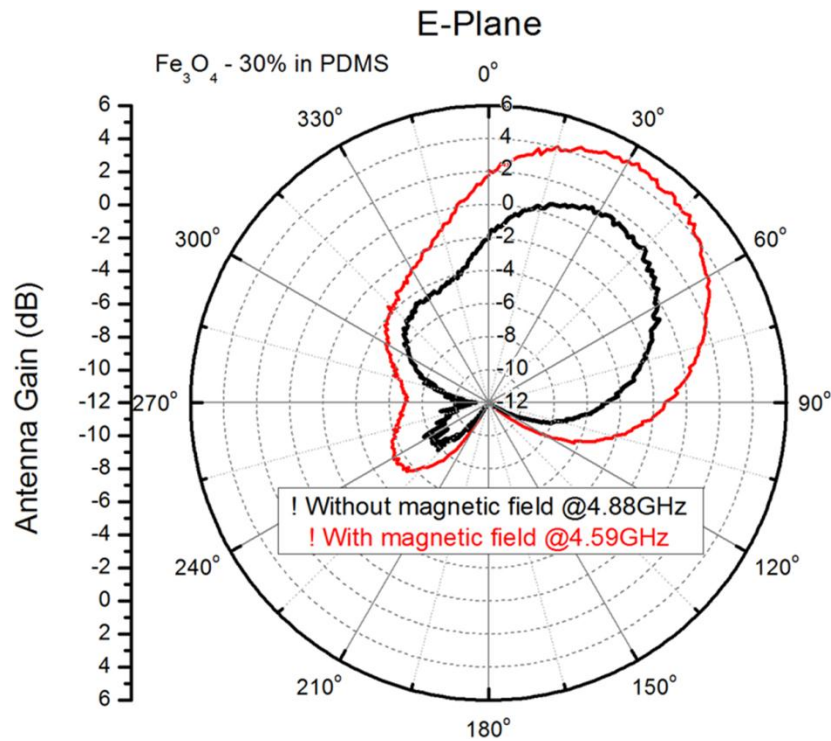

Figure 5.38 – Measured E-Plane radiation pattern of PDMS-Fe$_3$O$_4$ PNC multilayer patch antenna at 30% w.t. concentration with and without applied magnetic field.

Figure 5.39 presents a better contrast of the antenna gain with and without applied magnetic field versus frequency. In this plot, it can be seen that the gain has increased from 2.003dBi at 4.83GHz without biasing field to 5.085dB at 4.585GHz in the presence of biasing field, which represents an effective gain increase of 3.082dB or equivalent to 2 times the gain.
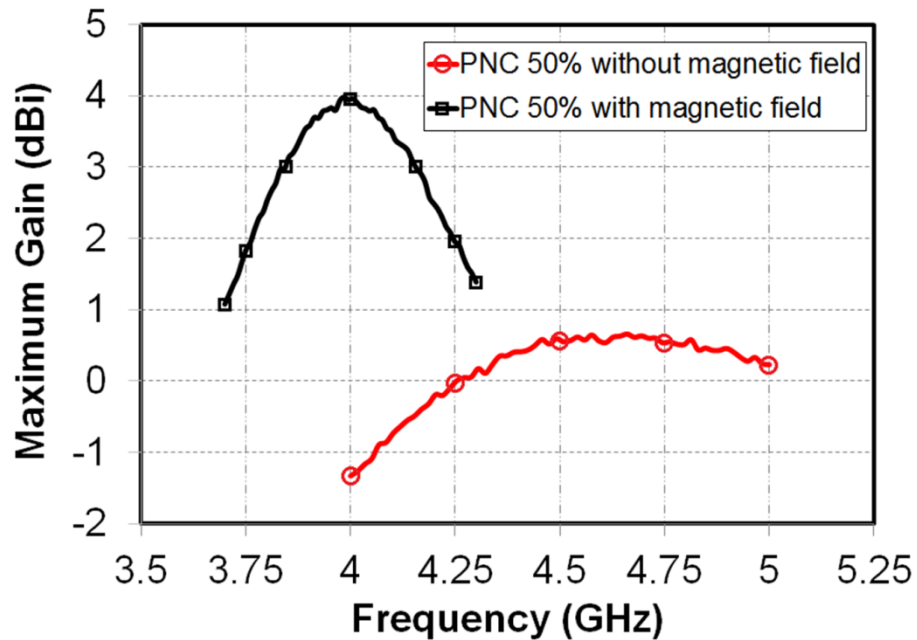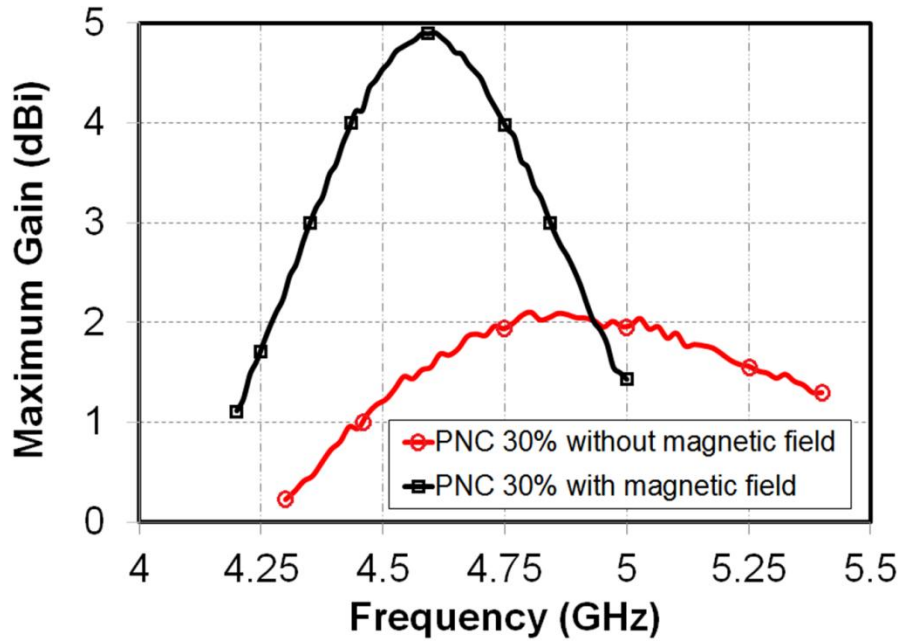
Figure 5.39 – Measured gain of PDMS-Fe$_3$O$_4$ PNC multilayer patch antenna at 30% w.t. concentration with and without applied magnetic field.

The effective miniaturization percentage and miniaturization factor for all three magneto-dielectric PNC antennas, achieved by the application of the external biasing magnetic field, are calculated using Equations (5.3) to (5.8). The results are summarized in the Table 5.8, which also compares the antenna performance parameters for all four multilayer patch antenna designs.

All the PNC antennas have achieved excellent miniaturization factors as compared to the size of the plain PDMS antenna. 30% PNC antenna only exhibited a slightly increased bandwidth, whereas the 50% PNC and 80% PNC antennas have both been demonstrated a notable bandwidth enhancement effect. Among all three PNC designs, the 50% PNC antenna has achieved the best efficiency which is almost comparable to the efficiency of the pure PDMS counterpart. Nevertheless, the antenna efficiencies have been improved

substantially for all the PNC antenna designs through the application of external

DC-biasing magnetic field generated by a stacked magnet array.

Table 5.8 – Antenna parameters of all the multilayer patch antennas with PNC-filled substrates and applied external DC biasing magnetic field. The plain PDMS antenna design is included as the reference device for comparison purposes.

Antenna Design	Resonance Frequency (GHz)	Bandwidth (MHz)	Maximum Gain (dBi)	Efficiency	Area (mm^2)	Miniaturization % / Factor
PDMS	3.931	185 (4.7%)	5.681	50.74%	594.05 (27.25x21.8)	---
PDMS-Fe_3O_4 80% PNC	3.298	245 (7.45%)	2.12	31.28%	312.05 (19.75x15.8)	57% / 2.3
PDMS-Fe_3O_4 50% PNC	3.986	244 (6.12%)	4.063	44.10%	312.05 (19.75x15.8)	47.5% / 1.9
PDMS-Fe_3O_4 30% PNC	4.585	230 (5.02%)	5.085	40.49%	312.05 (19.75x15.8)	39.5% / 1.65

A gain of 5.085 dBi is obtained for the 30% PNC antenna design, which is similar to the 5.681dBi obtained for the plain PDMS antenna. This result demonstrates that miniaturized antennas with enhanced bandwidth can be implemented by the employments of low-loss polymer nanocomposites with monodispersed superparamagnetic nanoparticles, without a considerable degradation in the overall antenna radiation performance. As a matter of fact, and from simulations results obtained in Chapter 3, there is a direct correlation between the physical area of the antenna and its highest achievable performance (gain, efficiency, etc.). The antenna with plain PDMS substrate presents larger dimensions than the PNC-based antenna designs, thus a direct comparison between the measured gains obtained from the different elaborated antennas could be ambivalent. Nevertheless, a direct comparison is made in this case to

describe that a certain acceptable gain can be realized for antennas that employ

magneto-dielectric PNC materials as substrate fillers.

Table 5.9 – Field susceptibility of the antenna performance parameters, for all the multilayer patch antennas with PNC-filled substrates, to external DC biasing magnetic field.

Antenna Design	Resonance Frequency Shifting (GHz)	Bandwidth Reduction (MHz)	Gain Increase(dBi)	Efficiency Increasing factor	Miniaturization % / Factor
PDMS-Fe_3O_4 80% PNC	-0.683	827.5	3.448	2.5x	17.16% / 1.2
PDMS-Fe_3O_4 50% PNC	-0.566	486	3.457	2.15x	12.43% / 1.14
PDMS-Fe_3O_4 30% PNC	-0.247	367.5	3.082	1.69x	5.11% / 1.05

Finally, Table 5.9 shows the susceptibility of the antenna performance

parameters for all four designs to externally applied DC biasing field. As shown in

Table 5.9, all the values for the variation of the performance metrics in response

to the external magnetic field were derived by taking into account the measured

results with and without external DC biasing magnetic field.

Chapter 6

Conclusions and Future Work

6.1 Summary and Contributions to the RF/Microwave Field

This research has presented the usage of magnetite-based magneto-dielectric polymer nanocomposites for the implementation of miniaturized multilayer patch antennas. Four different patch antenna designs were systematically explored. Each one of the PDMS-based design has a different loading concentration of superparamagnetic nanoparticles (from 0% to 80%). The performance of the constructed antennas was measured with and without externally applied DC biasing magnetic field. Comparisons between the different designs were thoroughly conducted to demonstrate the correlation between the nanoparticle loading concentration presented in the polymer nanocomposites and the corresponding resultant dielectric and magnetic properties.

Antenna miniaturization up to 57% and antenna bandwidth increase of 58% (from 4.7% to 7.45%) have been successfully demonstrated, while retaining an acceptable antenna gain by the employment of PDMS-Fe_3O_4 PNC with 80% w.t. concentration. Furthermore, the reduction of the loading concentration of the superparamagnetic nanoparticles in the PNC (e.g. 50% w.t. PNC and 30%w.t. PNC) decreased the dielectric and magnetic loss properties, then resulting in the enhancement of the antenna gain, up to the value close to that achieved by its pure PDMS counterpart. Beyond acknowledging that the reduction of

nanoparticle loading does decrease the permeability of the resultant PNC, thereby reducing both bandwidth miniaturization factor of the multilayer antenna, it is paramount to notice that resulting magneto-dielectric characteristics of the PDMS-Fe_3O_4 nanocomposite materials with low nanoparticle concentrations, do offer superior electrical properties when compared to pure PDMS substrates. For instance, the antenna with embedded PDMS-Fe_3O_4 PNC at 30% w.t. has exhibited a gain of 5.085dBi, similar to the measured gain of 5.095dBi of the pure PDMS antenna. Additionally, the antenna with the PNC at 30% w.t. presented slightly increased bandwidth of 5.02% (as compared to the 4.7% for pure PDMS counterpart), together with a significant miniaturization of 39.5%, which enables 1.65 times smaller antenna dimensions.

In conclusion, the novelty of this dissertation work is the fact that it represents the first known successful attempt when PDMS-Fe_3O_4 magneto-dielectric polymer nanocomposites have been effectively employed for the miniaturization and bandwidth enhancement of microstrip patch antennas. Finally, the demonstration of tunability of the antenna characteristics (i.e., resonance frequency and radiation properties), under externally applied DC magnetic fields generated by permanent magnets, opens alternate approaches for further research and implementation of reconfigurable antennas as well as tunable antenna arrays.

6.2 Recommendation for Future Work and Emerging Projects

The methodologies and experiments developed in this dissertation work can be used as the baseline for the implementation of multilayer planar antennas

that employ low-loss superparamagnetic polymer nanocomposites systems as substrates. Certainly, there is room for further improvement beyond the results reported herein. Initially, efforts should focus on how to mitigate dielectric and magnetic losses of magneto-dielectric nanocomposites, especially while they present high particle loading concentrations. New magneto-dielectric polymer nanocomposites can be developed by selecting different polymer matrices and nanoparticles. The selection of a polymer with very low dielectric losses will help improve antenna performance. Factors such as the compatibility with the nanoparticle system and the solvents used for the nanoparticle suspension should be considered. In future work, the use of inorganic coating for the purpose of surface functionalization should be explored. Aside from reducing the loss associated with organic surfactant, the usage of inorganic coating can further improve the compatibility with existing polymers that require high curing temperatures (e.g., PTFE based polymers).

Furthermore, magneto-dielectric polymer nanocomposites may be used in other antenna topologies in order to achieve increased miniaturization and maximize the antenna performance (i.e., antenna gain, bandwidth), while taking full advantage of the properties of these new polymeric materials.

Similarly, other topologies can potentially take advantage of magneto-dielectric materials with controllable values of μ_r and ε_r. With the magneto-dielectric PNCs developed in this dissertation work, antennas based on artificial magneto-dielectric material, such as the design proposed by Namin *et al*. at [1], may now become realizable.

Finally, the magneto-dielectric PNC materials developed in this work can be investigated simultaneously with Electromagnetic Band Gap Structures and Frequency Selective Surfaces. The proper implementation of magneto-dielectric PNC in such structures may help improve their operational frequency range and provide additional miniaturization.

References

[1] F. Namin, T. G. Spence, D. H. Werner and E. Semouchkina, "Broadband, Miniaturized Stacked-Patch Antennas for L-Band Operation Based on Magneto-Dielectric Substrates," *IEEE Transactions on Antennas and Propagation*, vol. 58, no. 9, pp. 2817-2822, September 2010.

[2] J. L. Volakis, C. C. Chen and K. Fujimoto, "Small Antennas [Electronic Resource]: Miniaturization Techniques & Applications," McGraw-Hill, New York, 2010

[3] F. Erkmen, Chi-Chih Chen and J. L. Volakis, "Impedance Matched Ferrite Layers as Ground Plane Treatments to Improve Antenna Wide-Band Performance," *IEEE Transactions on Antennas and Propagation*, vol. 57, no. 1, pp. 263-266, 2009.

[4] K. N. Rozanov, I. T. Iakubov, A. N. Lagarkov, S. A. Maklakov, A. V. Osipov, D. A. Petrov, L. Ryzhikov, M. V. Sedova and S. N. Starostenko, "Laminates of thin ferromagnetic films for microwave applications," *The Sixth International Kharkov Symposium on Physics and Engineering of Microwaves, Millimeter and Submillimeter Waves and Workshop on Terahertz Technologies, 2007. MSMW '07.*, 2007, pp. 168-173.

[5] C.A Balanis, "Advanced Engineering Electromagnetics," John Wiley and Sons, Inc. 1989, pp. 181-243.

[6] R.C. Hansen and M. Burke, "Antennas with magneto-dielectrics*," Microwave Optical Technology Letters*, vol. 26, no. 2, pp.75-78, July 2000.

[7] H. A. Wheeler, "Transmission-Line Properties of Parallel Strips Separated by a Dielectric Sheet," *IEEE Transactions on Microwave Theory and Techniques*, vol. 13, no. 2, pp. 172-185, 1965.

[8]   S. Sun and H. Zeng, "Size-Controlled Synthesis of Magnetite Nanoparticles," *Journal of the American Chemical Society*., vol. 124, no. 28, pp. 8204-8205, July 2002.

[9]   R.M. Cornell, U. Schwertmann, "The Iron Oxides: Structure, Properties, Reactions, Occurrence and Uses," VCH, New York, 1996, pp28-29.

[10] L. Fu, V. P. Dravid and D. L. Johnson, "Self-assembled (SA) bilayer molecular coating on magnetic nanoparticles," *Applied Surface Science*, vol. 181, no.1-2, pp. 173-178, 9/3, 2001.

[11] N. A. Frey, S. Peng, K. Cheng and S. Sun, "Magnetic nanoparticles: synthesis, functionalization, and applications in bioimaging and magnetic energy storage," *Chemical Society Reviews*, vol. 38, no. 9, pp. 2532-2542, 2009.

[12] Z. Xu, C. Shen, Y. Hou, H. Gao and S. Sun, "Oleylamine as Both Reducing Agent and Stabilizer in a Facile Synthesis of Magnetite Nanoparticles," *Chemistry of Materials,* vol. 21, no. 9, pp. 1778-1780, 2009.

[13] J. L. Wilson, P. Poddar, N. A. Frey, H. Srikanth, K. Mohomed, J. P. Harmon, S. Kotha and J. Wachsmuth, "Synthesis and magnetic properties of polymer nanocomposites with embedded iron nanoparticles," *Journal of Applied Physics*, vol. 95, pp. 1439-1443, 2004.

[14] C. Morales, J. Dewdney, S. Pal, S. Skidmore, K. Stojak, H. Srikanth, T. Weller and Jing Wang, "Tunable Magneto-Dielectric Polymer Nanocomposites for Microwave Applications," *IEEE Transactions on Microwave Theory and Techniques*, vol. MTT-59, pp. 302-310, 2011.

[15] S. Pal, S. Chandra, M.H. Phan, P. Mukherjee and H. Srikanth, "Carbon nanostraws: nanotubes filled with superparamagnetic nanoparticles," *Nanotechnology*, vol. 20, no. 48, pp. 485604 (7), 2009.

[16] K Stojak, S Pal, H Srikanth, C Morales, J Dewdney, T Weller and J Wang "Polymer nanocomposites exhibiting magnetically tunable microwave properties," *Nanotechnology*, vol. 22, no. 13, pp. 135602 (6), 2011.

[17] S. Sun, H. Zeng, D. B. Robinson, S. Raoux, P. M. Rice, S. X. Wang and G. Li, "Monodisperse MFe2O4 (M = Fe, Co, Mn) Nanoparticles," *Journal of the American Chemical Society*, vol. 126, no. 1, pp. 273-279, 2004.

[18] J. Gass, P. Poddar, J. Almand, S. Srinath and H. Srikanth, "Superparamagnetic Polymer Nanocomposites with Uniform Fe_3O_4 Nanoparticle Dispersions," *Advanced Functional Materials*, vol. 16, no. 1, pp. 71-75, 2006.

[19] J.D. Hanawalt, H.W. Rinn and L.K Frevel, "Chemical Analysis by X-Ray Diffraction," Analytical Chemistry, vol. 10, no.9, pp. 457-512, 1938.

[20] Dow Corning, Sylgard® 184 Elastomer Kit Product Information, http://www.dowcorning.com/applications/search/products/Details.aspx?prod=01064291&type=PROD

[21] B. Bakar and L.F. Lemmens, "Blocking temperature in magnetic nanoclusters," *Physical Review E*, vol. 71, pp. 046109 (1-7), 2005

[22] W. B. Weir, "Automatic measurement of complex dielectric constant and permeability at microwave frequencies," *Proceedings of the IEEE*, vol. 62, no.1, pp. 33–36, Jan. 1974.

[23] A. M. Nicolson and G. F. Ross, "Measurement of the intrinsic properties of materials by time-domain techniques," *IEEE Transactions on Instrumentation and Measurement,* vol. IM-19, no. 11, pp. 377–382, Nov. 1970.

[24] E. Hammerstad and O. Jensen, "Accurate models for microstrip computer-aided design," in *IEEE MTT-S International Microwave Symposium Digest*, May 1980, pp. 407–409.

[25] M. Kirschning and R. H. Jansen, "Accurate model for effective dielectric constant of microstrip with validity up to millimetre-wave frequencies," *Electronics Letters.*, vol. 18, no. 6, pp. 272–273, Mar. 1982.

[26] J. Barker-Jarvis, E. Vanzura, and W. Kissick, "Improved technique for determining complex permittivity with the transmission/reflection method," *IEEE Transactions on Microwave Theory and Techniques*, vol. 38, no. 8, pp. 1096–1103, Aug. 1990.

[27] E. Yamashita, "Variational method for the analysis of microstrip-like transmission lines," *IEEE Transactions on Microwave Theory and Techniques*, vol. MTT-16, no. 8, pp. 529–535, Aug. 1968.

[28] A. Farrar and A. T. Adams, "Multilayer microstrip transmission lines," *IEEE Transactions on Microwave Theory and Techniques*, vol. MTT-22, no. 10, pp. 889–891, Oct. 1974.

[29] R. A. Pucel and D. J. Masse, "Microstrip propagation on magnetic substrates—Part I: Design theory," *IEEE Transactions on Microwave Theory and Techniques*, vol. MTT-20, no. 5, pp. 304–308, May 1972.

[30] H. A. Wheeler, "Transmission line properties of parallel wide strips by a conformal mapping approximation," *IEEE Transactions on Microwave Theory and Techniques*, vol. MTT-12, no. 3, pp. 280–289, May 1964.

[31] J. Svacina, "Analysis of multilayer microstrip lines by a conformal mapping method," *IEEE Transactions on Microwave Theory and Techniques*, vol. MTT-40, no. 4, pp. 769–772, Apr. 1992.

[32] J. Svacina, "A simple quasi-static determination of basic parameters of multilayer microstrip and coplanar waveguide," *IEEE Microwave and Guided Wave Letters*, vol. 2, no. 10, pp. 385–387, Oct. 1992.

[33] T. Kaneki, "Analysis of linear microstrip using an arbitrary ferromagnetic substance as the substrate," *Electronics Letters*, vol. 5, no. 19, pp. 463–465, Sep. 1969.

[34] W. Eisenstadt and Y. Eo, "S-parameter-based IC interconnect transmission line characterization," *IEEE Transactions on Components, Hybrids, and Manufacturing Technology*, vol. 15, no. 4, pp. 483–490, Aug. 1992.

[35] C. Morales, J. Dewdney, S. Pal, K. Stojak, H. Srikanth, J. Wang, and T. Weller, "Magnetically tunable nanocomposites for microwave applications," *IEEE MTT-S International Microwave Symposium Digest*, May 2010, pp. 1340–1343.

[36] J. L. Volakis, "Antenna Engineering Handbook," 4th ed., McGraw-Hill, New York, 2007.

[37] Rogers Corporation, "ULTRALAM® 3000 Liquid Crystalline Polymer Circuit Material," datasheet RF1.3000, publication #92-125. http://www.rogerscorp.com/documents/730/acm/ULTRALAM-3000-LCP laminate-data-sheet-ULTRALAM-3850.aspx.

About the Author

Cesar Morales received his B.S. degree (Honors) from Universidad del Norte (University of North), Barranquilla, Colombia, in 2004; his M.S. degree in electrical engineering from the University of South Florida, Tampa, in 2008, and is currently working towards his Ph.D. degree in electrical engineering at the University of South Florida. He is currently with the RF-MEMS Transducers Group (a division of the WAMI Center), Electrical Engineering Department, University of South Florida. His areas of research are general RF and Microwaves, RF and microwave measurements and antenna design. He also worked as an Engineering Intern at Modelithics Inc., in Tampa FL from 2007 to 2008. Mr. Morales is a Student Member of the Institute of Electrical and Electronics Engineers (IEEE) and the IEEE Microwave Theory and Techniques (MTT) Society, where he has served as reviewer for at least four Journal Publications. He is also a member if the International Microelectronics and Packaging Society (IMAPS) since 2008. His current research involves the characterization and implementation of polymer nanocomposites for microwave applications.